Title
Electronic Nano-device Fabrications and Measurements

Author
Ren, Haowen

Publication Date
2020

UNIVERSITY OF CALIFORNIA SAN DIEGO

Electronic Nano-device Fabrications and Measurements

A dissertation submitted in partial satisfaction of the
requirements for the degree Doctor of Philosophy

in

Materials Science and Engineering

by

Haowen Ren

Committee in charge:

Professor Eric E. Fullerton, Chair
Professor Renkun Chen
Professor Ping Liu
Professor Shirley Y. Meng
Professor Oleg Shpyrko

2020

The Dissertation of Haowen Ren is approved, and it is acceptable in quality and form for publication on microfilm and electronically:

Chair

University of California San Diego

2020

DEDICATION

I dedicated to my loving parents Ren, Guobin and Xiao, Ling for their very much supports. I also dedicated to my girl Liu, Xuanying who is always on my back all the time when I was struggling with my research and life.

EPIGRAPH

Don’t try,
just do it.

—Eric E. Fullerton

TABLE OF CONTENTS

LIST OF FIGURES

LIST OF TABLES

ACKNOWLEDGEMENTS

First of all, I really appreciate the full supports from my PI professor Fullerton. He is a easy-going and open-minded instructor both in study and in life. He is energetic and visionary in the research and was always willing to teach me with his immense knowledge no matter how busy he was. It was yet possible for me to walk through this Ph.D. journey without his understanding and communications at right time. I also really appreciate the help and financial supports from doctor Minh, who is always a supportive and communicative mentor just like my 'grandpa'.

Secondly, I would like to say countless thank you to my labmates, Sohini, Sheena, Jimmy, and Raj, who bring me into this lovely group; Yuxuan, Mohammed and Jeff, who I was always talking to, with numerous new ideas fresh to me; Yoon-Ho, Tuyen, Erik, and Qi, who we were spending hours together discussing SOFC project and all kinds of interesting topic in their own country.

Most importantly, I dedicated to my loving parents Ren, Guobin and Xiao, Ling for their very much supports. 2020 a special year for all the people, same for my parents who were stuck here and luckily I was well cared by them in this last year of graduate school. I also dedicated to my girl Liu, Xuanying who is always on my back all the time even when I was struggling with my research and study.

Last but not the least, I want to say thank you to all my friends who I met in my life. We shared happiness and sadness, we experienced together, and we will always be part of the precious memory in our own story.

Chapter 1, in part, is a reprint of the material "Lee, Y. H.*; Ren, H.* Wu, E.* A.; Fullerton, E. E.; Meng, Y. S.; Minh, N. Q. *All-Sputtered, Superior Power Density Thin-Film Solid Oxide Fuel Cells with a Novel Nanofibrous Ceramic Cathode*, Nano Lett., 20, 5, 2943–2949 (2020).", "H. Ren, Y. H. Lee, E. Wu, H. Chung, Y. S. Meng, E. E. Fullerton, N. Q. Minh, *Nano-Ceramic Cathodes via Co-sputtering of Gd-Ce Alloy and Lanthanum Strontium Cobaltite for Low-Temperature Thin-Film Solid Oxide Fuel Cells*, ACS Applied Energy Materials, 3, 9,

8135–8142 (2020).", and N. Q. Minh, Y. H. Lee, T. Q. Tran, H. Ren, E. E. Fullerton, E. A. Wu, Y. S. Meng, *"Development of a versatile, high-performance solid oxide fuel cell stack technology"*, ECS Trans., 91(1) 133-138 (2019). The dissertation author was the primary investigator and author of these materials.

Chapter 2, in part, is currently being prepared for submission for publication of the material "*Temperature-dependent magnetoresistance in Si-doped single-crystalline Ni nanowires*", Haowen Ren, Sohini Manna, Eric E. Fullerton. The dissertation author was one of the primary investigators and author of this material.

Chapter 4, in part, is currently being prepared for submission for publication of the material "*Ion beam etching dependence of spin-orbit torque memory devices with low switching current density enhanced by Hf interlayers*", Haowen Ren, Shih-Yu Wu, Jonathan Z. Sun, Eric E. Fullerton. The dissertation author was one of the primary investigators and author of this material.

VITA

2010-2014	B. E. in Material Science and Engineering, Central South University, Changsha
2014-2015	M. S. in Materials Science and Engineering, University of California, San Diego
2015-2020	Ph. D. in Materials Science and Engineering, University of California, San Diego

PUBLICATIONS

Y. H. Lee*, H. Ren*, E. A. Wu*, E. E. Fullerton, Y. S. Meng, N. Q. Minh, *”All-Sputtered, Superior Power Density Thin-Film Solid Oxide Fuel Cells with a Novel Nanofibrous Ceramic Cathode.”*, Nano Lett., 20, 5, 2943–2949 (2020).

H. Ren, Y. H. Lee, E. A. Wu, H. Chung, Y. S. Meng, E. E. Fullerton, N. Q. Minh, *”Nano-Ceramic Cathodes via Co-sputtering of Gd-Ce Alloy and Lanthanum Strontium Cobaltite for Low-Temperature Thin-Film Solid Oxide Fuel Cells”*, ACS Applied Energy Materials, 3, 9, 8135–8142 (2020)

H. Ren, Sohini Manna, Eric E. Fullerton”*Temperature-dependent magnetoresistance in Si-doped single-crystalline Ni nanowires*”, in preparation.

H. Ren, Shih-Yu Wu, Jonathan Z. Sun, E. E. Fullerton, ”*Ion beam etching dependence of spin-orbit torque memory devices with low switching current density enhanced by Hf interlayers*”, in preparation.

N. Q. Minh, Y. H. Lee, T. Q. Tran, H. Ren, E. E. Fullerton, E. A. Wu, Y. S. Meng, *“Development of a versatile, high-performance solid oxide fuel cell stack technology”*, ECS Trans., 91(1) 133-138 (2019).

F. Formisano, R. Medapalli, Y. Xiao, H. Ren, E. E. Fullerton, A. V. Kimel, *“Femtosecond magneto-optics of EuO*, Journal of Magnetism and Magnetic Materials, 502, 166479 (2020).

J. Wang, A. S. Jeevarathinam, A. Jhunjhunwala, H. Ren, J. Lemaster, Y. Luo, D. P. Fenning, E. E. Fullerton, J. V Jokerst, *”A Wearable Colorimetric Dosimeter to Monitor Sunlight Exposure,”*, Advanced Materials Technologies, 3 (6), 1800037, 2018

ABSTRACT OF THE DISSERTATION

Electronic Nano-device Fabrications and Measurements

by

Haowen Ren

Doctor of Philosophy in Materials Science and Engineering

University of California San Diego, 2020

Professor Eric E. Fullerton, Chair

The first part of this dissertation mainly focus on thin film solid oxide fuel cells. In recent years, solid oxide fuel cells are becoming more popular as a green energy source of electricity due to their high efficiency and low carbon emission. However, high operation temperature and materials costs are the main issues impeding the application of this technique. In this presentation, by applying magnetron sputtering technique to fabricate thin film solid oxide fuel cell, we are able to operate the cells under much lower temperature with superior performance under hydrogen or hydrocarbon fuels. Different composite nano-porous cathodes and anodes are fabricated and characterized, all showing reliable, reproducible and scalable results. The second part of the dissertation focus on fabrication and characterizations of spintronic devices, including Si-doped

single crystalline Ni nanowires, spin-triplet spintronic and SOT-MRAM devices. Spintronics has been widely applied in data storage applications such as hard disk drives, STT-MRAMs, and SOT-MRAMs, etc. Recently, development of spintronics theories and experiments has allowed it to expand to broader applications, such as domain wall MRAMs, neuromorphic computing and quantum computing. In this section, we will introduce the growth of Si-doped single crystalline Ni nanowires, the effects from AMR, OMR and domain wall MR at low magnetic fields and electron-magnon interaction at high magnetic fields. We studied superconducting triplet spin valve devices. In general, singlet Cooper pairs generated from superconducting layers cannot survive in magnetic layer. However, if we introduce an inhomogeneous moments between these two layers, triplets Cooper pair appeared and can survive much longer than singlet Cooper pair in ferromagnetic materials. In our study, we fabricated epitaxial Ni and Co superconducting spin-triplet spin valves to study this effect. By rotating the soft NiFe layer to break the linearity of magnetizations, inhomogeneous moments can be generated. Magnetization configurations are characterized by polarized neutron reflectometer. By measuring the change of superconducting critical temperature at different angles of external field, we observed that the behavior of spin valve is highly sensitive to the thickness of the inhomogeneous magnetic layers. Lastly, the SOT-MRAM project during the internship in IBM is presented. SOT-MRAM is a potential second generation MRAM compared to STT-MRAM due to its higher efficiency, stability and lower switching current. We fabricated single SOT-MRAM device using β-W as spin current source. Ion beam etching process, the most critical fabrication process, has been studied. Shapes and aspect ratio effects on nanopillars are discussed. We also introduced thin Hf interlayers in the heterostructure to further decrease the critical switching current. Simulations proves an enhancement in perpendicular anisotropy will lead to this reduction in critical switching current.

Chapter 1

Thin Film Solid Oxide Fuel Cells

1.1 Introduction and Motivation

Solid oxide fuel cells (SOFCs) have been developed for a broad spectrum of power generation applications.[1] Power systems considered for SOFCs range from watt-sized devices to multimegawatt power plants.[2] Recently, the introduction of nanotechnology has facilitated the development of thin-film SOFCs (TF-SOFCs) and has shown dramatically improved cell performance also allowing for operation for the cell at lower temperatures (e.g., 400-650 °C versus the conventional 650-800 °C).[3] Various deposition processes have been used to fabricate cell components for TF-SOFCs, for example, chemical vapor deposition processes such as atomic layer deposition (ALD) have been shown to be capable of depositing high-quality films.[4, 5, 6, 7] However, it is difficult to fabricate porous films required for the anode and cathode using ALD; the structure must be porous for efficient gas supply. To this end, pulsed laser deposition (PLD) has also been used, and ceramic-based TF-SOFCs fabricated via PLD showed high performance and stability.[8, 9] However, since it is difficult to use PLD for large area deposition with high throughput in addition to high maintenance costs, it is preferable to develop a scalable and cost-effective deposition technique such as sputtering for fabricating TF-SOFCs.

Among various physical vapor deposition processes, sputtering is a versatile technique commonly used in mass production as it can create either porous or dense films by changing the deposition conditions. Several studies have used sputtering to fabricate TF-SOFCs and showed high performance at relatively low operating temperatures.[10] However, most of these sputtered TF-SOFCs utilized platinum (Pt) as an electrode. Although Pt exhibits high catalytic activity at low temperatures and a porous Pt structure can be made by sputtering,[11] Pt can easily agglomerate at elevated temperatures and thus is not suitable for use at typical SOFC operating temperatures of 650-800 °C.[12] Several approaches have been considered to mitigate this such as cosputtering with ceramics or applying a coating on the Pt surface,[13, 14, 15] but the preferable solution is to construct the electrode with a material that is more thermally stable. For this purpose, ceramic-based materials have desirable thermal properties.[16, 17, 18] However, it is difficult to make ceramic materials into porous films via sputtering. The most common approach is to sputter using a high pressure of the sputtering process gas to increase the number of collisions and decrease the kinetic energy of the deposited atoms. This results in low surface mobility of the deposited atoms and the increasing effects of self-shadowing. As the deposition evolves, grains are formed with well-defined and often porous grain boundaries known as zone 1 growth in thin film deposition.[19] In addition, atoms in the gas can form particle clusters prior to deposition aiding in the formation of porous films. If a porous ceramic electrode can be deposited through sputtering then the entire cell can be fabricated using a single process and a single piece of equipment, which is more cost-effective and beneficial for future mass production of devices.

1.2 Operation of Solid Oxide Fuel Cells

Unlike energy storage devices like batteries, fuel cell is an electrochemical device that directly converts chemical energy from fuels to electrical energy. It can continuously generate electricity from a continuous supply of fuels, like hydrogen and simple hydrocarbon gas, and oxidant, mostly oxygen from atmosphere. The energy stored in battery is limited by the amount of reactant stored in the battery, it stopped working once reactants completely consumed. However, fuel cells can operate for infinity time if there is a constant supply of reactant and oxidant.

Contrary to conventional combustion engine, the efficiency of fuel cells are not limited by the Carnot cycle, leading to a much lower waste of energy during the operation. It was not until late 20th century that fuel cell start to become much more promising due to zero-carbon emission when operating with hydrogen fuel and also cost competitive to batteries due to development of new fabrication techniques. Fuel cell has becoming a viable and potential alternative to fossil fuels as a sustainable energy source.

There are different types of fuel cells, mostly depends on the type of electrolyte being chosen. For example, polymer electrolyte membrane fuel cells (PEMFC) use polymer membrane as electrolyte, alkaline fuel cell (AFC) use KOH as electrolyte, phosphoric acid fuel cells (PAFC) use phosphoric acid as electolyte, and solid oxide fuel cells (SOFCs) use ionic conducting solid oxides as electrolyte. In this chapter, we will focus on the SOFCs. SOFCs utilize ionic conducting ceramics as electrolyte, which requires a relatively higher operation temperature than other types of fuel cells. In conventional SOFCs, yttrium-stabilized-zirconium (YSZ) is the most commonly seen oxide that has high oxygen ions conductivity and high stability at high temperature (800-1000 °C). The advantages of SOFCs are promising, including much higher efficiency (70 %) than other types of fuel cells (40 %), wide range of applicable gaseous fuels (hydrogen, methane, ethanol, etc.), reforming the fuels at high temperature without catalyst, cheap ceramics to reduce materials costs and no water management system required, etc.

The mechanisms of SOFCs is straightforward. Similar to conventional fuel cells, SOFCs consist of an anode that react with fuels, electrolyte that allows not electrons but ions to pass through, and a cathode for oxygen reduction reaction (ORR). A brief configuration of SOFCs and their basic chemical reactions are shown in Figure 1.1(a). When feeding hydrogen fuel to SOFCs, for the oxygen ions conducting type of fuel cells, the chemical reactions happens in the fuel cells follows the forms below:

$$\text{Anode:} \quad H_2 + O^{2-} \rightleftharpoons H_2O + 2e^- \tag{1.1}$$

$$\text{Cathode:} \quad \frac{1}{2}\mathrm{O_2} + 2\,\mathrm{e^-} \rightleftharpoons \mathrm{O^{2-}} \tag{1.2}$$

$$\text{Overall:} \quad \mathrm{H_2} + \frac{1}{2}\mathrm{O_2} \rightleftharpoons \mathrm{H_2O} \tag{1.3}$$

The flow of ionic charges through the electrolyte are balanced by the electronic charge through external circuit. The by-products are produced at anode side in this case. The proton conducting types have similar chemical reaction but protons are moving in electrolyte and by-products are produced in cathode instead. Thermodynamically, due to the difference of activity of oxygen in anode and cathode, an electrical potential among them is generated. The open circuit voltage (OCV) is determined by the temperature and difference of oxygen partial pressure between anode and cathode and it follows the Nernst equation:

$$E_{OCV} = -\frac{RT}{nF} ln \frac{P_{O_2}(anode)}{P_{O_2}(cathode)} \tag{1.4}$$

where R is the gas constant, T is the temperature, n is number of transferred electrons, P is the oxygen partial pressure in the electrodes and F is the Faraday constant. The $P_{O_2}(cathode)$=0.21 atm due to the air is delivered as oxidant to cathode. According to the overall reaction from equation (1.3), we can know that the kinetic equations for this fuel cell and their relations to the Gibbs free energy are:

$$K_{eq} = \frac{P_{H_2O}}{P_{H_2} P_{O_2}^{1/2}} \tag{1.5}$$

$$\Delta G_T = \Delta H_T - T\Delta S_T = -RT ln(K_{eq}) \tag{1.6}$$

where K_{eq} is the equilibrium constant, ΔG_T is Gibbs free energy, ΔH_T and ΔS_T are enthlapy and entropy at temperature T respectively. Since the by-product water only appears in the anode side,

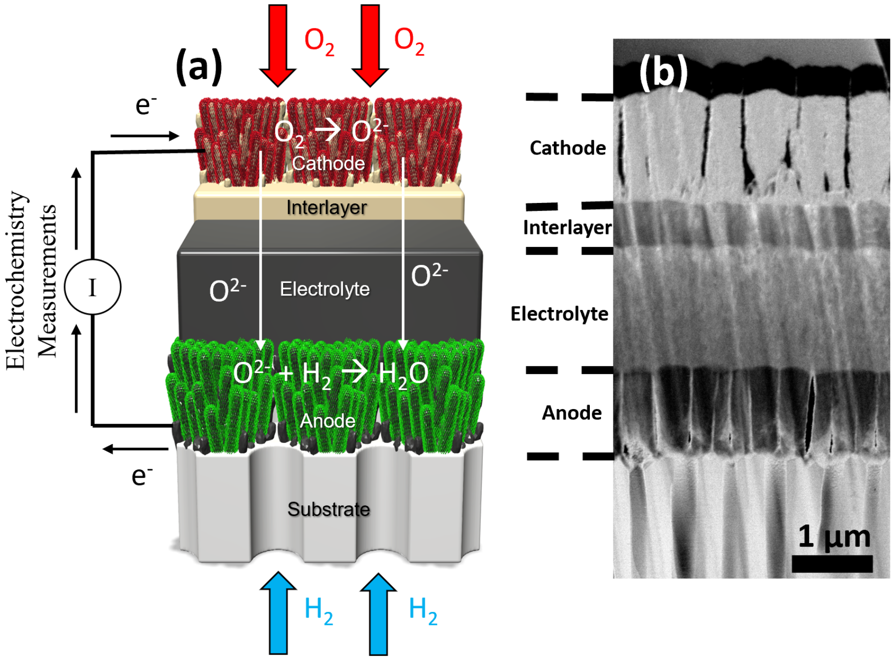

Figure 1.1. (a) Breif configuration for TF-SOFCs and (b) corresponding SEM image for a sputtered full cell

this could used to represent $P_{O_2}(anode)$ in equation (1.4). By combining equation (1.4-6), we can get:

$$P_{O_2}(anode) = \left(\frac{P_{H_2O}}{P_{H_2}}\right)^2 exp\left(\frac{2(T\Delta S_T - \Delta H_T)}{RT}\right) \tag{1.7}$$

This equation could used to estimate the theoretical Nernst potential at any given operation temperature of SOFC system. In reality, the measured OCV is always lower than this calculated value because of electrochemical losses and polarization losses. Besides, in real world, there is an overpotential casued by ohimic resistance, charge transfer polarization, and diffusion polarizations. This will always make the operation voltage lower than its theoretical values.

The conventional SOFCs requires high operation temperature, normally up to 800-1000 °C. This operation temperature increases the costs of operation and limits the applicable materials of interconnects and largely reduces the possible applications of SOFCs. One of the solution is to fabricate the TF-SOFCs. It is known that the oxygen ionic conductivity σ of oxides usually follows an Arrhenius-type temperature dependence and also strongly depends on the geometry of the thin films as followed,

$$\sigma T = Aexp\left(\frac{-E_a}{kT}\right) \tag{1.8}$$

$$\sigma = t/RS \tag{1.9}$$

where E_a is the activation energy, k is Boltzman constant, A is a pre-factor, t is the thickness of thin film oxide, S is the cross-sectional area, and σ is the measured oxygen ionic conductivity of the thin films. Clearly, we can observe there are two ways to increase the σ of the thin film oxides: One is by increasing the temperature and the other is by decreasing the thickness of oxides. In this chapter, we are presenting using magnetron sputtering technique to fabricate YSZ-based TF-SOFCs, which makes the operation temperature below 650 °C.

1.2.1 Magnetron Sputtering

Magnetron sputtering is a dominant technique for the growth of thin-film heterostructure due to the high quality, large quantity and relatively low costs of the deposition. Apart from that, magnetron sputtering has the advantage of room-temperature deposition and has the potential for large-area deposition, enabling fabrication scale-up. The mechanism for magnetron sputtering is straightforward. A closed magnetic field is applied parallel to the target surface and then the secondary electrons will circle around the magnetic field, which in return enhance the ionization efficiency of the sputtering process. This mechanism guarantees a high sputtering rate by increasing the ion density and energy. During the sputtering process, a negative bias electric field is applied between the target and substrate holder that will accelerate the electrons to move fast towards the substrate holder. Accelerated electrons then circle around the magnetic field due to the Lorentz force and collide with processing gases (for example Ar atoms), ionizing the Ar atoms into positive charged particles Ar^+. These positively charged Ar ions are driven by electric field and gain kinetic energy, which will collide with atoms on the surface of targets. After the collision, part of the kinetic energy is transferred to the atoms on the surface of target and this cascade process will let part of the target atoms have sufficient momentum to escape the the target, thus sputtered to the substrate. Electrons are also emitted in the collision process from the target where Ar ionized again. In the steady state a plasma, confined by the magnetic fields, is generated and a uniform deposition rate is achieved. During the sputtering process, the sputtered atoms will experience multiple randoms collision with gas atoms and molecules in the chamber and forms a complex scattering behavior, which could used to control the morphology of the sputtered structure.

As we discussed in the introduction, compared to other PVD fabrication methods, magnetron sputtering allows for extensive control of the morphology of the deposited thin films (whether it is a dense electrolyte or porous electrodes) by modifying the sputtering conditions. In most cases, magnetron sputtering is carried out in low processing pressure (usually below 5 mTorr) to ensure dense film structure. This approach is used to fabricate dense and thin oxide electrolyte. However, it is difficult to get porous electrodes under such low pressure. The most common approach to get porous electrodes is to sputter using a high pressure of sputtering process gas at room-temperature. The high gas pressure increases the number of collisions and decreases the kinetic energy of the deposited atoms as shown in Figure 1.2. This results in low surface mobility of the deposited atoms and the increasing effects of self-shadowing. As the deposition evolves, grains are formed with well-defined and often porous grain boundaries known as zone 1 growth in thin-film deposition.[19] In addition, atoms in the gas can form particle clusters prior to deposition aiding in the formation of porous films. If a porous ceramic electrode can be deposited through sputtering then the entire cell can be fabricated using a single process and a single piece of equipment simply changing process gas pressure, which is more cost-effective and beneficial for future mass production of devices.

1.2.2 Anode Materials

Anode is the place where oxidation of fuels happens. This electrochemical reaction usually take place at the triple phase boundary (TPB), which is the crossing line of electrode,

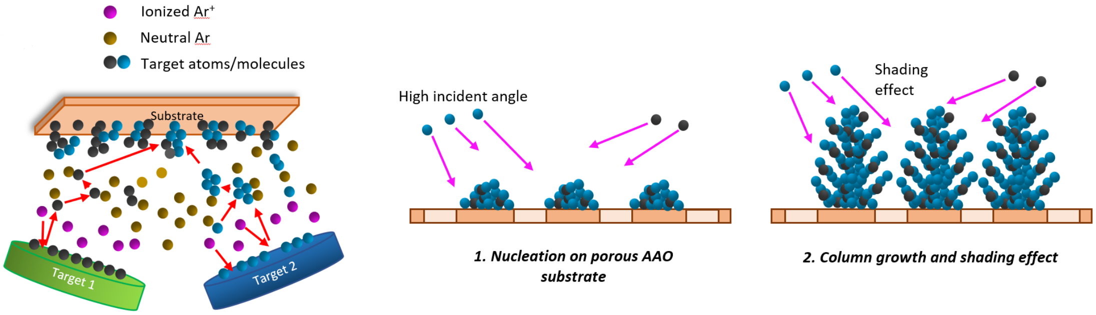

Figure 1.2. Schematic of the co-sputtering process and the deposited nano-ceramic cathode nanostructure and column growth process.

electrolyte, and gas phase. The selection of anode materials is strongly depends on the type of fuel fed into the anode. The microstructure of anode materials, morphology of anode, active area, size and distribution of porosity for efficient gas transportation are key factors to reduce the anode polarization losses and promote the catalytic activities of anode. Besides, anode also requires high chemical and thermal stability along with small thermal expansion mismatch between different layers. Metals and carbon were commonly used as anode materials, which include pure elements like Pt, Ni, Fe, Co, and C. Among these materials, Ni is the most commonly used metal anode due to its low cost and high catalytic activity towards hydrogen oxidation. However, thermal expansion mismatch between Ni and electrolyte causes severe degradation after operating at high temperature. To overcome this issue, cermets anode materials are introduced to reduce the thermal expansion mismatch and also increase the length of TPB. For pure hydrogen fuel, Ni/YSZ cermet anode is commonly used in most of the SOFCs. It satisfies most of the requirements of SOFCs. Apart from that, Ni/YSZ anode exhibits high electrical conductivity and also a reasonably high ionic conductivity. In our TF-SOFCs, we are co-sputtering Ni metal with Y-Zr alloy targets and let the deposited anode oxidizes into Ni/YSZ cermets anode in the air. Mogensen and Lindegaard [20] proposed the possible mechanism for the oxidation of hydrogen in Ni/YSZ anode based on the impedance spectroscopy results. The steps are following: the absorption of H_2 on the surface of the Ni and the formation of H^+, the diffusion of H^+ to the Ni/YSZ boundary, the reaction of H^+ with O^{2-} and releasing of the product water. Kinetically, The rate determine steps are usually from the combination of proton and oxygen ions and the absorption of hydrogen atoms on the Ni surface. Overall, the possible steps that might causes the change in eletrochemical reaction rates are summerized below[21]: (1) On the anode electrocatalyst surface: The first step is the mass transport of gaseous fuel to the electrochemically active region of porous anode material followed by adsorption of fuel species onto electrocatalyst surface. The surface diffusion of active adsorbate species to the TPB region occurs, which is followed by desorption of any electrocatalyst-adsorbed oxidation products from anode electrocatalyst surface. (2) On the electrolyte surface at the vicinity of the anode: The oxygen ions migrate from the bulk of electrolyte up to the electrolyte surface, ensued with surface diffusion of ionic species to the TPB region and desorption (if necessary) of any electrolyte-adsorbed oxidation products from electrolyte surface. (3) At the three-phase boundaries: Release of electrons formed during charge transfer reaction into the electrocatalyst bulk.

1.2.3 Anode for Hydrocarbon Fuels

Modern SOFCs systems requires flexibility in the fuel selection, which means hydrocarbons fuels, such as natural gas (methane), alcohol, gasoline, etc., should be able to replace hydrogen in some situations. Besides, hydrocarbon fuels are much easier for storage, delivery and refill based on existed infrastructure, and the high efficiency of SOFCs can limit the amount of carbon footage compared to conventional combustion engine. However, Ni/YSZ cermets anodes are suffering from severe sulfur poisoning and carbon deposition, especially the carbon deposition is much more severe in TF-SOFCs due to the nano-structure of anode. The surfur poisoning is caused by the formation of H_2S phase from S and H_2. Resulting H_2S will adsorb to the Ni surface and deactivate the catalytic activity of Ni towards oxidation of H_2. Using methane as an example, chemical reactions take place during carbon deposition are usually in the following order[22]:

$$CH_4 \rightleftharpoons C + 2H_2 \tag{1.10}$$

methane decomposes at high temperature when carbon deposition is still low concentration,

$$CO + H_2 \rightleftharpoons C + H_2O \tag{1.11}$$

part of carbon monoxide is reduce by hydrogen gas into carbon,

$$2CO \rightleftharpoons C + CO_2 \tag{1.12}$$

and disproportionation of CO start to take place at low temperature when CO reach high concentration in reformate gas. The morphology of deposited carbon clusters is strongly affected by temperature, anode materials and fuel composition. This carbon depositions only take place at the surface of Ni metals due to catalytic graphitization mechanism. The Ni metal cations intercalate into graphite' planes and forming particles on the surface of graphite.[23] To solve this issue, there are few anode materials that can be used to avoid carbon depositions as we discuss below.

Ceria (CeO_2) is known as a mixed ionic-electronic conductor (MIEC) in reducing gases. Its electronic conductivity is much higher than that of YSZ and its ionic conductivity can be engineered by doping with oxides (CaO, GdO_3, and Y_2O_3, etc.) This can expand the active sites for hydrocarbons oxidization process. There are studies showed no carbon deposition during hydrocarbon fuels mode when applying ceria as anode materials or as interlayer.[21] Among all of these doped ceria, gadolinium-doped ceria (GDC) is the most commonly used materials for the operation of hydrocarbon fuels. Researcher found that with the help of moisture, Ni/GDC cermet anode is tolerant to carbon deposition when reasonable current is passing through the fuel cell. CO can also help to suppress the carbon deposition in this type of anode. In our test, we fabricated anode using Ni/GDC cermet to make it applicable under hydrocarbon fuels.

Besides, different pure metals like Cu and Au shows resistance to carbon depositions. Both metals are functioning as a pure electronic conductor and are showing no catalytic activity toward breaking of hydrocarbon in the anode and leading to no poisoning of anodes.[24] However, both of these noble metals are suffering from low melting point that becomes crucial at nano-scale. One of the solution is to use Ru metal as anode.[25, 26] The melting point of Ru metals is 2334 °C, ensure the nanostructure of anode thermally stable at operation temperature. Besides, Ru is known as a good catalyst for reforming reaction, which promote the break of hydrocarbons into hydrogen gas and carbon dioxides. In our experimental setup, we used Ni-Ru-GDC as a composite anode to avoid carbon deposition in methane fuel.

1.2.4 Electrolyte Materials

Different than PEMFCs, SOFCs uses solid oxides as the electrolyte to conducting ions between anode and cathode. The oxide ion conduction is caused by oxygen vacancy hopping mechanism. To obtain high ionic conductivity, the electrolyte materials should contain large inter-ionic open space to have high point defect disorder and low migration enthalpy. Usually metal oxides does not possesses high ion mobility due to large charge valence bond in the lattice. To address this issue, doping metal oxides with different oxides can create oxygen vacancy defects and thus increase the ionic conductivity. In general, there are few requirements for a qualified electrolyte materials: high ionic conductivity, low electrical conductivity, thermodynamic and chemical stable at elevated temperatures, thermal expansion compatible with electrodes, and processes reliable mechanical properties. Among all kinds of electrolyte materials, one of the most commonly seen crystal structure is the Fluorite structure oxides. For example, both CeO_2 and ZrO_2 belong to this type of crystal structure. However, both of them do not process high ion conductivity due to low concentration of oxygen vacancy. To introduce oxygen vacancies into the crystal structure, acceptor cations like Gd^{3+} and Y^{3+} are doped into pure oxides and substitute Ce^{4+} and Zr^{4+}. In general case, these type of reactions can be represented by Kroger Vink notation as followed:

$$\mathrm{D_2O_3} \xrightarrow{2AO_2} 2\,\mathrm{D}_{\mathrm{A}}^{'} + 3\,\mathrm{O}_{\mathrm{O}}^{\times} + \mathrm{V}_{\mathrm{O}}^{\cdot\cdot} \tag{1.13}$$

from this equation, it is obvious that increasing dopant concentration can achieve higher oxygen vacancies concentration and thus have higher change of jump possibility between two sites in the crystal structure. This doping process will make electolyte have much higher ionic conductivity. Ionic conductivity can be described in terms of charge carrier concentration, which is proportional to the oxygen vacancy concentration. During the diffusion process of oxygen ions, oxygen ion jumps from its original tetrahedral site to the adjacent oxygen vacant site. This diffusion process can be described by enthalpy and entropy of migration. Combining all these factors, the equation (1.8) becomes:

$$\sigma_i T = A[V_{\ddot{O}}]exp(-\frac{\Delta H_m}{kT}) \tag{1.14}$$

Clearly, the temperature dependence of ionic conductivity is proportional to the vacancy concentration and the lower the ΔH_m, which means the easier migration of oxygen ions, the higher the ionic conductivity. However, the ionic conductivity cannot simply presented by this equation. In reality, ionic conductivity in electrolyte is also mainly affected by defect association, oxygen paritial pressure, dopant cations and the microstructure of electrolyte (grain boundaries and grain size). In our TF-SOFCs, we are depositing few microns thick YSZ/GDC bilayers as electrolyte.

1.2.5 Perovskite and Cermet Cathode Materials

Cathode is the place where oxygen molecules are absorbed and reduced to oxide ions. This oxygen reduction reaction (ORR) can take place on any place of cathode depends on the choice of cathode materials. For metal cathode, the ORR usually take places at the TPB and for MIEC cathode, ORR can occur in the bulk of cathode. There are few basic requirements for the choice of cathode materials, they need to process high electronic conductivity, small mismatch of thermal expansion coefficient to other components in the fuel cells, chemical compatibility with electrolyte and interconnect materials, high porosity, high oxygen ion conductivity, and high catalytic activity for ORR. The ORR in cathode can be concluded into several basic mechanisms: (1) Chemical reaction step: oxygen moledules are dissociated and adsorbed on the surface of cathode and diffusing to TPB. At TPB, oxygen molecules are reduced to O^{2-} by the free electrons provided from anode. (2) Co-limitation by kinetic and mass transfer: the overall reaction rate is dependent on both diffusion of gases and the length of active area in porous cathode. (3) Electrochemical kinetics confined to TPB: oxygen gas reduced at TPB and the catalytic activity of cathode materials near TPB.[21] Researchers found that the ORR rate is strongly dependent on the size of active area on the cathode/electrolyte interface. Considering this, increasing the reaction active area becomes the most critical condition to improve the overall performance of cathode. However, cathode made of noble metals have its own limitations as we discussed before. One of the solution to address this issue is via fabricating perovskite cathodes and mixing them with ionic conducting oxides.

Perovskite materials are famous for their wide range of applications in solar cells and semiconductor devices due to the flexibility of adjusting their unique physical properties. Perovskites are a type of oxides with formula ABO_3. In the perovskite crystal structure, the A sites are occupied by lower valance cations, such as La, Sr, Ca, etc., which is large in radius and coordinated to 12 oxide ions. The B-sites are then occupied by higher valance cations like Ni, Co, Ti, Cr, etc, which are usually coming from transition metals. At SOFC operation temperature, perovskites process a semiconducting band structure which is electronic conducting. In most of the cases, undoped perovskite materials do not process high ionic conductivity. By partially substituting A-site or B-site cations with acceptor cations like Sr^{2+} or Mn^{2+}, we can obtain oxygen deficient perovskites, such as LSM and LSC, which have high ionic conductivity.

To better understand the cathode reactions, we can approach the mechanism from two aspects: at atomic scale and at bulk scale. At atomic scale, perovskites with a reducible transition metal cation occupies on B-site and a mix of rare and alkaline earths cation in A-site will exhibit an octahedral symmetry around the transition metal cation, which gives a high electronic conductivity by promoting a metallic or semiconducting band structure at high temperature. At the same time, doped perovskites with oxygen vacancies will allows oxygen ions diffuse in the bulk. This will lead to so called MIEC. In our experiments, perovskites in LSCF

($La_{1-x}Sr_xCo_{1-y}Fe_yO_{3-\sigma}$) family are deposited as MIEC part of cathode. Using crystal field theory and taking LSC as an example, LSC composite can be formed by doping Sr in $LaCoO_3$. In LSC, Co^{4+} holes and d electrons are formed and lead to high electronic conductivity. At operation temperature, oxygen molecules are firstly attracted by the reducible transition metals to form O_2^- species and then further share electrons with transition metals to form O_2^{2-} species. Then the O_2^{2-} species will dissociate into two individual oxygen ions and forms O^{2-} species attached to two atoms from transition metals. This high concentration of oxygen ions on the surface of cathode will cause oxygen ions diffusion into the bulk materials. At bulk scale, the ORR in perovskites cathode is also dependent on microstructure of cathode. In our case, we are depositing nano-porous perovskite cathodes, whose microstructure is much complicated than dense thin film cathode. For porous mixed conducting cathode, reaction at gas/solid interface and the transport of oxygen into the bulk are affected by microstructure parameters. Electrochemical impedance spectroscopy (EIS) can give useful information regarding these parameters. For semi-infinite thick porous cathode with no limitation from gas transport, the chemical impedance is co-limited by absorption and transport of oxygen and it can be presented as below[27]:

$$R_{chem} = \sqrt{\frac{4R_{surf}}{\sigma_{i,eff}a}} \tag{1.15}$$

$$C = \frac{4F^2(1-\varepsilon)l_\delta}{RTfV_m} \tag{1.16}$$

where R_{chem} and C are the resistance and capacitance representing the co-limitation from ionic, transport and surface kinetic of the MIEC, $\sigma_{i,eff}$ is effective ionic conductivity and a is surface area, l_δ is characteristic utilization length, ε is the porosity, f is the thermodynamic parameter, and V_m is the molar volume of the oxide. These two equations demonstrate that in the porous electrode, the capacitance is not relied on the thickness of film but on diffusion and kinetic parameters. This type of capacitance is called as Gerischer impedance. To further improve the performance of our cells, we deposit perovskite with other high ionic conducting oxide such as

YSZ and GDC to form composite cathode. This will greatly increase the TPB in cathode and gives much lower cathodic polarization loss. The details of mechanism and performance of this type of composite cathodes will be discussed in later sections.

1.3 Experimental Methods

1.3.1 Anode Aluminum Oxide Porous Substrate

For TF-SOFCs, the substrate plays a very important role. If the substrate pore size is small and uniform, a thin cell without cracks and defects can be produced on the substrate with sufficient fuel mass transport. From this point of view, anodized aluminum oxide (AAO) substrates are a suitable support upon which thin films, especially thin-film electrolytes, can be deposited.[28, 29] AAO is made by anodizing an aluminum sheet where pores of several tens of nanometers are formed and uniformly distributed. Depending on the anodic oxidation conditions, the size of the pore and thus the porosity of the film can be easily manipulated. The tortuosity of AAO can be very low due to the straight and aligned pore structure through the substrate. This ultimately enables fuel to be sufficiently supplied to the cell even with a pore size as small as several tens to one hundred of nanometers.

1.3.2 Deposition of Porous Anodes

On top of AAO substrates, nano-porous anode layers are deposited to oxidize varies of fuels. For the porous anode layer operating in pure hydrogen, sputtering was conducted in an atmosphere of pure Ar at 30-50 mTorr for 50 minutes where Ni (AJA International, USA) and Y/Zr alloy (Advance Engineering Materials, China) targets were co-sputtered onto the porous AAO substrate by DC sputtering with 200 W power for the center 3-inch gun and 200 W power in the side 2-inch gun, respectively. The thickness of the anode film formed under these deposition conditions was about 650-900 nm.

For the porous anode layer operating in hydrocarbon fuels, two different composite anodes are deposited. For ethanol gas fuel, co-sputtering of 3-inch Ru metal, 2-inch Ni and 2-inch GDC ceramic targets were conducted in pure Ar at 30 mTorr for 1 hour by two DC power sources at 100 W, 200 W and by RF power souce at 200 W, respectively. The film thickness is about 1 µm to ensure enough reforming time. For methane gas fuel, co-sputtering of 3-inch Ni metal with 2-inch GDC ceramic targets were conducted in pure Ar at 30 mTorr for 1 hour by 200 W DC power source and 150 W RF power source repectively. The film thickness is about 1 µm. Both of them are deposited on top of aluminum oxide template.

1.3.3 Deposition of Dense Electrolytes

For the dense electrolyte layer, a 3-inch YSZ ceramic target (Advance Engineering Materials, China) was RF sputtered (200 W) in a pure Ar atmosphere at 3-5 mTorr pressure for 3 hours directly on top of the porous anode structure. The dense YSZ film had a thickness of about 1.4-2 µm. For the thin functional GDC interlayer, a 3-inch GDC ceramic target (Advance Engineering Materials, China) was RF sputtered in a 5 mTorr Ar atmosphere at 200 W for 1 hour. The resulting thickness was about 400-500 nm.

1.3.4 Deposition of Porous Composite Cathodes

Development of nano-porous composite cathodes is the focus of this dissertation. The fabrication mechanisms and electronic transport measurements will be discussed in later sessions. Composite cathode are fabricated via co-sputtering 3-inch Y/Zr alloy or Gd/Ce alloy with LSCF or LSC perovskites ceramic targets in pure Ar at 30 mTorr. Alloy targets are deposited by DC power source with power varies from 10-50 W and perovskites targets are deposited with RF power source at 200 W. The thickness of nano-porous cathodes are typically around 1 µm.

1.3.5 Cell configuration and test setup

The test setup is shown in Figure 1.3 and described as follows:

1. Cell configuration: first, the anode is deposited on 1 mm width on AAO substrate.

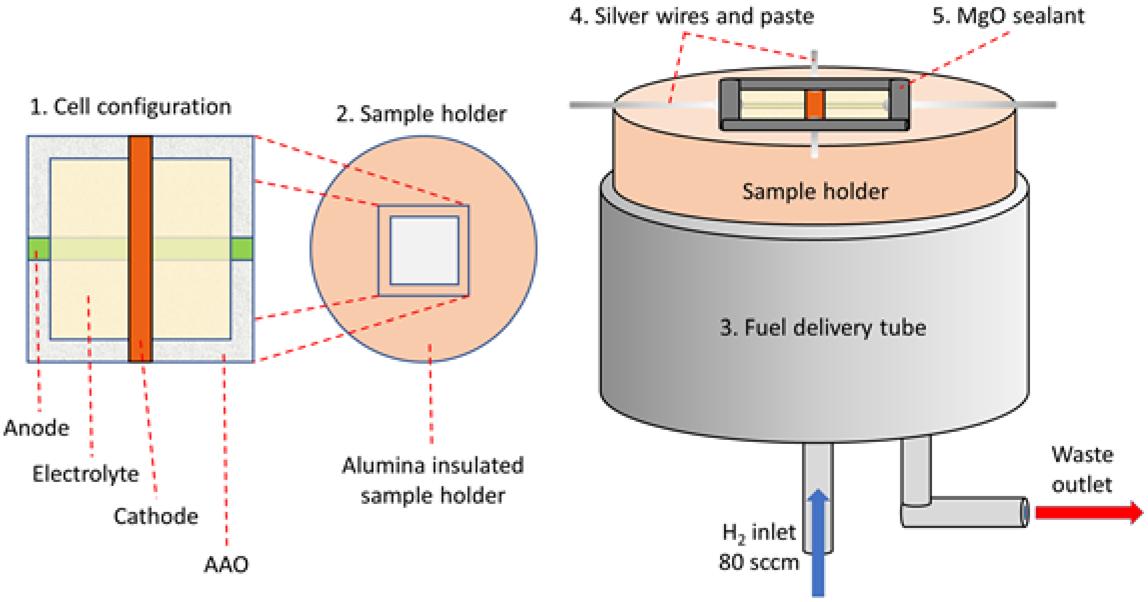

Figure 1.3. Configuration of the cell (left), sample holder (middle) and test setup (right).

Second, a large area of electrolyte is deposited on top of the anode. Lastly, the cathode is deposited with 1 mm width perpendicular to the anode stripe.

2. Sample holder: the fabricated cell is placed onto a 0.9×0.9 cm2 center hole of the alumina sample holder.

3. Fuel delivery tube: the sample holder is mounted onto 1-inch fuel delivery tube. During the measurements, a constant 80 sccm flow rate of H2 fuel is provided to the tube.

4. Current collection wire and paste: 0.5 mm diameter silver wires are connected to the ends of two side of the anode and cathode stripes (1 mm width) via silver paste. The measurements are conducted with a 4-wire configuration. Heated up to 150°C for 1 h to dry up silver paste.

5. Sealing: after connecting the wires to the anode and cathode, MgO sealant is applied around the edge of the cell to prevent any fuel leakage during testing.

1.3.6 Morphology Characterizations

To investigate the crystal structure of the sputtered films and cell structure, grazing incidence X-ray diffraction (GI-XRD) was conducted with a Rigaku SmartLab Diffractometer. To analyze the morphology of the thin-film SOFC, cross sections of the cell were milled using a FEI Scios Dual Beam Focused Ion Beam (FIB) and SEM images were taken by a FEI Apreo SEM using the High-Resolution Immersion Mode. The microscope control software was used to measure film thicknesses using the cross-sectional images and values were corrected for stage tilt. For TEM lamella sample preparation, a common milling and lift-out procedure was conducted by FIB. The samples were mounted onto a Cu TEM lift-out grid (Ted Pella) and subsequently thinned with the FIB to be transparent to the electron beam. The JEOL 2800 TEM was used to image the prepared sample. Scanning mode TEM (STEM) was used and STEM-EDX was performed to illustrate the different cell components. An accelerating voltage of 200 kV was used for all the TEM processes.

1.3.7 Transport Measurements and Electrochemistry Impedance Spectroscopy

To study the electrochemical performance in the fabricated TF-SOFCs, a Gamry Reference 3000 was used for all electrochemistry data collection, including cell OCV, I-V, I-P measurements, and electrochemical impedance Spectroscopy (EIS). To minimize damage from high current densities and overpotentials, the measurements limited the maximum current density and minimum voltage to 7 A/cm^2 and 0.3 V, respectively. In our experiments, four-electrode transport measurements are conducted to fabricated cells. In four-electrode measurement, the working sense lead is separated from the working electrode and the signals is noisy free from the external circus. Galvanostatic mode is used for durability tests to gain a constant output current at working voltage.

EIS characterization tells rich information regarding to the electrochemical reactions, rate limitation steps during the operation and the quality of fabriated TF-SOFCs compared to conventional SOFCs. In EIS characterization, by appyling an AC potential to the TF-SOFCs and then measuring the current response from the cell, one can get the magnitude and the phase of the response signals. The impedances Z of TF-SOFCs can simply be presented by a complex number:

$$Z(\omega) = Z_0(cos\phi + jsin\phi) \tag{1.17}$$

where Z_0 is the impedance magnitude, ϕ is the phase difference in angle. By measuring Z over a wide range of frequency (usually from 0.1 Hz to 1 MHz) and plot real and imaginary part of impedance in X-axis and Y-axis respectively, we can obtain a Nyquist plot as shown in Figure 1.4(a), which can be used to interpret the different electrochemical reactions take place in the fabricated TF-SOFCs. EIS data are commonly analyzed by fitting the curve to an equivalent electrical circuit model as shown in Figure 1.4(b). Equivalent electrical circuit model is a combination of different electrical circuit elements in a specific order. There are a few commonly used elements, such as resistor (R), capactitance (C), and constant phase element (CPE), etc., to describe the possible electrochemical reactions that taking place in the TF-SOFCs. There are some typical combinations of elements to represent some specific chemical reactions. For example, electrolyte is always presented by a resistor in parallel with a pure capacitance denoted as $R//C$. For porous MIEC anode and cathode, they are frequently presented by a resistor in parallel with a CPE denoted as $R//CPE$. After building up the equivalent model as shown in Figure 1.4(b), we can fit the model with EIS data. However, the same EIS data can be fitted by different models, which does not mean these models are physically valid for this TF-SOFC. It is important to build up a reasonable model before fitting the EIS data.

1.3.8 Distribution Function of Relaxation Times

To get quantitatively reliable data for cathode and anode separately, the distributed function of relaxation time (DFRT) method was conducted on the EIS data. DFRT characterization of EIS data is a convenient method to distinguish the different impedance contributions in

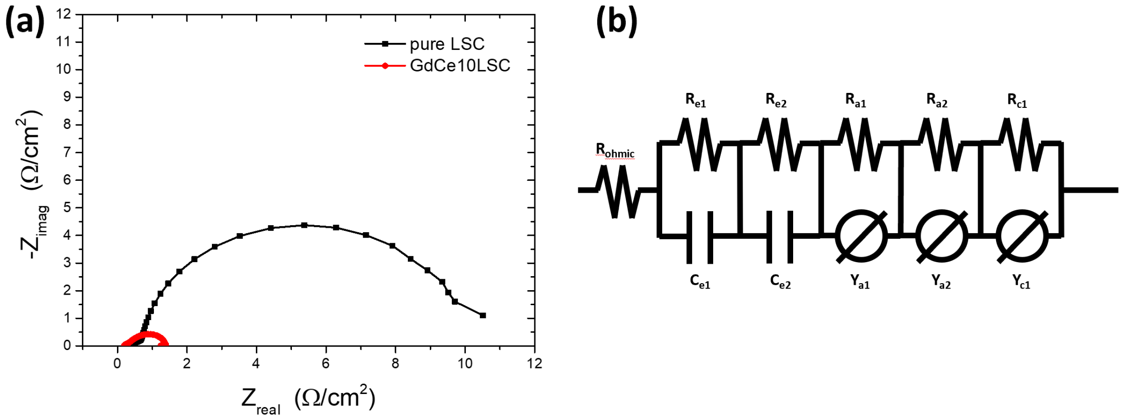

Figure 1.4. (a) Example of Nyquist plot from EIS data of fabricated TF-SOFCs. (b) Equivalent electrical circuit model to fit the EIS data

TF-SOFCs.[30] DFRT transforms EIS data from the frequency domain to the time domain (τ-domain) to distinguish contributions from different processes. The DFRT transforms EIS data into several individual peaks along x-axis and is scaled by $\log(\tau)$, which are characteristic for specific processes that contribute to the electrode impedance. Therefore, its peaks, shown as a function of $G(\tau)$ is not constrained by a specific model. Simply saying, it is trying to solve a Fredholm integral of the second kind for the data inversion. EIS data for the fabricated TF-SOFCs and their transformation to time domain after DFRT transformation are shown in Figure 1.5. After DFRT transformation, contributions of impedance from each individual process in EIS curve can be clearly told apart.

1.4 Development of YSZ-LSCF Cathode

Starting from this session, we will present the development of two different nano-porous cermet cathodes and two different anodes for hydrocarbon fuels operation. The results mainly focus on the fabrication mechanism, characterization of different layers and discussion of electrochemistry of the fabricated TF-SOFCs by EIS data.

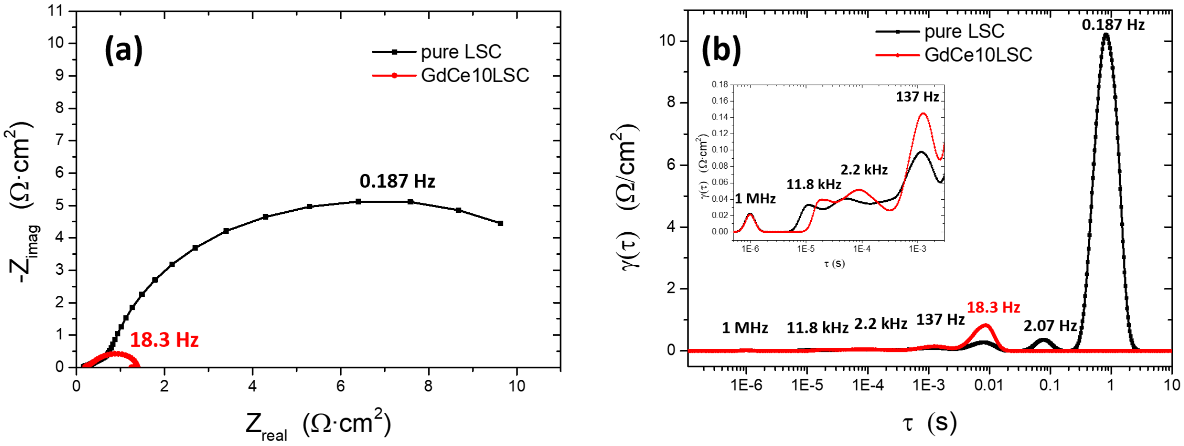

Figure 1.5. (a) EIS data for fabricated TF-SOFCs and (b) data after DFRT transformation to show individual contribution to overall EIS curve

1.4.1 Deposition and Characterizations of YSZ-LSCF Cathode

Depositing LSCF via ceramic sputtering targets usually results in a dense structure owing to a rare atomic shadowing effect.[19] In this case, directly sputtering ceramic LSCF electrode can only result in dense films as shown in Figure 1.6(a), no matter if the sputtering process parameters were changed. Alternatively, a metallic yttrium/zirconium (Y/Zr) alloy film through direct current (DC) sputtering can easily yield columnar growth of the Y/Zr alloy, which in turn has a much lower adatom mobility, thus a better atomic shadowing effect. Ultimately, this effect results in a porous structure (Figure 1.6(a)). Taking inspiration from this result, it follows that it could be possible to sputter two materials together, or cosputter, to fabricate a porous LSCF-YSZ cathode. Co-sputtering was previously used to create composite films such as Ni-YSZ anode composites.[31] Thus, cosputtering of LSCF and Y/Zr could also be used to create a porous cathode structure.

To fabricate a porous LSCF-based electrode, cosputtering of Y/Zr metal alloy and LSCF targets was performed. Since Y/Zr can be easily formed into a porous film at high Ar pressures, the cosputtering of LSCF and Y/Zr could yield a porous film of LSCF-YSZ using similar conditions. The resulting cosputtered LSCF-YSZ film has a porous, columnar nanostructure as shown in the SEM images in Figure 1.6(c). According to the images, this columnar structure

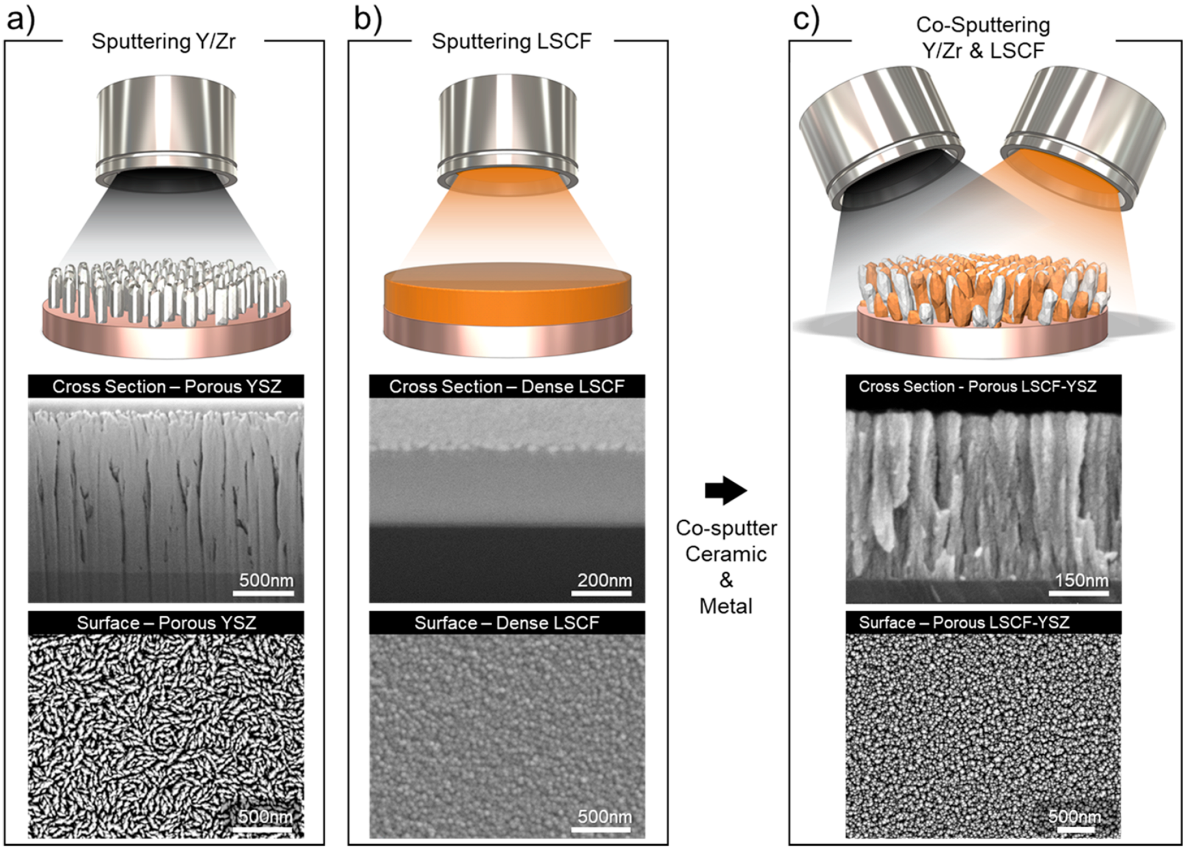

Figure 1.6. Schematic of sputtering metal, ceramic, and cosputtering of metal and ceramic. (a) Sputtering of a Y/Zr metal alloy target and the corresponding porous YSZ cross-sectional and surface SEM images. (b) Sputtering of a LSCF ceramic target and the corresponding dense LSCF cross-sectional and surface SEM images. (c) Co-sputtering of Y/Zr and LSCF and the corresponding porous LSCF-YSZ cross-sectional and surface SEM images. Two hundred watts was applied to the LSCF ceramic target and 50 W was applied to the Y/Zr target.

has a diameter of tens of nanometers, thus creating a very large active surface area. The desired growth mechanism takes place as long as the following occur at the start of cosputtering: (1) Atoms sputtered from Y/Zr target combine into a cluster of particles at high pressure in the chamber. This leads to a low adatom mobility in sputtered Y/Zr atoms and they are more likely to create many well-separated growing nuclei on the room temperature substrate. (2) LSCF with a lower volume ratio prefers to stay on the surface of the Y/Zr (this is aided further by oxygen atoms).[32] (3) A high-processing Ar pressure scatters the sputtered atoms in the chamber, making atoms sputter at larger angles. This enhances the sputtering rate at high points but lowers the rate at valleys due to the shadowing effect, which in turn makes columnar growth more dominant.

To fully understand the growth mechanism of the porous columnar LSCF-YSZ shown in Figure 1.6(c), LSCF-YSZ was deposited with different LSCF-to-Y/Zr ratios (Figure 1.7). The power applied to the LSCF target was fixed to 200 W and the power applied to the Y/Zr target was varied to compare the microstructure of various LSCF-YSZ cosputtered composites.

According to the images of LSCF-YSZ deposited at 20 W for Y/Zr (Figure 1.7a,b), a mesoporous structure was seen on the surface image, but the cross-sectional image showed that the pores were not fully connected through the cathode to the interface of the substrate. Thus, although such an electrode would have a large surface area, without continuous pores, air could not be efficiently delivered to the triple phase boundary (TPB). When the Y/Zr target is increased to 30 W, the size of the particles increased by about two times and the microstructure became relatively more porous. However, discontinuous pores are also similarly observed for the 30 W-sputtered Y/Zr. While the surface image of LSCF-YSZ deposited with 40 W Y/Zr power was similar to that of the film deposited at 30 W, the nanostructure observed by the cross-sectional image for 40 W Y/Zr was different; at 40 W, the pores have become completely continuous from the inlet to the substrate surface. As the number of particles of metallic Y/Zr increased during the deposition of LSCF-YSZ, the higher rate of the shadowing effect resulted in a columnar structure with greater porosity.

Through calculating the LSCF and YSZ deposition rates, it was confirmed that if the YSZ content of LSCF-YSZ exceeds about 50%, the thin film will show a highly porous columnar structure. Our LSCF-YSZ used for cell fabrication was deposited at 50 W for Y/Zr and 200 W for LSCF. This increase to 50 W, which meant that the YSZ content is slightly higher than that at the 40 W critical point, was chosen so that a porous film can be fabricated consistently and reliably. Figure 1.6c illustrates the morphology using these conditions.

According to the XRD analysis as shown in Figure 1.8, peaks from LSCF and YSZ are observed and the nonconducting secondary phases of $La_2Zr_2O_7$ and $SrZrO_3$ were not generated.

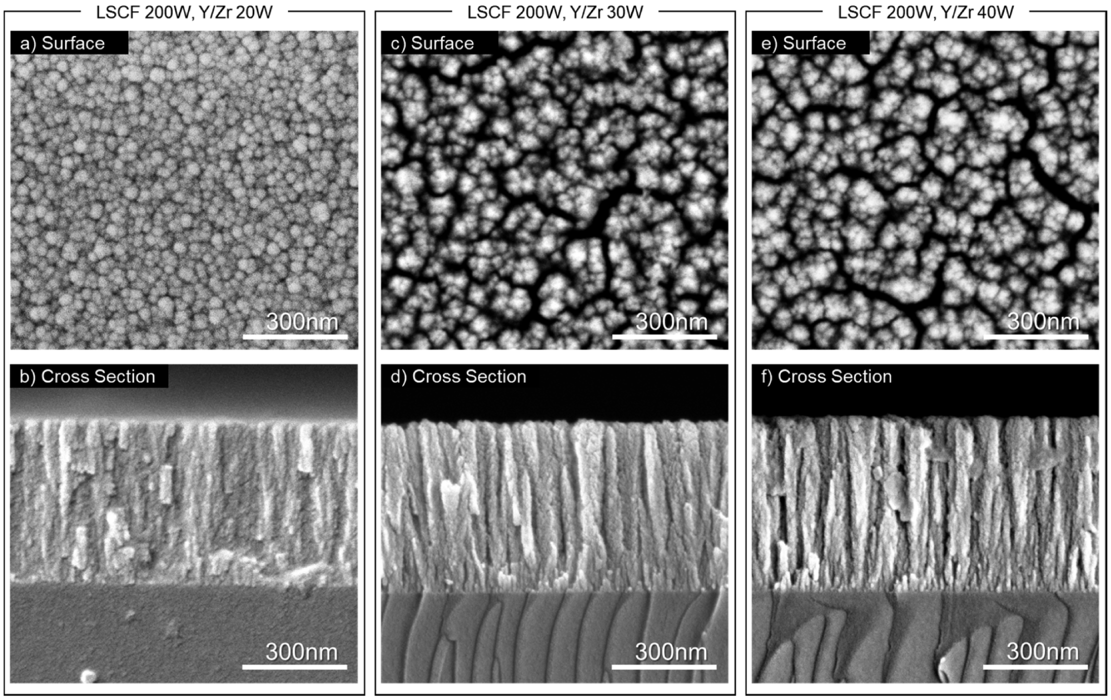

Figure 1.7. Surface and cross-sectional images of LSCF-YSZ with different LSCF-to-YSZ ratios. (a) Surface and (b) cross sectional FE-SEM image of LSCF-YSZ deposited by cosputtering at 200 W for LSCF and 20 W for Y/Zr. (c) Surface and (d) cross sectional FE-SEM image of LSCF-YSZ deposited at 200 W for LSCF and 30 W for Y/Zr. (e) Surface and (f) cross sectional FE-SEM image of LSCF-YSZ deposited at 200 W for LSCF and 40 W for Y/Zr.

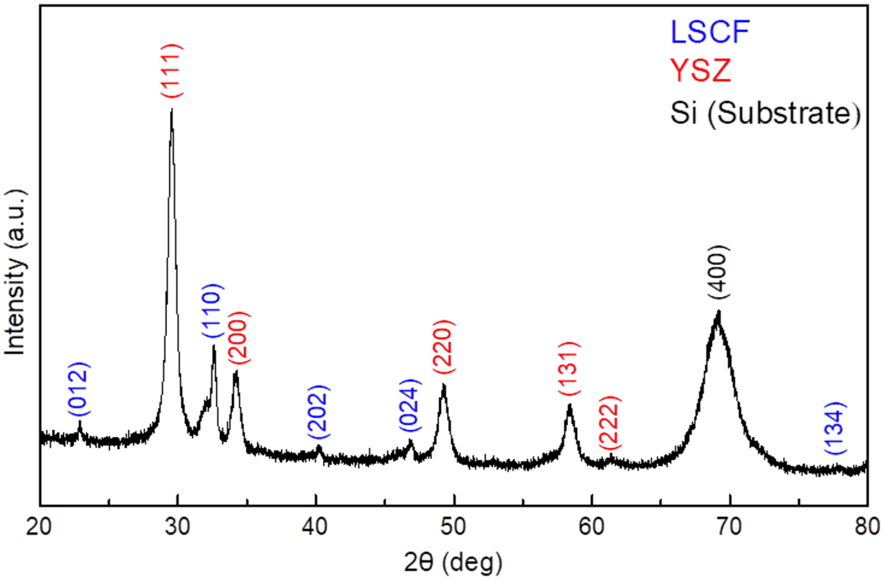

Figure 1.8. GI-XRD pattern of the sputtered LSCF-YSZ composite cathode. The blue Miller indices correspond to LSCF and the red Miller indices correspond to YSZ. No new or additional peaks are seen. The large peak at 70° comes from the Si wafer substrate, as the cathode was deposited on a Si wafer substrate.

This is due to the room-temperature deposition and 600 °C annealing; the thermal energy of the plasma during sputtering was not sufficient to support the formation of secondary phases.[33] Both LSCF peaks and YSZ peaks are clearly showing up in the figure, indicating a composite cathode is fabricated.

1.4.2 Function of GDC interlayer

A GDC interlayer[34] was deposited between the electrolyte and the cathode. Both the sputtering power and substrate location in the chamber were varied for GDC. The plasma emitted from the sputter gun is most intensely delivered to the center part of the substrate. This greatly affects the microstructure of the deposited thin film by ion bombardment and re-sputtering. To clarify the effect of plasma emission to the sample, samples were placed in different locations (Figure 1.9) and the corresponding nanostructures of the GDC thin films were analyzed by FIB and FE-SEM (Figure 1.10 and 1.11). Figure 1.10 shows electron microscope images of the cross-section and surface of the GDC film deposited at the center of the substrate (Figure 1.10(a) and Figure 1.10(c), respectively), and the edge of the substrate (Figure 1.10(b) and Figure 1.10(d), respectively), located at about 5cm from the center. The GDC deposited at the center of the substrate shows defects and pores, but the film deposited at the edge shows a defect-free dense structure. As the plasma emitted from the sputtering target has high energy and thus many electrons are emitted, this can result in damage and re-sputtering of the film surface. Since the thin film deposited at the center is exposed to a higher density of plasma, this causes defects and surface irregularities as shown in Figure 1.10(a) and Figure 1.10(c). Since the intensity of the plasma is lower at the edge of the substrate than at the center, damage and re-sputtering of the thin film are reduced, and a more dense and uniform thin film results (Figure 1.10(b) and Figure 1.10(d)). In order to confirm whether the plasma damage is due to the difference in the substrate position, the power output is reduced to 100W (Figure 1.11). As a result of lowering the power, the GDC thin film was found to also be dense and defect-free regardless of the sample position. According to these results, it is necessary to either place the sample on the edge or reduce the output power of the sputter gun to avoid plasma damage and thus deposit defect-free dense layers.

The cathode functional layer (CFL) between the cathode and electrolyte has been widely studied in the past decade. It has multiple benefits for the intermediate-temperature SOFC, such as having better electrical conductivity for cathode current collection, acting as barrier to limit any reaction between the cathode and electrolyte, and decreasing the activation energy for the ORR. In our study, a dense GDC functional layer is sandwiched between the LSCF-YSZ cathode and YSZ electrolyte via RF sputtering to reduce cathodic overpotential. The as-deposited GDC layer shows a uniform, smooth, and dense structure as previously shown. GI-XRD was also performed on the as-deposited film and after operation under 600°C for 1h, as shown in Figure 1.12. The XRD data clearly shows that the peaks of the as-deposited GDC films are broadened and asymmetric. As we heat up the film to 600°C and measure the same sample again, the peak shifts to the right and becomes sharp and symmetric. This effect in consistent with literature;

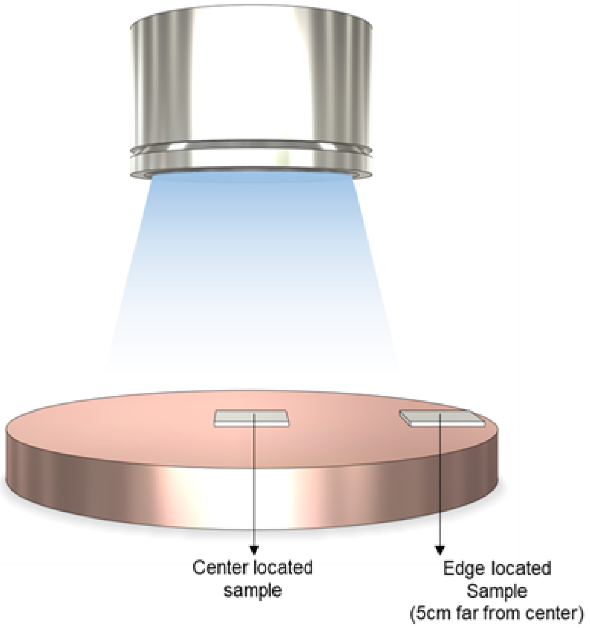

Figure 1.9. Sputtering configuration for films deposited at different locations.

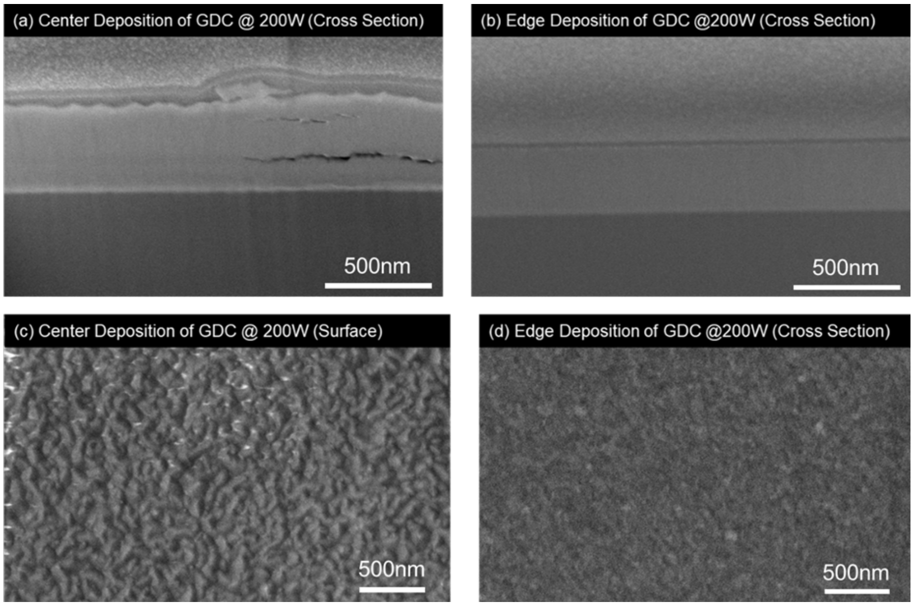

Figure 1.10. Surface and cross-sectional images of GDC films deposited under 200W with varying substrate location.

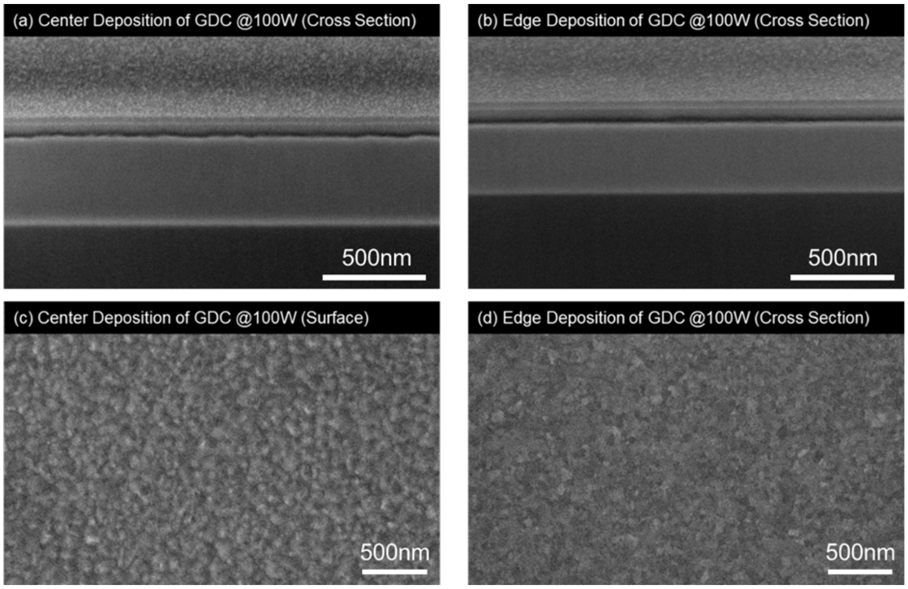

Figure 1.11. Surface and cross-sectional images of GDC films deposited under 100W with varying substrate location.

as-deposited GDC was found to mostly consist of the oxygen-deficient Ce4O7 phase, but changes phase to GDC at elevated temperatures1. Rather than use a high annealing temperature of 900°C, since we operate our TF-SOFC at 600°C, we characterized the same GDC film after annealing for one hour at 600°C. The resulting XRD pattern shows the formation of GDC with a much sharper peak as a result of strain release and grain growth. It is important to note that in our cells, there is no need for any separate or additional annealing processes for both the formation of LSCF and GDC, since from the XRD data, the cell operation temperature is sufficient for the formation of GDC functional layer. This is a big advantage when considering simplicity in large-scale fabrication.

1.4.3 Full Cell Fabrication and Characterization

The anode, electrolyte, interlayer, and cathode were sequentially sputtered onto the porous AAO and shown schematically in Figure 1.13 and the corresponding STEM micrograph in Figure 1.13a. Figure 1.13b-d shows the STEM images and Figure 1.13e-g shows the corresponding SEM images of the surface morphology of each component. With this configuration, no etching

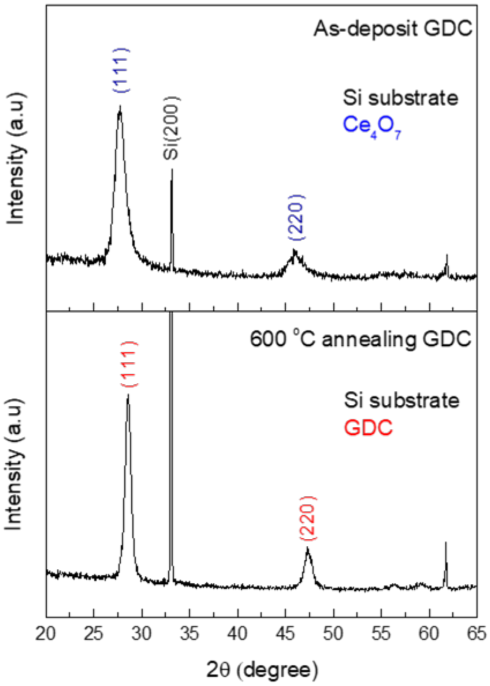

Figure 1.12. GI-XRD pattern of as-deposited (black) GDC and after heating GDC to 600°C for one hour (red). The Si(200) peak comes from the Si wafer substrate, where GDC was deposited upon.

or patterning steps were required between sputtering of the different films. One clear benefit was that the samples were kept under vacuum during the fabrication process, especially for complete cells, and thus ambient contamination was minimized since sputtering was done sequentially in the same chamber.

A 700-nm Ni-YSZ porous anode layer was deposited onto the AAO. As shown in Figure 3a,b, the Ni-YSZ electrode is formed as a collection of larger columns with a diameter of about 200 nm with smaller columns of less than 10 nm in diameter on top of the 200 nm columns. The surface morphology of Ni-YSZ (Figure 1.13e) showing hexagonally arranged columns that do not completely block the pores of the AAO. This microstructure provides a very high active surface area for the anode, thus significantly improving electrode performance. Figure 1.14a shows the distribution of the elements through STEM-EDX analysis of the Ni-YSZ electrode. The YSZ electrolyte and the GDC interlayer were deposited on top of the Ni-YSZ anode. As

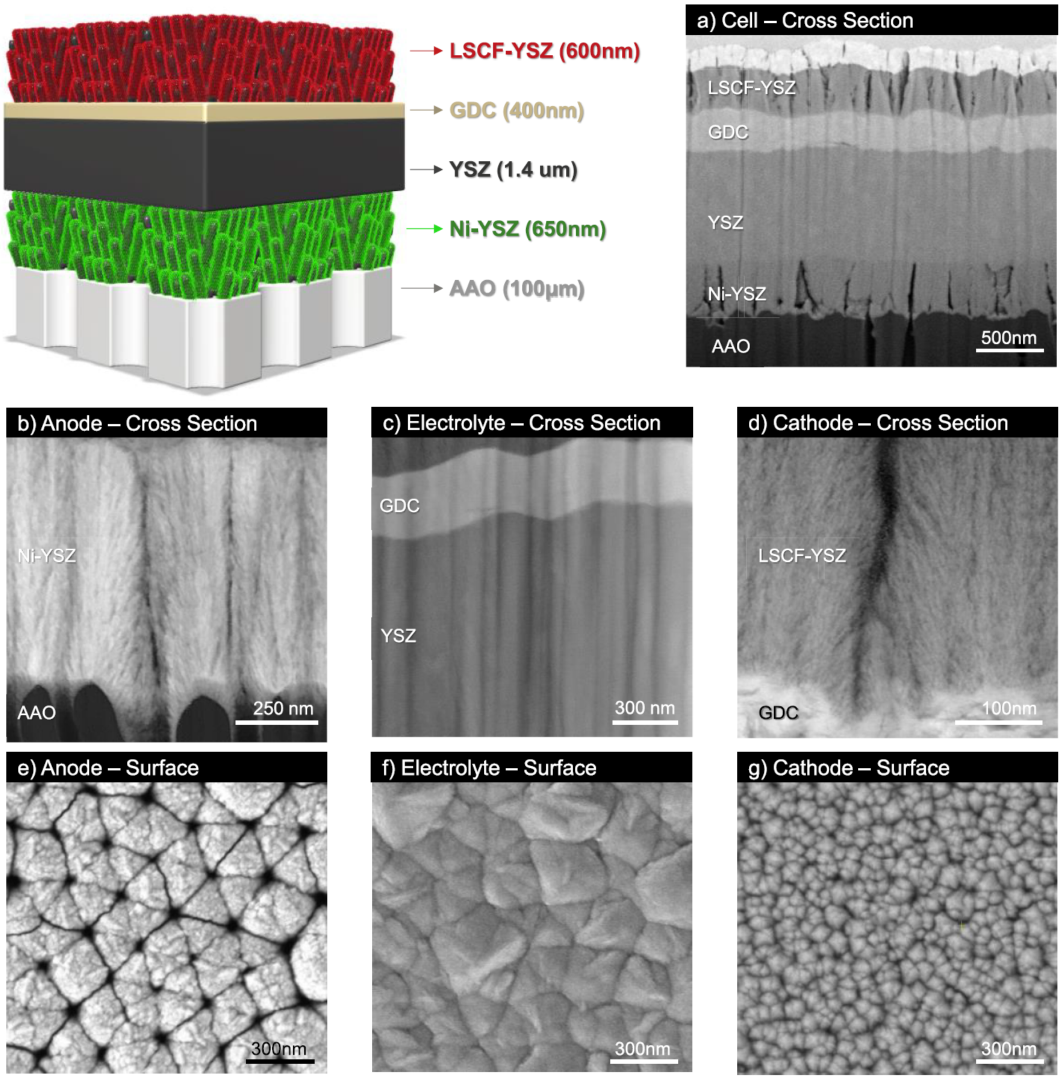

Figure 1.13. Schematic of the cell architecture. (a) Cross section FE-SEM image of the cell architecture. STEM view of the (b) anode, (c) electrolyte with interlayer, and (d) cathode, respectively. Respective FE-SEM surface images of (e) Ni-YSZ layer on AAO, (f) GDC layer on top of AAO/Ni-YSZ/YSZ, and (g) LSCF-YSZ layer on top of AAO/Ni-YSZ/YSZ/GDC.

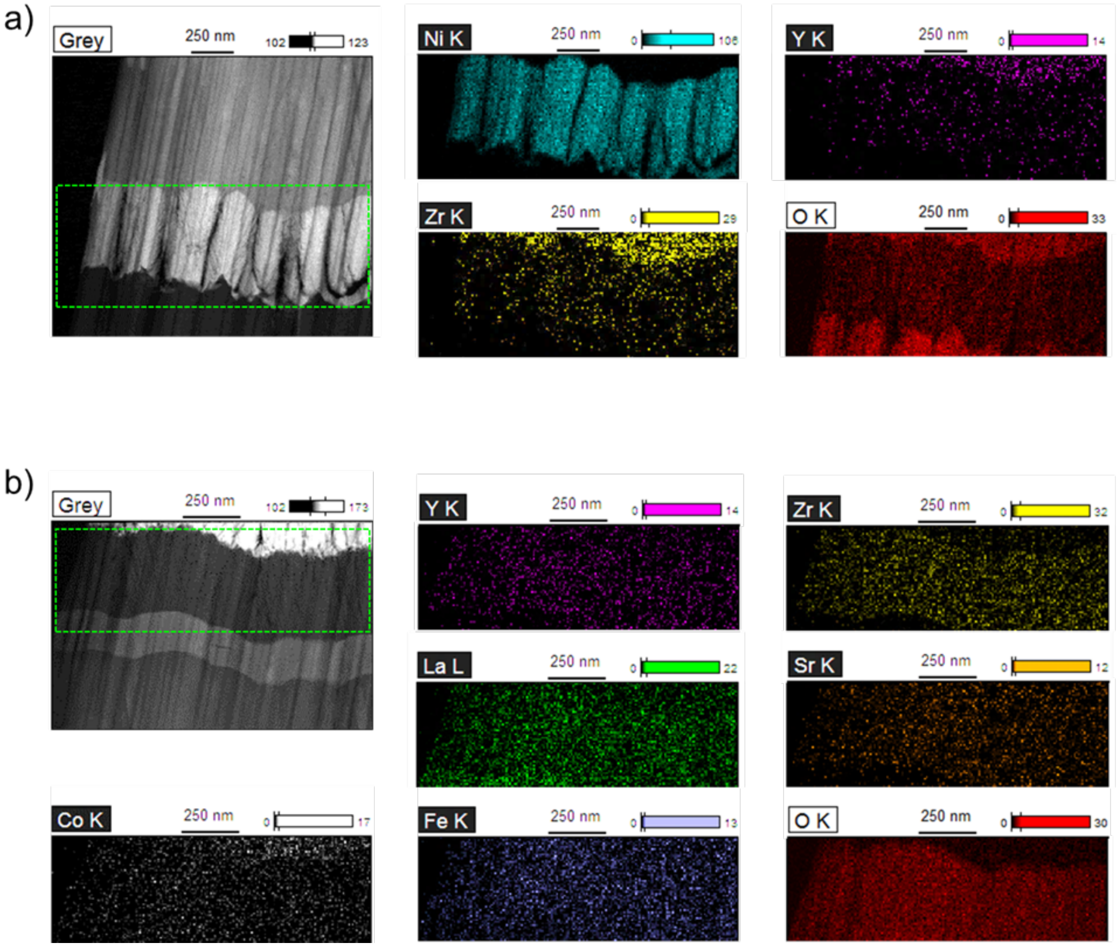

Figure 1.14. STEM-EDX of (a) the Ni-YSZ anode structure and (b) the LSCF-YSZ cathode structure.

seen in Figure 1.13a, the YSZ electrolyte has a thickness of about 1.4 μm, relatively thick considering a previous report of 150 nm YSZ electrolytes applied to AAO-based SOFCs. While thin electrolytes can increase performance, the trade-off is that structural defects in fabrication leading to cell failure during operation is more likely to occur. Since structural defects occur in proportion to the cell area, this issue is significantly exacerbated when applying an ultrathin electrolyte to a large-active-area cell. With these considerations, a relatively thick electrolyte was applied in this study. Even with a high electrolyte thickness, the cells are still capable of achieving exceptional power densities.

The LSCF-YSZ cathode was then deposited on the top of the GDC interlayer. The

LSCF-YSZ shows an extremely fine nanofibrous structure with a diameter of less than 10 nm and relatively large openings between the columns, which ensures high mass transport of oxygen to the whole cathode as well as a large active surface area. As the LSCF target has a composition of $La_{0.6}Sr_{0.4}Co_{0.2}Fe_{0.8}O_{2.95}$, STEM-EDX of LSCF-YSZ in Figure 1.14b shows that the signals from La and Fe are more intense than those of Sr and Co; however, to examine the exact stoichiometry of the sputtered LSCF films, further work involving different characterization techniques is required. The SEM, STEM, and STEM-EDX results nevertheless show that each component of the TF-SOFC with distinct nanostructures have been successfully deposited via magnetron sputtering.

1.4.4 Cell Performance and Electrochemical Measurements

Electrochemical analysis of the TFSOFC is shown in Figure 1.15 and a schematic of the test cell setup is shown in Figure 1.3. The cell has active area of 1 mm^2 (1 mm × 1 mm) and was tested under pure hydrogen at a flow rate of 50 sccm and exposed to air for the oxygen source. Our tested cells show an open-circuit voltage (OCV) of 0.95 V and a peak power density of 1.7 and 2.5 W/cm^2at 600 and 650 °C, respectively (Figure 1.15a), the highest recorded power density for YSZ-based SOFC devices. According to the EIS measurement shown in Figure 1.15b, relatively low polarization losses were observed at both 600 and 650 °C. Since the cosputtered Ni-YSZ electrode and the LSCF-YSZ electrodes consist of nanofibers of less than 10 nm in diameter, the number of reaction sites in the electrodes were significantly increased. In conjunction with Figure 3a,b,d, since the relatively larger vertical pores are formed in the electrodes at every 100-200 nm, the fine microstructure among these larger pores ultimately results in more effective gas delivery.

In terms of materials, a mixture of LSCF and YSZ will increase the triple phase boundary compared to pure LSCF electrodes. Since YSZ has low electrical conductivity, it is required to analyze the effect of the YSZ mixture in LSCF in terms of electrical conductivity and polarization losses. According to the comparison in Figure 1.16, the peak power density for the TF-SOFC

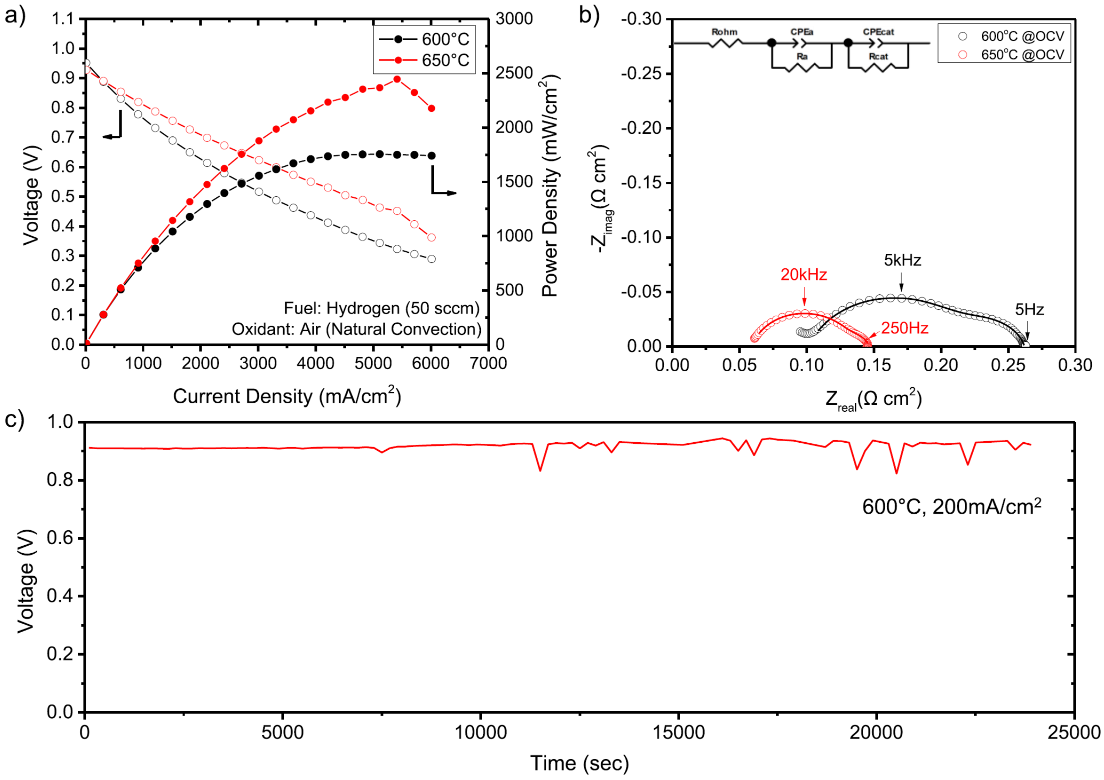

Figure 1.15. (a) Current-voltage (I-V) and current-power (I-P) curves and (b) EIS measurement of the TF-SOFC with hydrogen fuel and air at 600 and 650 °C, respectively. The lines on the Nyquist plot correspond to the respective fits from the equivalent circuit in the inset. (c) Short-term stability test; the cell voltage was measured over time while applying a constant current of 200 mA/cm^2.

Table 1.1. Impedance contributions from the EIS fitting at 600°C for Pure LSCF and LSCF-YSZ with their corresponding frequency ranges.

Component	LSCF (Ω cm^2)	LSCF-YSZ (Ω cm^2)
R_{ohm}	0.0515	0.1015
R_a	0.0242 (100kHz-10kHz)	0.0439 (100kHz-10kHz)
R_{cat}	0.5204 (10kHz-3Hz)	0.1167 (10kHz-5Hz)
R_{pol}	0.6254 (3Hz-0.3Hz)	n/a

with pure LSCF as the cathode was about 550 mW/cm^2 at 600 °C, about a third of that compared to the LSCF-YSZ composite at the same temperature. According to the EIS fitting results in Table 1.1, although pure LSCF has a lower ohmic resistance by about 0.05 Ω cm^2, its overall polarization resistance (R_{cat}+ R_{pol}) is much greater (by over 1 Ω cm^2). In other words, even though cosputtering of YSZ with LSCF slightly increases the ohmic resistance, it drastically reduces the polarization loss, which is consistent with the increased cell performance and peak power density measurements. In Figure 1.16(b), the Nyquist plot for pure LSCF seems to have a different shape and could not be fit with the same equivalent circuit used for LSCF-YSZ. This means there is seemingly an additional impedance contribution for pure LSCF. There can be a couple of factors behind this contribution: one is that pure LSCF has a lower ionic conductivity than the composite LSCF-YSZ, but another possible factor is that the as-deposited pure LSCF had many non-continuous/closed/restricted pores that contained trapped argon gas (as the film was deposited under an Ar atmosphere). This leads to a comparatively much lower oxygen concentration and thus a concentration overpotential, resulting in poor cell performance. Thus, the additional impedance contribution is designated as R_{pol}. It is important to note that the largest impedance contributions for pure LSCF are observed at the low frequency region; LSCF-YSZ, which has a much more porous microstructure, mitigates this issue, and cell performance is improved as a result.

In order to investigate the cell durability or the cell performance over time, the voltage was measured at a constant current of 200 mA/cm^2 at 600 °C and the results are shown in Figure 1.15c. This short-term stability test was performed for about 7 h where the cell showed a constant

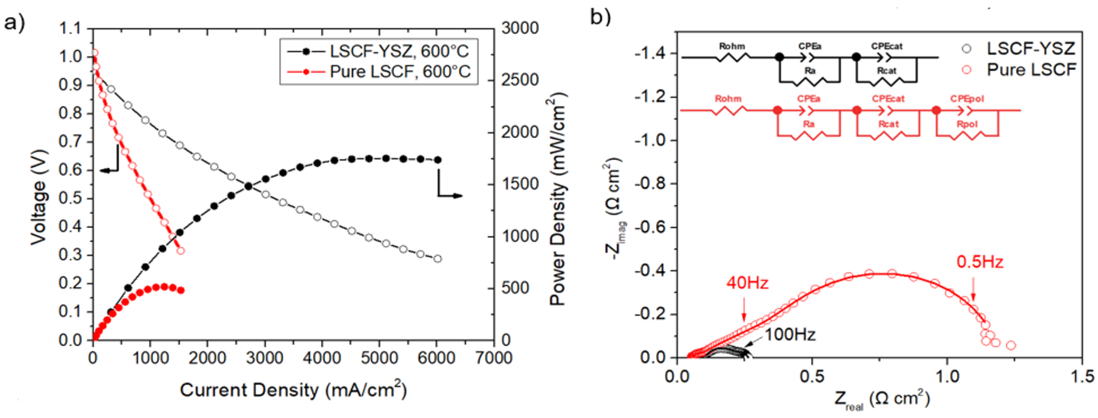

Figure 1.16. (a) current-voltage (I-V) and current-power (I-P) curves and (b) EIS measurement of the TF-SOFC using pure LSCF and LSCF-YSZ cathode with hydrogen fuel and air at 600°C. The lines in the Nyquist plot correspond to the respective fits from the equivalent circuits in the inset.

voltage without significant degradation. It should be noted that if the cell was operated at the peak power density for extended periods of time without air cooling, the cells tended to fail because of the large amount of heat generated from the high current density.

1.4.5 Summery of YSZ-LSCF Cathode

In summary, TF-SOFCs (3 μm thick) on AAO substrates were fabricated via a sputtering process for all of the cell components, which were composed of conventional materials (YSZ for the electrolyte, GDC for the electrolyte/cathode interlayer, Ni-YSZ for the anode, and LSCF-YSZ for the cathode). Fully dense YSZ and GDC films, along with porous Ni-YSZ and LSCF-YSZ films with columnar nanostructures (that yield a high active surface area) were successfully developed and fabricated. Electrochemical evaluations of the cell showed an OCV of 1.0 V and exceptional peak power densities of 1.7 and 2.5 W/cm^2 with hydrogen fuel and air at 600 and 650 °C, respectively. Further work is ongoing to refine the cell architecture, optimize and scale up the fabrication process, evaluate long-term performance stability, and investigate cell operation with different hydrocarbon fuels.

1.5 Development of GDC-LSC Cathode

In this section, we report the electrochemical performance and structural characteristics of porous nanostructured ceramic cathodes for thin-film solid oxide fuel cells (TF-SOFCs) based on yttria-stabilized zirconia (YSZ) electrolytes. The nanostructured cathode is obtained through magnetron cosputtering of gadolinium-cerium (Gd-Ce) alloy and lanthanum strontium cobaltite perovskite targets. The resultant nanostructure and composition of the ceramic cathode are controlled by adjusting the co-sputtering conditions. The peak power densities in our fabricated TF-SOFCs are the highest reported values for YSZ-based electrolyte SOFCs, showing 0.14, 0.48, 1.21, 2.56, and 3.01 W/cm2 at 450, 500, 550, 600, and 650 °C, respectively, operating under air and pure hydrogen fuel. The results show that the porosity and composition of the cathode greatly affect the resulting peak power densities. This work illustrates the capability of sputtering to produce stable, scalable, nano-ceramic cathodes with superb peak power densities when integrated in TF-SOFCs.

1.5.1 Deposition of GDC-LSC Cathode

In this work, we report the results of our study on YSZ-based TF-SOFCs with the lanthanum strontium cobaltite perovskite (LSC)-gadolinium-doped ceria (GDC) cathodes. Adding GDC into the MIEC perovskite to form a porous composite cathode greatly improves the performance by increasing the ionic conductivity of the perovskite cathode[35, 36, 37] and improves the stability by minimizing microstructural changes during operation. To combine the advantages of sputtering metals and ceramic oxides, as noted in our previous work,[38] we conducted co-sputtering of a metal alloy target, $Gd_{0.2}Ce_{0.8}$ (Gd-Ce), with a ceramic LSC target, $(La_{0.6}Sr_{0.4})_{0.98}CoO_3$. Figure 1.17c shows transmission electron microscopy images (TEM, in scanning mode) of a cosputtered nanostructured ceramic cathode. From the image, we can observe two distinctive porous features: one being columnar structures with large openings between each structure and the other being 10 nm diameter nanofibers which grow a branch-like nanostructure on a large columnar structure; such columnar structures have been observed previously and are caused by shadowing effects during deposition.[39, 40, 41] The nanofiber-like columnar nanostructure is an ideal structure for the cathode of TF-SOFCs since the openings ensure sufficient oxygen mass transport while the nanosized structure increases the effective active area. Furthermore, the co-sputtered GDC enhances mixed conductivity of the cathode, creating more triple-phase boundaries (TPBs) for the ORR process. The configuration of the full TF-SOFCs is illustrated in Figure 1.17a. The key to grow a nanoporous structure is to grow the sample in the zone 1 region of the Thornton diagram, or the so-called column growth region.[19] The growth mechanism, demonstrated in previous work,[38] is shown in Figure 1.17d. Porous anodized aluminum oxide (AAO) templates with a nanostructure of well-defined and uniform pores (100-250 nm) were used as the substrate. In previous works,[38, 31] porous AAO templates have been shown to be a suitable substrate for TF-SOFCs. In our study, 100 μm thick AAO templates with a 120 nm pore size were used as the supporting substrate. For the anode, Ni and Y-Zr were co-sputtered to form a 900 nm thick porous anode nanostructure. For the electrolyte, YSZ was used. To avoid potential chemical reactions between the perovskite cathode and YSZ electrolyte and reduce the interfacial transport loss, dense and thin GDC was used as an interlayer between the cathode and YSZ electrolyte. The thicknesses for the GDC and YSZ layers were 500 and 1900 nm, respectively. For the cathode, a porous ceramic LSC-GDC cathode was deposited on the GDC by co-sputtering with a thickness around 800-1000 nm. A 300 nm thick Pt layer was deposited on the cathode as a current collector.

The detailed deposition conditions are followed: the sputtering power for the Gd-Ce target was set in the range of 0-50 W with a DC power source and the LSC target was sputtered at a constant 200 W with a RF power source. The co-sputtering processes all ran under pure Ar environment at room temperature. The base pressure was below 5×10^{-7} Torr before conducting sputtering. During sputtering, the Ar pressure was kept at 30 mTorr and the distance between target and substrate keeps at about 4 cm. Other cell components were also fabricated by sputtering. To deposit the porous anode layer, 3-inch Ni and 2-inch Y-Zr alloy targets were co-sputtered

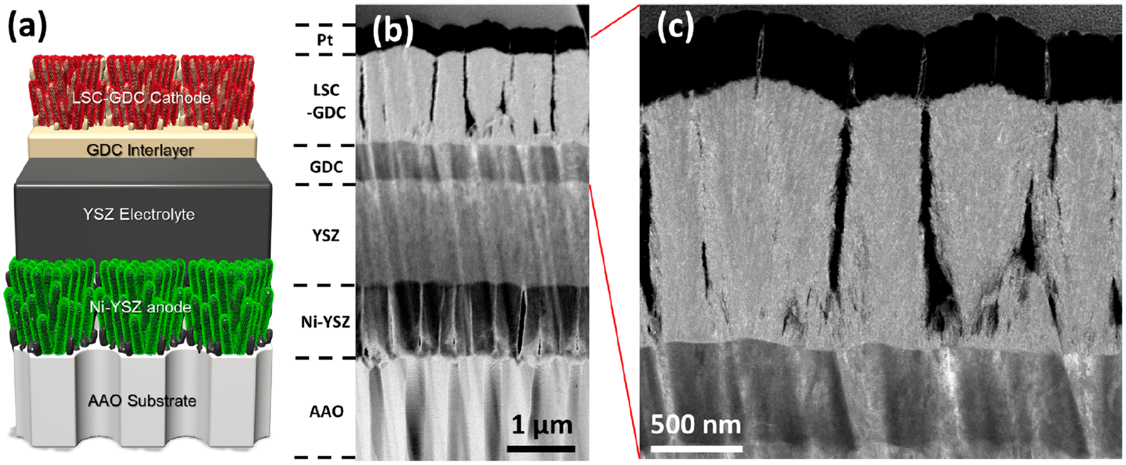

Figure 1.17. (a) Configuration of TF-SOFC. (b) Dark field cross-sectional STEM image of the sputtered TF-SOFC. (c) Dark field cross-sectional STEM image of the nano-ceramic cathode. (d) Schematic of the co-sputtering process and the deposited nano-ceramic cathode nanostructure and column growth process.

using two different DC power sources at 200W simultaneously for 50 mins. 50 sccm flow rate of pure Ar was continuously supplied to the chamber and the sputtering pressure maintained at 30 mTorr during the deposition process. The anode was directly deposited on the rough surface of AAO templates. The resulting thickness was about 900 nm. For the dense electrolyte and interlayer, a 3-inch YSZ ceramic target and a 3-inch GDC ceramic target were both sputtered with RF power source at 200 W power in a pure Ar atmosphere supplied at constant flow rate of 50 sccm. The YSZ layer was deposited at 3 mTorr for 5 hours, resulting in a thickness about 1.9 µm. The GDC layer was deposited at 2 mTorr for 1 hour, resulting in a thickness about 500 nm. The STEM image for the full cell is shown in Figure 1.17b, which shows the nanostructure for each layer schematically depicted in Figure 1.17a. Energy-dispersive X-ray spectroscopy (EDX) mappings conducted on the sputtered cathode and anode (shown in Figure 1.18), generally indicate the correct distribution of the different elements. The signal intensities for different elements are consistent with the ratio of each element.

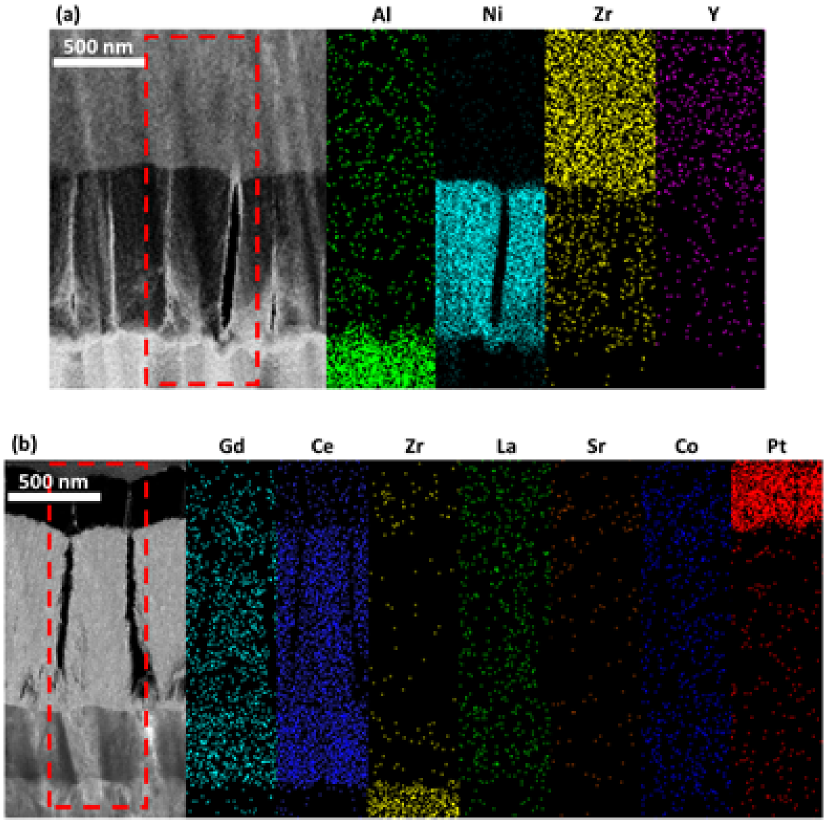

Figure 1.18. (a) EDX mapping for the anode side and (b) for the cathode side.

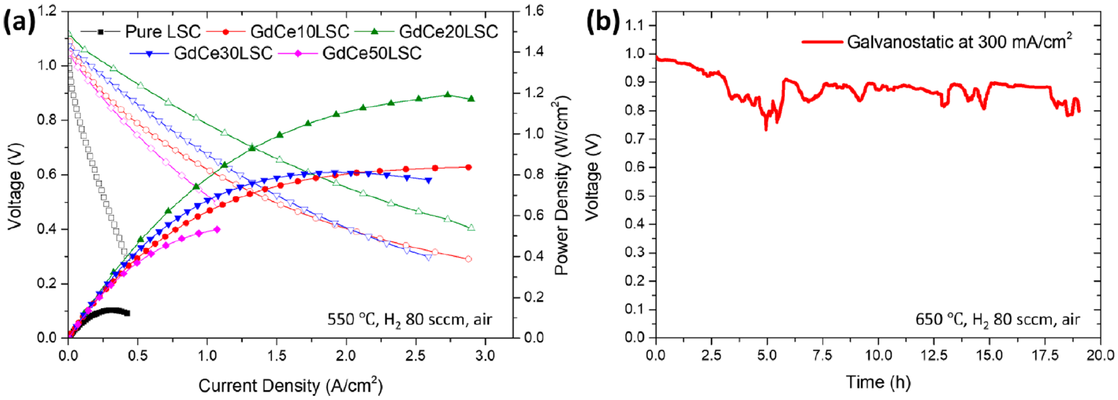

Figure 1.19. (a) Current density vs voltage and power density characteristics for LSC-GDC/GDC/YSZ/Ni-YSZ at 550 °C. (b) Durability test measured at 650 °C at a constant current density of 300 mA/cm^2.

1.5.2 Controlled Deposition of Morphology and Composition in Cathodes

To systematically study the effects of the deposited cathode nanostructure and composition over the performance of TF-SOFCs, a series of cells with different cathode compositions were fabricated via controlling the sputtering conditions. The cathodes were co-sputtered by using a constant power of 200 W for the LSC target and varying the power of the Gd-Ce alloy target (0, 10, 20, 30, and 50 W). The cathodes are denoted as pure LSC, GdCe10LSC, GdCe20LSC, GdCe30LSC, and GdCe50LSC, respectively. The active area in our cells is 1 mm^2, and the configuration of the cell and the test setup are provided in Figure 1.3. Potentiostatic, galvanostatic, and power polarization modes for the Gamry Reference 3000 were used to measure the electrochemical properties of the fabricated TF-SOFCs. To minimize damage from high current densities and overpotentials, the measurements limited the maximum current density and minimum voltage to 7 A/cm^2 and 0.3 V, respectively. The current density-voltage (I-V) curves and power density (PD)-current density curves (measured at 550 °C) are shown in Figure 1.19a for the different sputtered cells. Measurements conducted at 450, 500, 600, and 650 °C are shown in Figure 1.20.

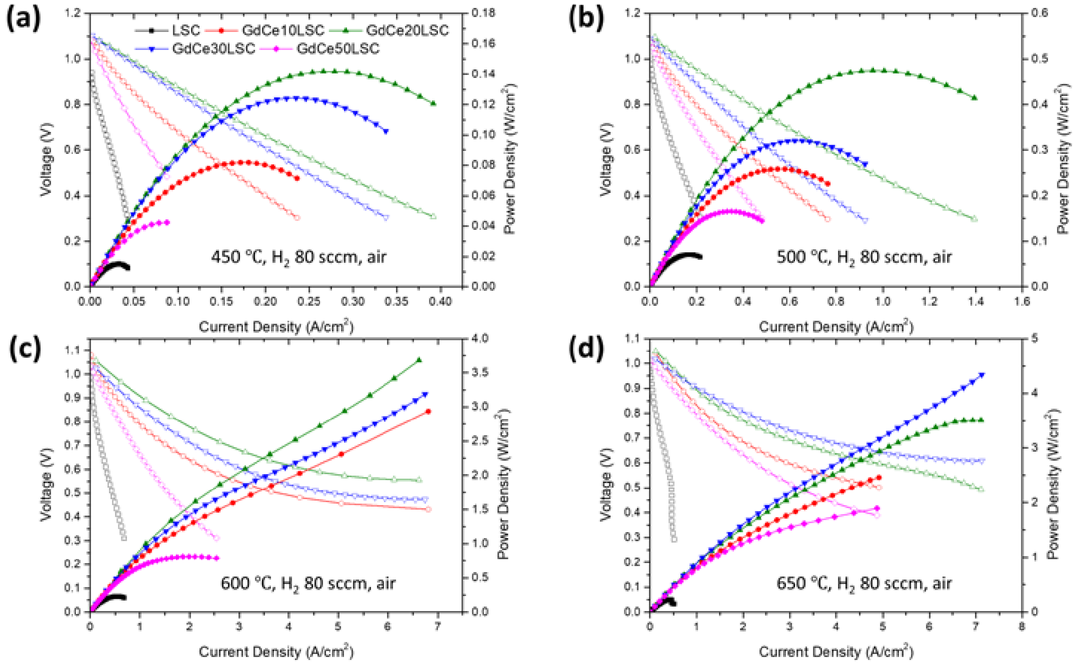

Figure 1.20. Voltage vs. current density (empty circle) and power density vs. current density (solid circles) measured at (a) 450°C, (b) 500°C, (c) 600°C, and (d) 650°C.

1.5.3 Power Densities and Fittings

It was observed that the PD at 600 and 650 °C increased with increasing current density without showing a peak at high current densities. This was most likely a result of the cell heating up due to the high current density. This only happens when current density rises above a certain threshold due to the limitation of heat dissipation in small cells. The peak PD at these temperatures was thus determined by fitting the power density data at lower current densities to a parabolic curve; the methodology is shown in Figure 1.21. Considering the system without an issue with heat dissipation, the $I-V$ curve follows a quasi-linear relationship (small discrepancy from linear relationship at OCV and high current density due to polarization resistance and gas transfer polarization resistance). This means the $I-P$ curve should follows $P = IV = I^2R$, where R is a constant resistance at certain temperature. According to the $I-P$ curves measured at lower temperature, when current density is lower than 4 A/cm^2, there is no significant heating effect occurred. Thus, by only applying the data from 0 to 4 A/cm^2 to fit a parabolic curve, we can

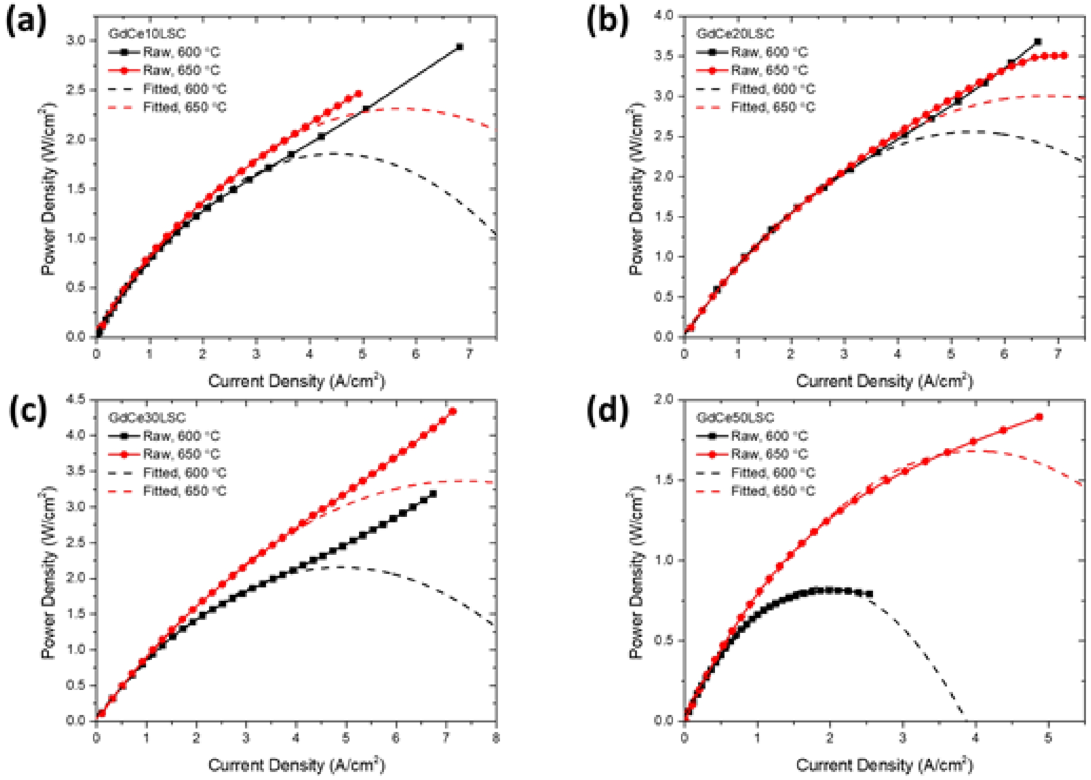

Figure 1.21. Peak power density vs current density (black square for 600°C, red circle for 650°C) and parabolic fitting curves (dash lines) for the (a) GdCe10LSC, (b) GdCe20LSC, (c) GdCe30LSC, and (d) GdCe50LSC samples. The data range for the fitting is from 0 to 4 A/cm^2.

determine the peak PD at 600°C and 650°C.

Table 1.2 summarizes the open-circuit voltages (OCVs) and peak PDs measured at different temperatures for the sputtered cells. All of the OCV values are close to the theoretical values. The OCV of a commercial cell mounted on the same test station was about 1.06 V, similar to our TF-SOFC cells, indicating insignificant gas cross-leakage and proper sealing for the measurement setup. Compared to the pure LSC cathode (dense), the co-sputtered, porous cathodes show significantly higher power densities at all of the measured temperatures. Among the samples, GdCe20LSC shows the best performance, with peak PDs of 0.14, 0.48, 1.19, 2.56, and 3.01 W/cm^2 obtained at 450, 500, 550, 600, and 650 °C, respectively, the highest PD values that have been observed for YSZ-based TFSOFCs.

Table 1.2. Summary of the OCV and Peak Power Density at Various Temperature for Cells with Different LSC-GDC Cathodes

	OCV (V)	peak PD (W/cm^2)				
Temperature	500 °C	450 °C	500 °C	550 °C	600 °C	650 °C
pure LSC	1.02	0.01	0.07	0.14	0.23	0.23
GdCe10LSC	1.10	0.08	0.26	0.83	1.86	2.31
GdCe20LSC	1.12	0.14	0.48	1.19	2.56	3.01
GdCe30LSC	1.10	0.12	0.32	0.81	2.16	3.37
GdCe50LSC	1.08	0.04	0.17	0.53	0.81	1.68

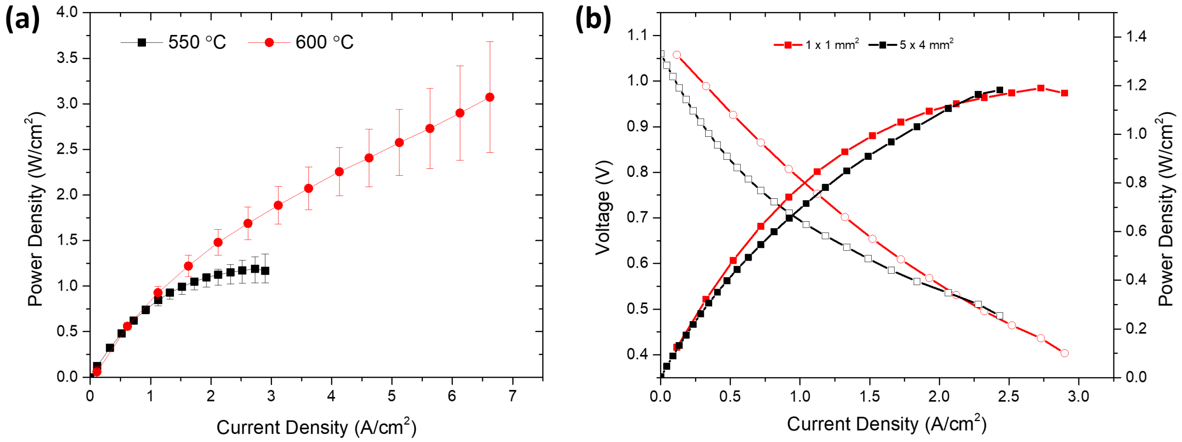

Figure 1.22. (a) Error bars from repeated transport measurements on GdCe20LSC TF-SOFCs at 550°C (black square) and 600°C (red circle) respectively. 5 different cells were measured at each temperature. (b) GdCe20LSC (5 × 4 mm^2 active area, black) IV and Peak PD curves compared to a 1 × 1 mm^2 active area cell (red).

1.5.4 Reproducibility, Durability and Scalability

To test reproducibility, multiple GdCe20LSC samples (5 in total) were tested at 550 and 600 °C and the error bars were obtained and shown in Figure 1.22a. It can be seen from Figure 1.22a that in spite of some performance variation commonly observed in SOFC cell testing, the experimental data show consistent performance. Notably, the peak PD for GdCe20LSC is slightly lower than that for GdCe30LSC at 650 °C and a comparison of different power densities of SOFCs measured at several different temperatures are shown in Figure 1.20. Overall, this comparison shows the superior power density for TF-SOFC with the nano-ceramic LSC-GDC cathode.

For durability testing, a co-sputtered cell was operated at 650 °C under a current density of 300 mA/cm^2. The test results are shown in Figure 1.19b, indicating that the cell was relatively stable over 20 h; it decayed less than 15%.

To verify the scalability of our fabrication method, cells with an active area of 5×4 mm^2 were fabricated. The peak PD and IV curves are shown in Figure 1.22b and compared to the same cell configuration that had a 1 mm^2 active area. There is no significant discrepancy between the small cell and the larger cell, which indicates the validity of our transport measurement and the scalability of the sputtering method.

1.5.5 Characterization of Cathodes and Impacts from Morphology and Composition

The cells were characterized using cross-sectional SEM images, and X-ray diffraction (XRD) patterns were obtained for each different cathode. The SEM images are shown in Figure 1.23a-d for pure LSC, GdCe10LSC, GdCe40LSC, and Pure GdCe. SEM images of the tested cell are also included in Figure 1.24. There is insignificant change of morphology before and after testing. From these images, there is a clear transition from a completely dense structure (pure LSC) to a porous structure once co-sputtering of LSC with Gd-Ce was conducted. Using a higher sputtering power of the Gd-Ce target (a higher GDC content in the layer) resulted in a composite with a higher porosity and increased ionic conductivity. In principle, with higher porosity and increased ionic conductivity in electrodes, the PD will be higher due to a larger active surface area and a lower cathodic polarization resistance. This trend was observed experimentally; however, once the Gd-Ce power exceeded 20 W, the PD decreased. This phenomenon indicates that the cathode composition, not just the morphology, also plays an important role.

To understand structural effects from the compositional changes of the co-sputtered cathode, the same cathodes previously mentioned were sputtered on Si/SiO$_2$ wafers and annealed at the typical operation temperature (600 °C) for 2 h before being measured by XRD. The resulting XRD patterns are shown in Figure 1.23e-h, and the peaks for LSC and GDC are labeled

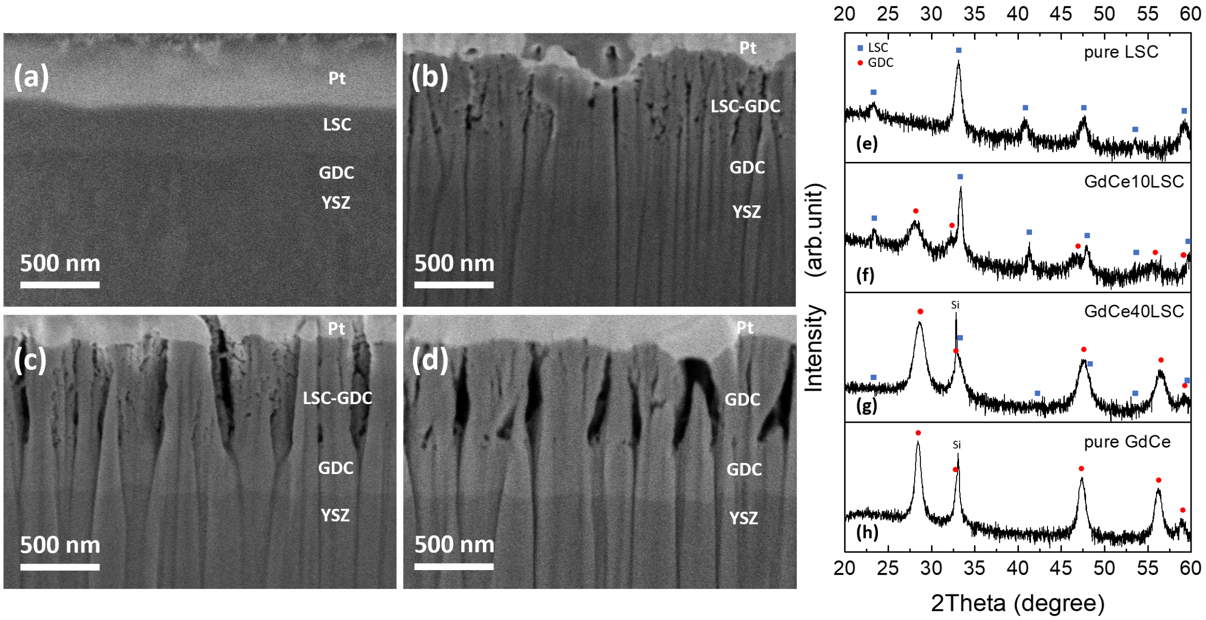

Figure 1.23. Cross-sectional SEM images and corresponding XRD patterns for (a and e) pure LSC cathode, (b and f) co-sputtered GdCe10LSC cathode, (c and g) co-sputtered GdCe40LSC cathode, and (d and h) pure GdCe cathode. Intensities are presented in log-scale.

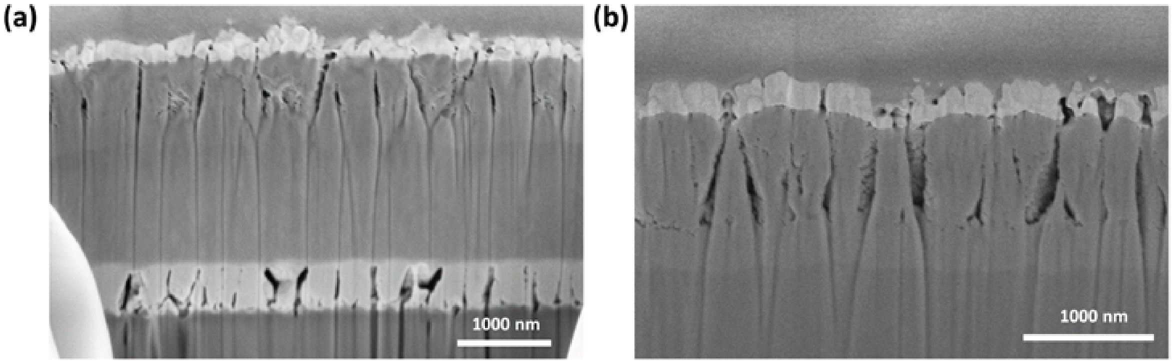

Figure 1.24. (a) SEM image of a tested cell. (b) Zoomed-in SEM image of the cathode after test.

with blue squares and red circles, respectively. The sharp peak at $2\theta = 33°$ corresponds to the Si(200) peak from the Si/SiO_2 substrate. The XRD pattern in Figure 1.23e corresponds to the sputtered pure dense LSC cathode as shown in the SEM image in Figure 1.23a; this XRD pattern only shows the peaks for LSC without any peaks from GDC, as expected. With co-sputtering of LSC with 10 W Gd-Ce, GDC peaks start to appear, while LSC peaks become less intense. As the sputtering power of GDC was gradually increased from 10 to 40 W, the GDC peaks become more prominent and the LSC peaks continue to decrease in intensity until virtually only the GDC peaks are seen (with pure Gd-Ce). Assuming the strain and stress in the thin films are negligible after annealing, by fitting the peak widths with the Scherrer equation,

$$\tau = \frac{K\lambda}{\beta cos\theta} \tag{1.18}$$

where τ is the crystallite size (coherence length), K is shape factor, λ is wavelength of Cu X-ray, β is the half the maximum intensity (FWHM), and θ is the Bragg angle. From XRD results in Figure 1.23, we obtain the τ for each phase, which is a measure of the size of the nanoparticles. The extracted crystallite sizes for LSC are 105.8 nm (pure LSC) and 165.9 nm (GdCe10LSC), and the crystallite sizes for GDC are 52.4 nm (GdCe10LSC), 80.8 nm (GdCe40LSC), and 169 nm (pure GdCe); both increase proportionally to the GDC ratio. In general, the larger the crystallite size is, the smaller the TPB will be. This change of composition and crystallite size in the cathodes decreases the TPB length, resulting in lowered power densities. The characterization results seem to reinforce that the nanostructure and composition of the cathode are the two main factors that impact the performance in our TF-SOFCs. The two competing mechanisms appear to be as follows: (1) a higher Gd-Ce ratio will dramatically enhance the porosity and ionic conductivity of the mixed conductivity in the cathode, but (2) a lower ratio of LSC will yield a shorter TPB length in the cathode and decrease catalytic activity. Among all of the fabricated cathodes, the peak performance was obtained when co-sputtering the Gd-Ce target at a power of 20 W. Compared to the sample after annealing (similar conditions as after testing), the as-deposited sample shows a similar XRD pattern but with less-intense LSC peaks. We believe this is due to grain growth of the LSC phase and thus an increase in the crystallinity of LSC during the annealing process.

1.5.6 Mechanism of Cathodes Studied via EIS and DFRT

Electrochemical impedance spectroscopy (EIS) was conducted during cell operation. To get quantitatively reliable data for cathode and anode separately, the distributed function of relaxation time (DFRT) method was conducted on the EIS data. DFRT characterization of EIS data is a convenient method to distinguish the different impedance contributions in TF-SOFCs.[30] DFRT transforms EIS data from the frequency domain to the time domain to distinguish contributions from different processes more clearly. In general, these processes are made up of a series of reaction steps: (i) adsorption of electroactive gaseous species (hydrogen or oxygen), (ii) dissociation of electroactive species on the electrode surface, (iii) diffusion of adsorbed species on the electrode surface to TPB sites, (iv) diffusion of oxygen ions to/from TPBs, and (v) charge transfer reactions. To investigate the high performance in our sputtered cathodes, galvanostatic EIS and DFRT were conducted for pure LSC cathode and co-sputtered GdCe10LSC cathode at 550 °C and the data are shown in Figure 1.25a,b. The AC frequency range was from 1 MHz to 0.1 Hz, and the impedance was measured at OCV. The DRT tool software was used to transform EIS data into the time domain for analysis,[42, 43] and a Gaussian distribution was used in the fitting. As shown in the EIS data in Figure 1.25a, the Ohmic resistances in two samples are close to each other, indicating the YSZ electrolyte and GDC interlayer are properly deposited. The small difference in each sample might be from variations in the Ohmic resistance of the electrolyte. From the DFRT data in Figure 1.25b, 5 main peaks were observed, located at 1 MHz (P_e), 14.0-11.8 kHz (P_i), 3.2-2.2 kHz (P_{a1}), 137-136 Hz (P_{a2}), and 18.3-0.187 Hz (P_{c1} + P_{c2} = P_c). Here P_{c1} and P_{c2} can be treated as a combined P_c since the gas diffusion, adsorption, and charge transfer reaction are coupled (and difficult to deconvolute) in MIEC cathodes.

The polarization resistances for each peak vary for each sample. To separate the polariza-

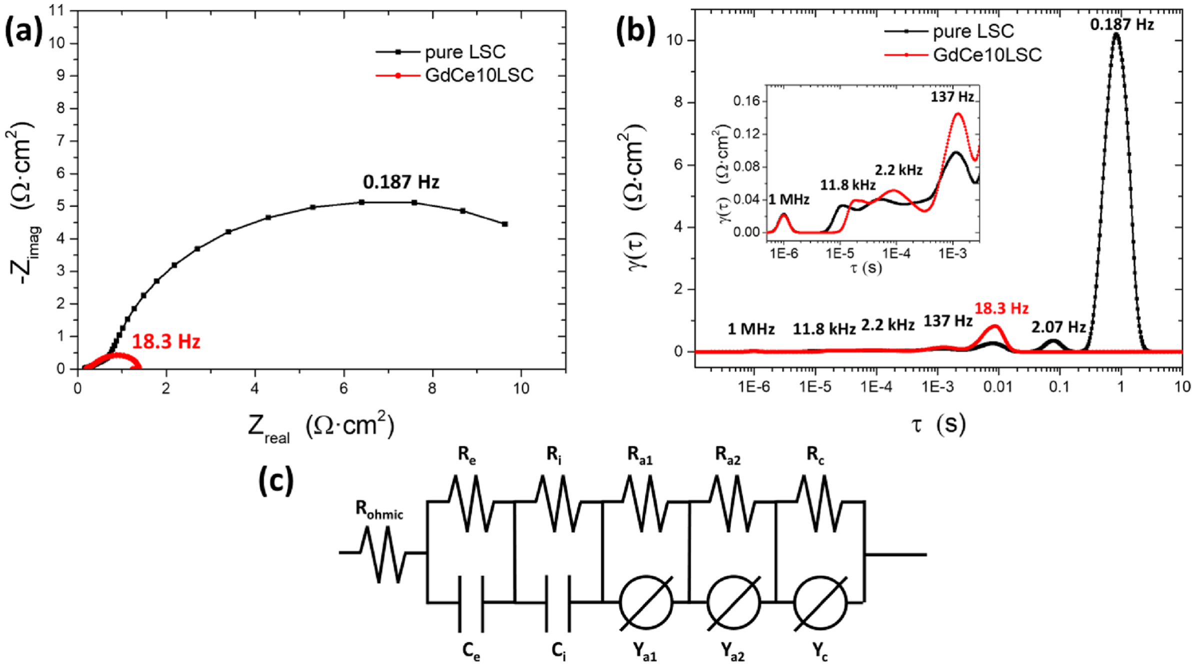

Figure 1.25. (a) EIS for pure LSC (black), co-sputtered GdCe10LSC cathode (red) and (b) the corresponding data transformed into DFRT curves. (c) Equivalent circuit used for the EIS fitting.

tion loss from the anode and cathode, different temperatures and hydrogen partial pressures were applied by mixing helium gas to the anode. The DFRT figures for different hydrogen partial pressures and temperature measured for pure LSC cathode are plotted in Figure 1.26a,b. From the DFRT figures, the two peaks around 3.2-2.2 kHz (P_{a1}) and 137-136 Hz (P_{a2}) come from the anode (since it changes with the hydrogen partial pressure) while the other three peaks are independent of the hydrogen partial pressure. These two peaks can be described by a constant phase element (CPE) in parallel with resistor (R), denoted as CPE//R. The two peaks above 1 MHz (P_e) and around 14.0-11.8 kHz (P_i) only change with temperature, and their frequencies increase with increasing temperature as shown in Figure 1.26c,d, so we assume that these come from the ionic transport process in the bulk electrolytes and the interface polarization resistance between electrolyte and anode; these two contributions are defined using a resistor in parallel with pure capacitance (C) denoted as R//C. The peaks at the lowest frequency from 18.3 to 0.187 Hz (P_c) are independent of the hydrogen partial pressure but dramatically change with the different cathodes. This can come from the surface exchange process and ionic and charge transport processes in the cathode. This peak could not be simply described by a R//C component as shown in Figure 1.25a, since the cathode is a typical MIEC which therefore does not behave like a pure double layer capacitor due to the bulk oxygen diffusion.[44, 45] Here we use the CPE//R component to represent this composite cathode.[46] The equivalent circuits are shown in Figure 1.25c, and the fitting parameters and results are listed in Tables 1.3 and Tables 1.4. The equivalent capacitance C values for all CPE//R components are effective capacitances calculated from the fitting parameters Q and n of the CPE component through the equation $C = (R^{1-n}Q)^{1/n}$, where R is the resistance of the parallel resistor, Q is the value of the admittance, and n is a constant. It is clearly seen that P_e, P_i, P_{a1}, and P_{a2} in different cells are close to each other since these have an identical anode and electrolyte. The only difference in the EIS fitting data comes from the cathode Pc, intuitive since that was the component that was varied. The fitted cathodic polarization resistance R_c for pure LSC and cosputtered GdCe10LSC cathode are 11.15 and 0.56 $\Omega \cdot \mathrm{cm}^2$, respectively. The two-order decrease of cathodic polarization resistance for the co-sputtered composite cathode results from the increased porosity and better ionic conductivity in the composite cathode, which in turn was caused by the superior porous nanostructure and with the introduction of GDC in the cathode. Table 1.5 summarizes the various reaction steps assigned from the DFRT data analysis.

1.5.7 Summery of GDC-LSC Cathode

In summary, nano-ceramic cathodes for TF-SOFCs were fabricated by co-sputtering a Gd-Ce alloy with LSC. Cells containing these composite cathodes showed superior power density at low temperatures, from 0.14 W/cm^2 at 450 °C to 3.01 W/cm^2 at 650 °C. Characterizations by TEM, SEM, XRD, and electrochemical measurements show that the composition and nanostructure of the cathode are the two main factors that impact the power density of the TF-SOFCs. By comparing the EIS data of the deposited pure LSC cathode with co-sputtered composite cathodes, it can be seen the cathodic polarization resistance of the composite cathode

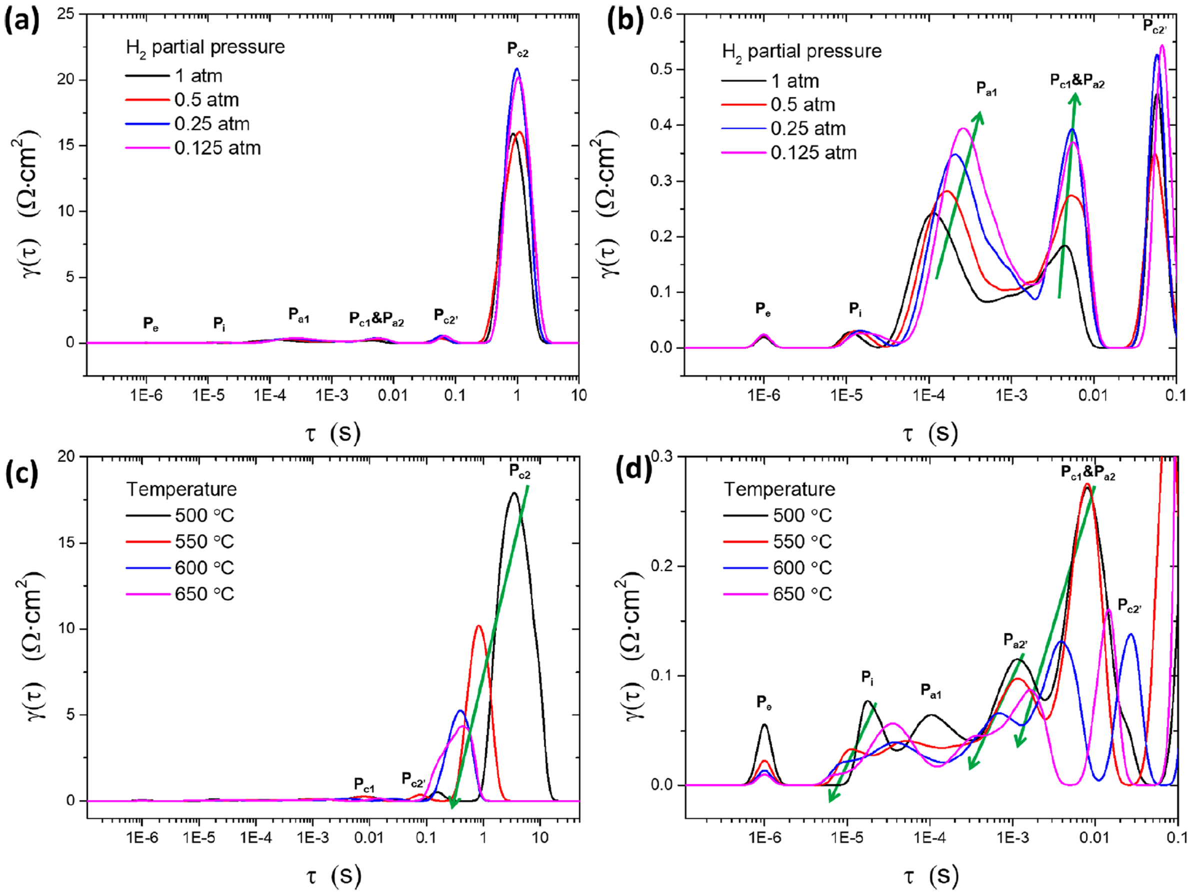

Figure 1.26. DFRT analysis for the pure LSC cathode: (a) overall and (b) zoomed-in view of the DFRT influenced by different hydrogen partial pressures and (c) overall and (d) zoomed-in view of DFRT influenced by different temperatures.

Table 1.3. EIS fitting parameters by using the equivalent circuits deduced by DFRT analysis.

Parameters	Pure LSC	GdCe10LSC	Units
Rohmic	2.366	4.671	Ω
R_e	13.7	14.33	Ω
C_e	8.15E-10	1.25E-09	F
R_i	1.388	2.991	Ω
C_i	1.07E-05	1.05E-05	F
R_{a1}	11.48	12.17	Ω
Q_{a1}	1.68E-04	2.23E-04	$S\times s^n$
n_{a1}	0.657	0.66	-
R_{a2}	54.31	48.59	Ω
Q_{a2}	5.80E-04	2.28E-04	$S\times s^n$
n_{a2}	0.666	0.781	-
R_c	1115	56.37	Ω
Q_c	7.27E-04	1.69E-04	$S\times s^n$
n_c	0.949	0.983	-
Goodness of Fit	6.97E-05	5.35E-05	

Table 1.4. EIS fitting results and calculated effective capacitance and frequency for each fitted component.

Fitted Results	Pure LSC	GdCe10LSC	Units
R_{ohmic}	2.366	4.671	Ω
R_e	13.7	14.33	Ω
C_e	8.15E-10	1.25E-09	F
f_e	1.43E+07	8.89E+06	Hz
R_i	1.388	2.991	Ω
C_i	1.07E-05	1.05E-05	F
f_i	1.07E+04	5.07E+03	Hz
R_{a1}	11.5	12.17	Ω
C_{a1}	6.38E-06	1.07E-05	F
f_{a1}	2.17E+03	1.22E+03	Hz
R_{a2}	54.3	48.59	Ω
C_{a2}	1.03E-04	6.44E-05	F
f_{a2}	2.85E+01	5.09E+01	Hz
R_c	1115	56.37	Ω
C_c	7.19E-04	1.56E-04	F
f_c	0.198	1.81	Hz

Table 1.5. Assigned Reaction Steps for the DFRT Data Analysis

DFRT peak	Frequency	Reaction step assigned
P_e	above 1 MHz	Diffusion of oxygen ions in the electrolyte to TPB
P_i	14.0-11.8 kHz	Transfer of oxygen ions from the bulk electrolyte to TPB sites
P_{a1}	3.2-2.2 kHz	Hydrogen adsorption, dissociation, and diffusion of adsorbed hydrogen atoms to anode TPB sites
P_{a2}	137-136 Hz	Charge transfer reaction between oxygen ions and adsorbed hydrogen atoms at TPB sites
P_c	18.3-0.187 Hz	Oxygen adsorption, dissociation, diffusion of adsorbed oxygen atoms to cathode TPB sites and charge transfer reaction of adsorbed oxygen atoms

dramatically decreased due to the superior nanostructure and optimized ratio of LSC to Gd-Ce. The peak power densities observed for sputtered thin-film cells are the highest among YSZ-based TF-SOFCs in the temperature range of 450-650 °C. This method of fabricating nanostructured ceramic composite cathodes by co-sputtering has been successfully demonstrated with Gd-Ce and LSC. The reproducibility and scalability of the magnetron sputtering platform have been illustrated in this letter and can thus be further adapted, namely, in using a variety of other materials, or for increasing the active area, to make TF-SOFCs for practical applications.

1.6 Ethanol and Methane Fuels Modes

It is important to make the TF-SOFCs fuel flexible due to the limitations of pure hydrogen fuel. Hydrocarbons like methane and ethanol are easy to produce, store and deliver. Even though the hydrocarbon fuels may emit carbon dioxides during the operation, it is still considered as a clean energy due to the high efficiency of SOFCs and easy management of gas wastes. In this section, we will give some brief results of using hydrocarbons as fuels in our fabricated TF-SOFCs.

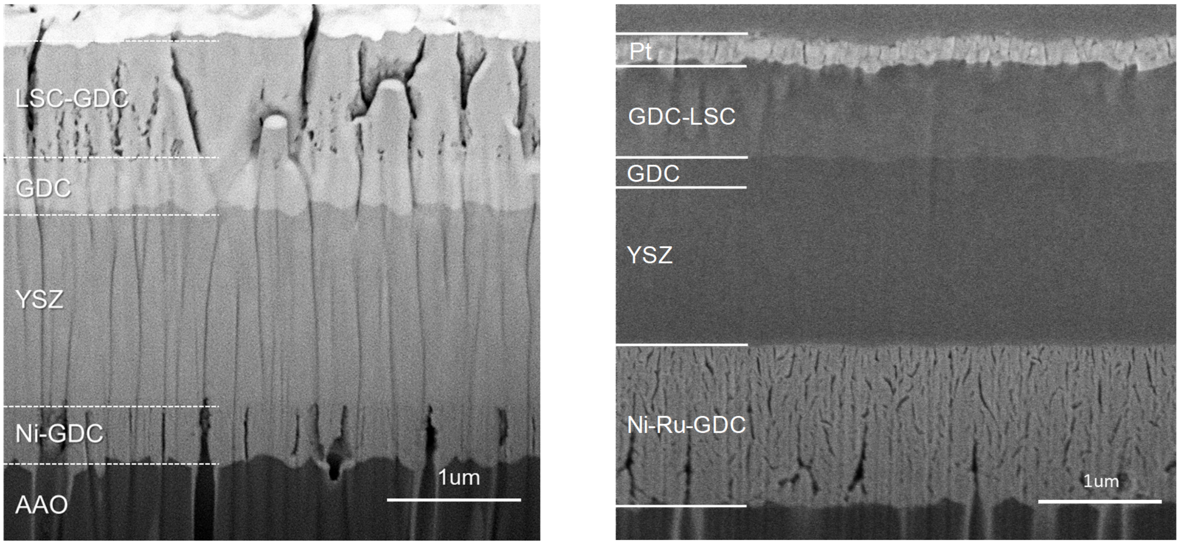

Figure 1.27. (a) Ni-GDC anode for methane fuel operation and (b) Ni-Ru-GDC for ethanol fuel operation

1.6.1 Anodes Deposition for Hydrocarbon Fuels

For the porous anode layer operating in hydrocarbon fuels, two different composite anodes are deposited. For ethanol gas fuel, co-sputtering of 3-inch Ru metal, 2-inch Ni and 2-inch GDC ceramic targets were conducted in pure Ar at 30 mTorr for 1 hour by two DC power sources at 100 W, 200 W and by RF power souce at 200 W, respectively. The film thickness is about 1 µm to ensure enough reforming time. For methane gas fuel, co-sputtering of 3-inch Ni metal with 2-inch GDC ceramic targets were conducted in pure Ar at 30 mTorr for 1 hour by 200 W DC power source and 150 W RF power source repectively. The film thickness is about 1 µm. Both of them are deposited on top of aluminum oxide template. Electrolytes and cathodes are deposited using the same technique and conditions as we mentioned in previous sections. The SEM images for the fabricated cells are shown in Figure 1.27.

1.6.2 Performance under Methane and Ethanol Fuels

The performance of the fabricated TF-SOFCs operating under hydrocarbon fuels are shown in Figure 1.28. The peak power density for the Ni-GDC anode sample and Ni-Ru-GDC

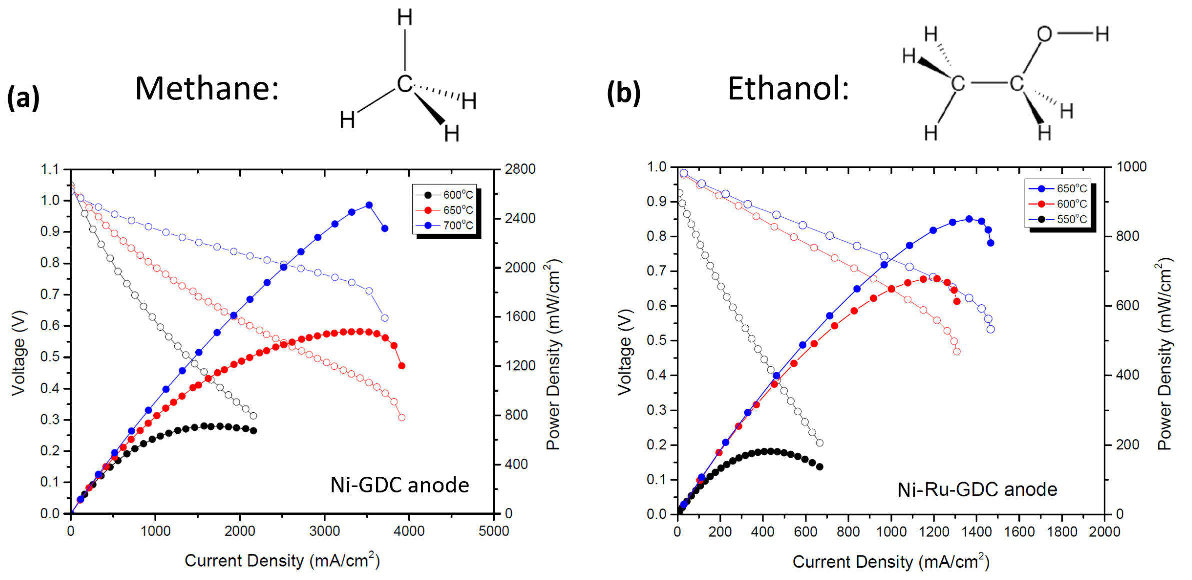

Figure 1.28. (a) Performance of TF-SOFCs using Ni-GDC as anode under methane fuel and (b) Ni-Ru-GDC as anode under ethanol fuel at 600 °C

sample reach 0.65 W/cm^2 and 0.7 W/cm^2 at 600 °C, respectively, which is much higher than the conventional SOFCs at this temperature. No significant carbon deposition could detect after the operation. This proves the validation of using TF-SOFCs as a platform for hydrocarbon fuel operations at relatively lower temperature.

1.7 Conclusion

In this chapter, we have presented the development of nano-porous YSZ-LSCF and GDC-LSC cathodes, Ni-Ru-GDC and Ni-GDC anodes via magnetron sputtering technique, and the fabrication of the full TF-SOFCs based on AAO substrates. Compared to conventional SOFCs, all these TF-SOFCs are showing promising performances at low operation temperatures (450-650 °C), respectively. Electochemical measurements and characterizations examined the growth mechanism for our porous electrodes and the mechanism for the superior performance. The future works will be focus on the scale-up and stability of fabricated TF-SOFCs.

1.8 Acknowledgement

Chapter 1, in part, is a reprint of the material “Lee, Y. H.*; Ren, H.* Wu, E.* A.; Fullerton, E. E.; Meng, Y. S.; Minh, N. Q. “*All-Sputtered, Superior Power Density Thin-Film Solid Oxide Fuel Cells with a Novel Nanofibrous Ceramic Cathode*”. Nano Lett. 20, 5, 2943–2949, (2020).”, ”H. Ren, Y. H. Lee, E. Wu, H. Chung, Y. S. Meng, E. E. Fullerton, N. Q. Minh, *Nano-Ceramic Cathodes via Co-sputtering of Gd-Ce Alloy and Lanthanum Strontium Cobaltite for Low-Temperature Thin-Film Solid Oxide Fuel Cells*, ACS Applied Energy Materials, 3, 9, 8135–8142 (2020).”, and N. Q. Minh, Y. H. Lee, T. Q. Tran, H. Ren, E. E. Fullerton, E. A. Wu, Y. S. Meng, *“Development of a versatile, high-performance solid oxide fuel cell stack technology”*, ECS Trans., 91(1) 133-138 (2019). The dissertation author was the primary investigator and author of these materials.

Chapter 2

Temperature-dependent Magnetoresistance and Domain Wall Resistance in Single Crystalline Si-doped Ni Nanowires

Temperature-dependent magneto-transport measurements were conducted on single-crystalline, Si-doped Ni nanowires formed by chemical vapor deposition. The data show a dramatic decrease in Curie temperature due to Si doping arising in the synthesis process. The magnetoresistance behavior below is explained by the competition between cubic magneto-crystalline anisotropy and shape anisotropy showing a reduced magnitude of M_s and K_1. We further see evidence of significant negative domain wall magnetoresistance at low temperatures, consistent with micromagnetic simulations. The observed quasi-linear dependence of resistivity at high applied fields is explained by the combined effect of electron-magnon scattering and ordinary magnetoresistance. Fitting the data combining these two factors leads to an extracted exchange stiffness $d_1 = 2.1\times10^{-6}$ K^{-2}.

2.1 Introduction

As technology continuously advances, devices are scaling down to only few nanometers, which requires future generation of materials producible and functional at this scale. Among developing materials system, nanowires is one the potential materials that can bring a new opportunities for innovation. There are ways to fabricate nanowires from thin films where the wires are definded by nanolithography or electrodeposition into nanopore arrays (e.g. AAO). However, the degree of freedom of fabrication is limited in all methods and there needs a new technique to fabricate nanowires with simple and straightforward procedures. In the data storage and memory industries, transition metals like Fe, Co, and Ni are commonly used as the base of materials due to their spontaneous magnetization property. It will be beneficial to explorre new method of fabricating these materials into nanowires, which will greatly promote the development of storage and memory technologies.

Magnetoresistance (MR) effects are fundamental for the functionality of spintronic devices and further probe underlying magnetic phenomena in materials. In ferromagnetic metals the sources of MR include anisotropic magnetoresistance (AMR)[47] and domain wall magnetoresistance (DWMR)[48, 49, 50, 51] which occur for low field below the saturation field of the materials. At high applied magnetic fields, AMR and DWMR effects are diminished when the magnetization is saturated, while the majority contributions to the MR come from the ordinary magnetoresistance (OMR) and electron-magnon scattering magnetoresistance[52]. OMR is typically more prevalent at lower temperature, low resistivity materials and become much smaller at relative higher temperatures. Meanwhile, electron-magnon scattering in 3d ferromagnetic metals like Ni, Co and Fe are prevalent and dominant above at higher temperatures. Raquet et al.[52] proposed a model that assumes at high fields, the change of resistivity is majorly caused by spin-flip process between s-d interband and intraband scattering. Within this model only magnons above certain wave vectors can induce spin-flip processes and increase the resistivity at high field. This method has been applied to study the electron-magnon scattering in various ferromagnetic materials such as polycrystalline cobalt[53], FePt thin film[54] and NiFe nanowires[50], etc.

Electrical transport measurements are conducted on single-crystalline, Si-doped Ni nanowires which are fabricated by a thermal chemical vapor deposition (CVD) method. Below the saturation field, the AMR response reflects the competition between magneto-crystalline and shape anisotropies. At low temperatures we further observe a negative DWMR, which gives distinct MR curves that cannot be understood from AMR responses alone. For high magnetic fields we quantify the electron-magnon scattering magnetoresistance and OMR.

2.1.1 Mechanism of CVD Fabricated Single Crystalline Ni Nanostructures

In materials science, CVD is a flexible technique that can apply to various of applications. In our experiments, a thermal CVD system with controlled atmosphere and temperature is set up for the deposition of Ni nanowires. The heart of growth mechanism of Ni nanowires in CVD is the driving force, which is depending on the nature of the materials deposited, growth surfaces and adsorption and desorption. A typically CVD process involves a few key mechanisms, such as thermodynamics, fluid dynamics, kinetics and other so on. Thermodynamically, to make a growth process take place, the change of Gibbs free energy from reactant side to product side must have a net value smaller than zero. In our case, the difference of the chemical potential between the crystal and the medium should be smaller than zero. Considering the vapor state of medium, we should have the equation for the change of chemical potential as:

$$\Delta\mu = k_b T log(\frac{C_{vapor}}{C_{equilibrium}}) \tag{2.1}$$

where k_b is the Boltzmann constant, T is the temperature, $C_{vapor}, C_{equilibrium}$ are the concentration of vapor particles and the concentration of equilibrium state in solid crystal, respectively. The rate of chemical reaction is determined by the organization/situation of adatoms at the interface between crystal and vapor. Under adequately high driving force, a kinetic roughening transition takes place and leading to an adhesive type growth. This can be also observed in high temperature growth. Giving enough time and energy to the atoms, the adsorbed atoms on surface start to migrate and desorption occurred. As a result, the average diffusion length of the adatoms is given by:

$$\lambda_{surface} = Aexp(\frac{E_{desorption} - E_{surface}}{2k_b T}) \tag{2.2}$$

where $\lambda_{surface}$ is the diffusion length, $E_{desorption} - E_{surface}$ is the energy difference of adatoms between desorption and surface. This indicates that the frequency of island nucleation on the surface is critical for the growth of single crystals. During the adsorption and desorption processes, atoms are continuously deposited on the surface. The binding energy and partial pressure of materials determine the rate of growth.

To better understand the growth Ni nanowires, the mechanisms need to be discussed first. The vapor-liquid-solid mechanism (VLS) is the key theory to achieve this anisotropic growth of Ni nanostructure.[55] The heart of this mechanism is to make the materials have phase transitions in the order of vapor to liquid and then to solid. Before the vapor phase reactant deposited, the catalyst will already melted into small droplets on the substrate. This will lead to an accommodation of materials near the catalyst droplets and introduce a supersaturation point when solid phase start to form. The self-catalytic oxide-assisted growth of Si nanowires is a good example to illustrate this mechaism.[56] The chemistry of Ni nanowires is achieved by using Halide-cycle reaction, which uses a $NiCl_2$ as precursor to deposit Ni films on substrate via CVD. The initial step of chemical reactions is:

$$\mathrm{NiCl_2(g) + H_2O(g) \longrightarrow NiO(s) + 2\,HCl(g)} \tag{2.3}$$

where $NiCl_2(g)$ was evaporated from the solid phase in precursor. After that, NiO start to reduced to some metallic Ni phase and deposit on the surface of substrate:

$$\mathrm{H_2(g) + NiO(s) \longrightarrow H_2O(g) + Ni(s)} \tag{2.4}$$

Upon this freshly deposited Ni surface, more Ni atoms preferably attache to Ni surface and forming Ni-Ni metallic bonds. Simultaneously, NiO will react with HCl as followed:

$$\mathrm{H_2(g) + NiCl_2(g) \longrightarrow Ni(s) + 2\,HCl(g)} \tag{2.5}$$

$$NiO(s) + 2\,HCl(g) \longrightarrow NiCl_2(g) + H_2O(g) \tag{2.6}$$

This will allow to resupply the ambient with $NiCl_2$ and moisture. Repetitively, these chemical reactions occurred in cycles and continuously deposit Ni materials on substrates.

2.1.2 Anisotropic Magnetoresistance

The anisotropic magnetoresistance is commonly observed magnetic materials. The term is used to describe the change of resistance of magnetic materials upon the change of the angle between current direction and field direction as shown in Figure 2.1a. The effect is mainly caused by the simultaneous action of magnetizaiton and spin-orbit interaction. The scattering of s-d orbits of electrons contribute to the change of resistance at different angles, where the maximum resistance can be observed when the direction of current is parallel to the applied magnetic field and minimum resistance at when they are perpendicular to each other as shown in Figure 2.1a. In the perpendicular case, electrons has minimum interaction with crystals and shown smallest resistance. By assuming the smallest resistivity appeared at perpendicular field ($\rho_{\perp}$) and maximum resistivity at parallel field(ρ), we can have a simple expression for AMR ($\rho(\beta)$):

$$\rho(\beta) = \rho_{\perp} + (\rho_{||} - \rho_{\perp})cos^2\beta \tag{2.7}$$

By sweeping magnetic field and fixing the external magnetic field angle, one can obtain another form of AMR as shown in Figure 2.1b. In this case, useful information like saturation field, coercive field and switching field can be extracted and used to calculate the magnetic properties of measured materials.

2.1.3 Magnon and Electron-magnon Scattering Magnetoresistance

In quantum mechanics, waves can be described as particles under certain conditions. Similar to photons, magnons are waves that can be expressed as particles and they carry the

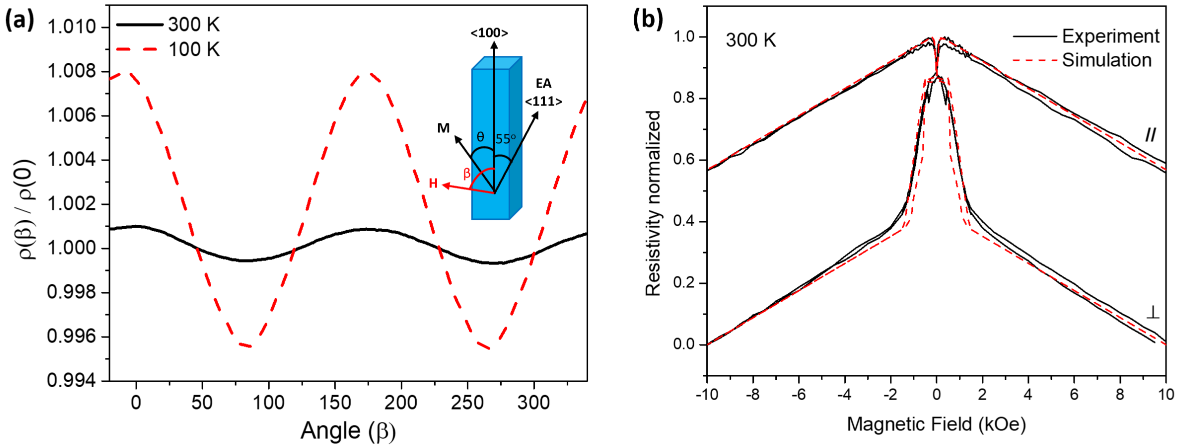

Figure 2.1. (a) AMR curves versus the angle between current direction (along the NW axis) and the external magnetic field (10 kOe). (b) Experimental AMR curve (black solid) measured at 300 K and simulated AMR curve (red dash).

energy:

$$E = hf \tag{2.8}$$

where h is the Plank constant and f is the precession frequency. Magnons can be visualized as a complete precession distributed over a chain of electrons' spins. The velocity of magnons depend on the angle between propagation direction and the external magnetic field direction, and also depend on precession frequencies of the spins in the chain.

In ferromagnets like Fe, Co, and Ni, spontaneous magnetization nature of these materials will lead to the formation of the aligned spins along one direction without the help of external magnetic field. In this situation, electron spins are more likely to communicate with each others and form a spin chain. Inelastic neutron scattering in these magnetic materials proves the band ferromagnetism theory that at low temperature, the spin-wave stiffness shows a T^2 relation to the temperature and the existence of an optic branch for magnon proves these materials are 3d magnetism.[57] Based on these theory, Raquet[52] proposed a method to estimate the spin-wave stiffness by simply conducting transport measurements on materials at high magnetic field. A straightforward relationship between temperature, magnetic flux and stiffness can be found in this theory:

$$\Delta\rho(T,B) \approx \rho(T,B) - \rho(T,0) \propto \frac{BT}{D(T)^2} ln(\frac{\mu_B B}{kT}) \tag{2.9}$$

where $D(T)$ is the temperature dependent spin-wave stiffness. By fitting the $\Delta\rho(T,B)$ at different temperature, one can obtain the $D(T)$ of this measured material.

2.1.4 Micromagnetic Simulation

Micromagnetic simulation has been widely used as a powerful tool in predicting and verifying magnetic properties and behaviors of materials. The micromagnetic simulator employ a finite difference discretization of space with various of shape of cells. Magnetic properties like magnetization and effective field are placed at the center of each cell, while coupling and interactions between cells are treated on the interface between the cells. One of the important function that micromagnetic simulator can achieve is to find the static equilibrium state of the system via minimizing the magnetic energy E_{total}. This total energy is a sum of a couple of distinctive energy terms, such as exchange energy, anisotropic energy, Zeeman energy, demagnetization energy, and magnetoelastic energy, etc., which could write as

$$E_{total} = E_{exch} + E_{anis} + E_{Zeem} + E_{demag} + E_{m-e} \tag{2.10}$$

By finding the minimum energy of the system, one can quickly obtain the stable magnetic states that a magnetic object should have at specific environment without considering the dynamic part of the equation. However, once the time scale of each step of simulation is comparable to the time scale of studied magnetic dynamic process, minimization of energy becomes not a valid approach to solve the magnetic states. At this time scale, the Larmor precessing of the magnetization and damping process start to play an important role. To solve the magnetic states at this time scale, we need to introduce the Landau-Lifshitz torque equation (in Gilbert form) as

$$\frac{\partial m}{\partial t} = -|\gamma| m \times H_{eff} + \alpha m \times \frac{\partial m}{\partial t} \tag{2.11}$$

where γ is the gyromagnetic ratio and α is the Gilbert damping constant. Through this approach, one can obtain the magnetic state at any time step and environment.

2.2 Experimental Methods

2.2.1 Thermal Chemical Vapor Deposition

The Ni nanostructures are fabricated by the thermal CVD system and the system setup is shown in Figure 2.2. As we discussed in the introduction, the driving force and the chemistry of reactant can give different growth morphology and crytallinity of Ni nanostructure. In our case, $NiCl_2 \cdot 6\,H_2O$ precursor is used as reactant, which will also release moisture during the vaporization process. As shown in Figure 2.3, high concentration of moisture can be achieved by directly heating the precursor at high temperature without preheat process. This will lead to a in-plane and horizontal growth of polycrystalline Ni nanowires. On the other hand, low moisture concentration can be achieved by preheating the precursor at low temperature before the deposition and leads to vertical growth of single crystalline Si-doped Ni nanowires. This growth behavior in accordance with the study observed before.[58] It is more interesting to grow single crystalline Si-doped Ni nanowires due to rarity of technique that is capable of growing these single crystalline nanowires. Before the depostion, the glass tube chamber is purged with pure Ar gas to eliminate oxygen and moisture from the air. To vertically growth the single crysalline Ni nanowires, the $NiCl_2 \cdot 6\,H_2O$ precursor is preheated at 200 °C for 30 minutes to eliminate extra moisture and maintain in dry state. During the preheat and deposition process, a 20 sccm of Ar gas is continuously delivered to the glass tube chamber in the purpose of creating a reduced environment and carrying the vaporized materials from the precursor to the surface of substrates. After the moisture of precursor becomes low enough, the temperature of the chamber is increased to 600 °C and maintained at this temperature for another 1 hour to deposit Ni on the substrate. According to previous study[58], the growth of the Ni nanowires is catalyzed by the Si atoms from the Si/SiO_2 substrate. This will lead to a final product of Si-doped Ni nanowire,

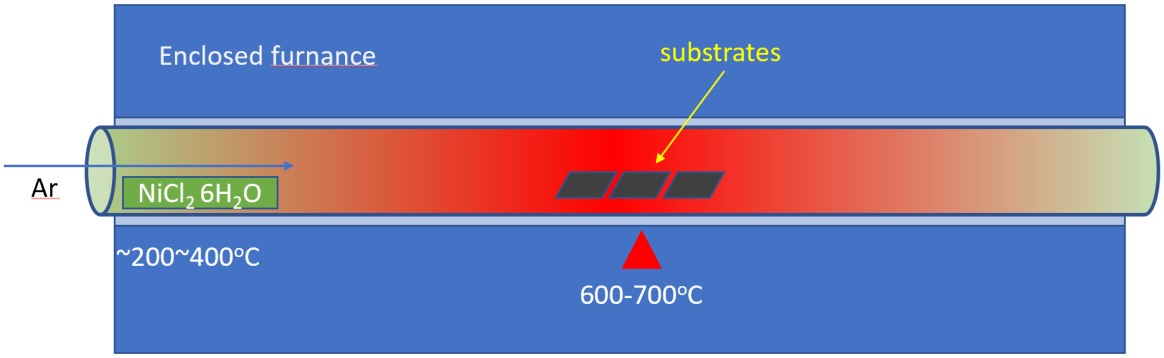

Figure 2.2. Thermal CVD system setup for Ni nanowires growth

which we will discuss in the coming sections in detail.

2.2.2 Nanowires Transfer and Contacts Patterning

The fabricated vertical Ni nanowires are grown on a Si/SiO_2 substrate. Due to the vertical growth of nanowires, the as grown nanowires are attached to the substrate by a weak connection at the interface, which is much smaller than the Van der Waals force when laying down on the surface of the substrate. Using this mechanism, once can simply overlay another substrate on top of the as grown sample to transfer the nanowires onto the substrates for future patterning.

Once the nanowires are transferred to a new substrate, we pattern contacts on top of nanowires for transport measurements. Four electrodes are patterned on top of the Ni nanowire to conduct 4-wires transport measurement, which is able to reduce the contact resistances and noise from the environment. To achieve this pattern, a negative photoresist NR7-1500 is exposed under a photomask in Mask Aligner 6 in the cleanroom. After develop of the photoresist, a 100 nm Ti/Au layer is deposited and lift-off in the acetone. The ultrasonic should be avoided due to weak binding force between the nanowire and substrate. The resulting patterned Ni nanowire is shown in Figure 2.4.

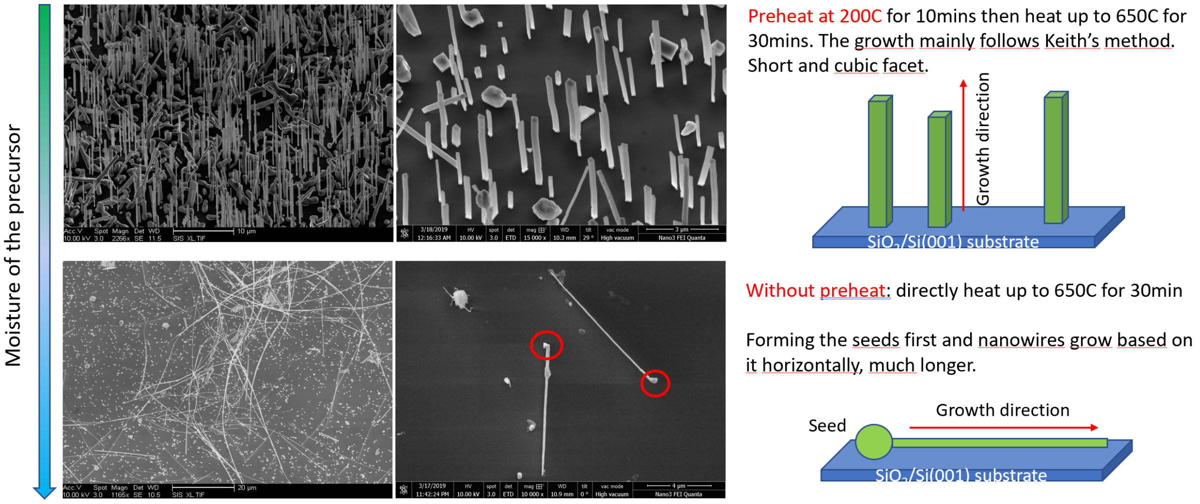

Figure 2.3. The two growth mechanisms controlled by the moisture of the precursor: lower moisture precursor gives vertical growth single crystalline Si-doped Ni nanowire and higher moisture precursor give horizontal growth of polycrystalline Ni nanowires

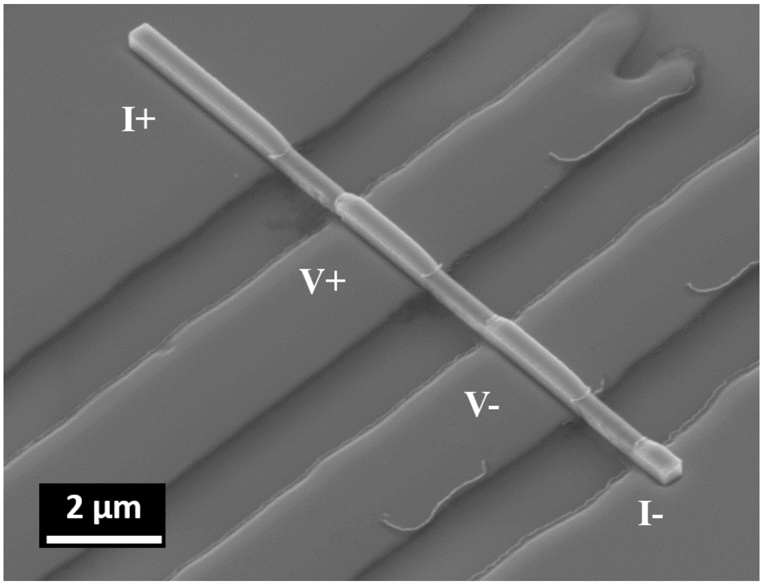

Figure 2.4. Patterned Ni nanowires after lift-off process and transport measurements configuration.

2.2.3 Transport Measurements Platform

Transport measurement are conducted in a Quantum Design Physical Properties Measurement System (PPMS) which allows apply a magnetic field up to 9 T via the superconducting coil and also a wide range of adjustable temperature from 2 K to 400 K. A horizontal rotator probe is used to allow an adjustable angle between the magnetic field and the easy axis of Ni nanowire. As shown in Figure 2.4, 4-wires transport measurements are conducted by patterning contacts on top of Ni nanowires and wire-bonding to the PCB on the horizontal rotator probe. The standard Resistivity Option is used for the low noise measurements of resistivity of the Ni nanowires. During the measurements, a 0.1 mA-AC current is provided to the current leads and voltage signals are detected from two voltage leads. The resistivity of the Ni nanowires can be calculated by divided the resistance by the cross sectional area of the measured Ni nanowire and multiplied by the length of the gap between two voltage leads.

2.2.4 MuMax3 Micromagnetic Simulation

The MuMax3 micromagnetic simulator is an open-source and GPU-accelerated micromagnetic simulation program written in Go and CUDA language. It can be used to calculate the space- and time-dependent magnetization dynamics in nano- to micro-sized ferromagnets using a finite-difference discretization. In our simulation, the Ni nanowire are divided into a $16 \times 16 \times 512$ grid with orthogonal shape in each cell. The energy minimization operation is conducted for the anisotropic constant and saturation magnetization calculations without considering the dynamic term in the system.[59]

2.3 Results and Discussion

2.3.1 Si-doped Single Crystalline Ni Nanowire Synthesis and XRD Characterization

Single-crystalline, Si-doped Ni nanowires were grown on Si(001)/SiO_2 substrate via a thermal CVD method using $NiCl_2 \cdot 6H_2O$ as the source material as described by previous studies.[58, 55] For the conditions used the growth direction of the single-crystal nanowires is normal to the amorphous SiO_2 substrate with a preferred [200] crystallographic direction along the Ni long-axis as shown in Figure 2.5(a). The cubic facet cross section of the nanowires indicated a high crystallinity quality and previous studies have shown the wires grown using this approach are single crystals. The dimensions of the nanowire samples studied range from $0.2 \times 0.2 \times 12\ \mu m^3$ to $0.4 \times 0.4 \times 12\ \mu m^3$. As proposed in an earlier study[55], the growth mechanism for these Ni nanowires is Si-assisted growth, where Si mediates the transition of the Ni atoms from the vapor to the solid. This results in Si atoms embedding into the Ni crystal structure during growth procedure. To confirm the appearance of Si, the as-grown nanowires were characterized by glancing angle x-ray diffraction and the result is shown in Fig. 2.5(b). The counts of the dominant peak at (200) are orders higher than the peaks at (111) and (220), proves the vertical growth of Ni nanowires along [200] direction. The appearance of the forbidden peak (100) in fcc-Ni indicates a small amount of doped-Si atoms disturbed the crystal structure and allow the (100) peak to show up.

2.3.2 Mangeto-resistance Measurements

The Ni nanowires were transferred to a separate Si/SiO_2 substrate for electrical transport measurements conducted using both 4-wire and 2-wire configurations by patterning electrodes on top of the nanowires as shown in Fig. 2.6(a). A 30-second RF bias was applied before the electrodes deposition to clean the oxides on the surface of nanowires for better contact. The patterned samples were then transferred into a Quantum Design PPMS system and the

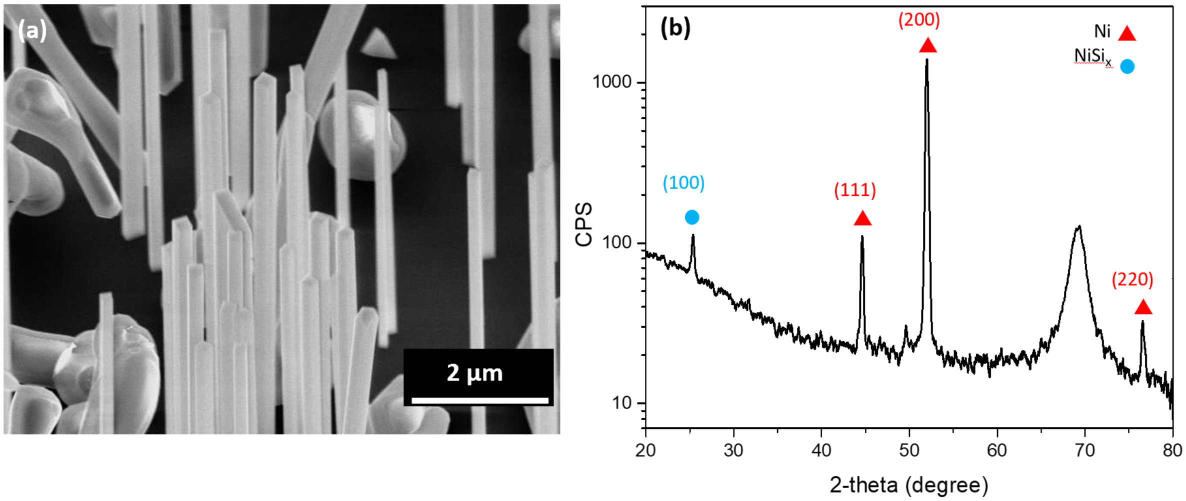

Figure 2.5. (a) SEM image and (b) XRD characterization of the as-grown single-crystalline, Si-doped Ni nanowires.

magneto-transport properties were measured over a temperature range of 10 – 400 K and also under magnetic fields up to 90 kOe. The gap between two voltage leads is fixed to 4 µm. By defining the resistivity as a function of relaxation time τ, the temperature and field dependence of resistivity could be describe[60] as

$$\rho_{total}(\tau) = c_1(1/\tau) + c_2(\omega_c\tau)^n \tag{2.12}$$

where ω_c is cyclotron frequency and n is a coefficient which usually have value in range 1 2. According to Matthiessen's rule, the total resistivity is additive among all electron scattering sources. There are some deviation terms to Matthiessen's rule[61] but are expected to be negligible in our measurement conditions. The assumptions above give good fits for our transport results. Below we give detailed discussion regarding the temperature dependence resistivity and MRs at low magnetic field and high magnetic field separately.

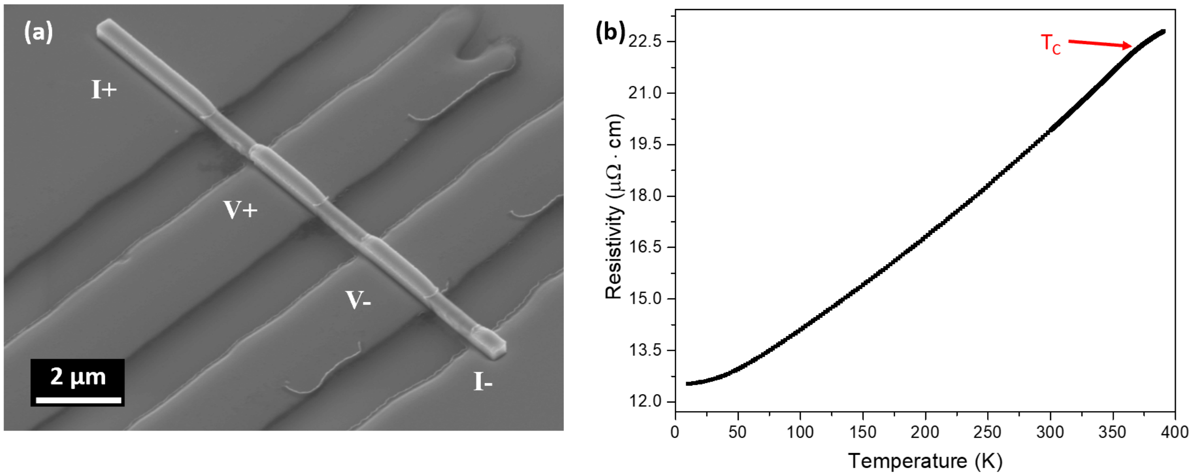

Figure 2.6. (a) SEM image of a Ni nanowire patterned with contacts for 4-wires transport measurement configuration. (b) Resistivity vs. T curve for a 0.4×0.4×12 μm^3 Ni-Si nanowire with a RRR value of 1.59.

2.3.3 Temperature Dependence of Resistivity

Figure 2.6(b) shows the resistance versus temperature curve, which gives a residual resistance ratio RRR equals to $\rho(300K)/\rho(10K)$=21.6 $\mu\Omega$cm/13.6 $\mu\Omega$cm=1.59. Compared to the reported RRR for the poly-crystalline Ni nanowires around 2-8[58, 62] and for the single-crystalline Ni nanowires around 2.8-4[58, 63], the fabricated Ni nanowires in our experiments have much smaller RRR values, indicating increased electron scattering process. Within the Drude model

$$\rho = m_e/ne^2\tau \tag{2.13}$$

where m_e is the mass of electron, n is the concentration of the electrons per unit volume, e is the elementary electron charge and τ is the relaxation time caused by different scattering sources. The corresponding mean free path l is given by

$$l = v_F\tau \tag{2.14}$$

$$v_F = \sqrt{2E_F/m_e} \tag{2.15}$$

In 3d ferromagnetic materials up and down spin channels contribute to resistivity separately. However, for Si impurities in Ni, the spin anisotropy ratio $\alpha = \rho_{\downarrow}/\rho_{\uparrow}$ = 1.3 [64],which means there is no significant difference between spin up and down current and simple form of mean free path can be used here. Taking the most commonly used values[52] of E_F = 7.3 eV, $n = 9.2 \times 10^{28}$ m^{-3} for Ni we obtain l= 2.2 nm from the low-temperature resistivity. If we assume we have 5 at.% Si impurities in our Ni NWs and they distributes uniformly in the crystal structure the average distance between each Si impurity atom is approximately 1.76 nm. This value is close to the estimated mean free path of the electrons in the nanowires and we can have a reasonable deduction that the residual resistivity is mainly attributed to the electron scattering from Si-impurities.

2.3.4 Mean Free Path of Electrons in Two-current Model

The classical image of resistivity gives us Equation 2.13. However, this is not a complete description in 3d ferromagnetic Ni materials, since up and down spins contribute to resistivity separately. In this case, two current model proposed by Fert[65] could be used to calculate the total resistivity. ρ_0 is the residual resistivity caused by impurities which is also independent of temperature and magnetic field. To only concentrated on the effects from impurities, we can use the resistivity value obtained at low temperature (10 K), where spin-mixing and spin-orbit coupling effects can be excluded. In this condition, we should have

$$\rho_0 = \rho_{imp} = \rho_{\uparrow}\rho_{\downarrow}/(\rho_{\uparrow} + \rho_{\downarrow}) \tag{2.16}$$

where ρ_0 usually equals to zero in pure perfect metals. $\rho_{\uparrow}$ and $\rho_{\downarrow}$ are the resistivity for up and down spins respectively and one always is majority spin and other is minority spin. Apparently, the total resistivity depends on the low resistivity channel, which is less scattered by the impurities.

Once we introduce impurities in Ni and form dilute alloy, the band structure, thus resistivity, for spin up and down will change independently and the spin anisotropy ratio $\alpha = \rho_\downarrow/\rho_\uparrow$ will change according to the type of impurity. This has been proven by both experimental methods and simulation. From previous study, Si impurity in Ni will have α = 1.3, which means spin up and spin down channel have similar resistivity and $\rho_{imp} = 0.57\rho_\uparrow = 0.43\rho_\downarrow$. Taking the most commonly used values as mentioned before and let $\rho_{imp} = \rho(10K)$, we could obtain $l_\uparrow$= 1.9 nm and $l_\downarrow$ = 2.6 nm. If we assume we have 5 at.% Si impurity in our Ni NWs and it distributes uniformly in the crystal structure, by taking the lattice constant for fcc-Ni equals to 0.352 nm and each unit cell contains 4 atoms, we could have an average distance between each Si impurity atom is approximately 1.76 nm. This value is close to the larger spin up mean free path $l_\uparrow$= 1.9 nm, which we could have a reasonable deduction that the residual resistivity mainly related to the distance between Si impurity. This is a complete computation for the previous section.

2.3.5 Si Concentration Dependent Curie Temperature

A second effect of Si doping in the Ni nanowires is the reduction of the Curie temperature T_c which can be determined from the non-linear behavior in $\rho vs.T$ near T_c. This can be seen in Figure 2.7 at temperature near 360 K where there is a clear change in the slope of $\rho vs.T$ curve. The T_c value shown here is much lower than the bulk Ni value[66] at 631 K. We believe this effect is due to the Si substitution in the fcc-Ni crystal structure. From the previous study[67], a 6.1 at.% Si impurities in Ni can reduce the T_c to approximately 400 K. For our sample where T_c=360 K, we could estimate the average atomic percentage of Si in of about 6.5 at.%.

Using the same sample geometry as shown in Figure 2.5, we probed dR/dT at different positions on the same nanowires. By conducting 2-wire measurements on the two side electrodes (from leads I+ to V+ and I- to V- as shown in Figure 2.5(a)) and 4-wire measurements for the middle part of nanowire, we can detect the $Rvs.T$ curves at different positions of the same nanowire. Figures 2.7(b) and (c) are measured resistivities and their corresponding derivatives with temperature from 300 K to 400 K for the three different positions on the same Ni nanowire.

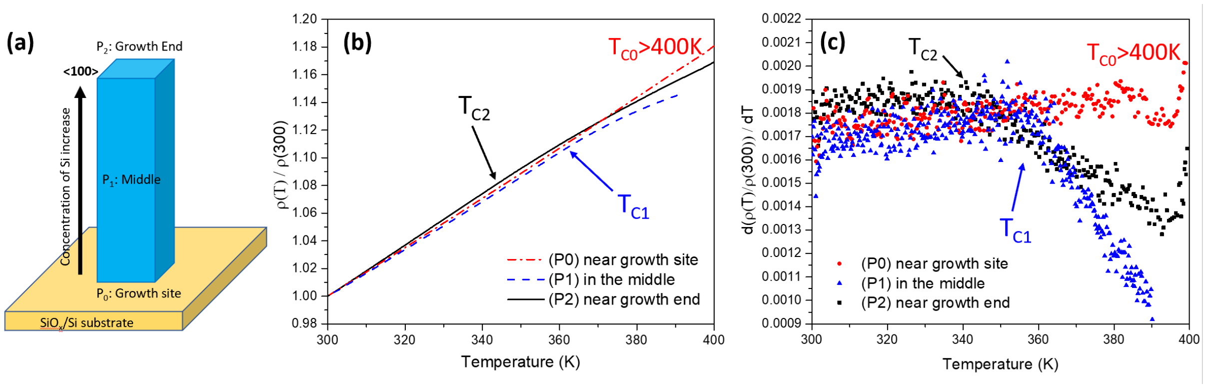

Figure 2.7. (a) Configuration of the increasing Si concentration along the NWs growth direction with the lowest near the growth site. (b) Resistivity versus temperature curves and (c) their derivatives from 300 to 400 K for three different position P0 (near growth site), P1 (near growth end) and P2 (in the middle of NWs).

The red dash-dot line represents the position near the growth site (P_0), the blue dash line represent position at the middle (P_1) of the nanowire and the black solid line represents the position near the growth end (P_2) as highlighted in Figure 2.7(a). From the measured curves in Figures 2.7(b) and (c), we can observe there is no transition in the slope at P_0, which means the $T_{c0} > 400$ K. The slope measured at position P_1 has a transition temperature $T_{c1} = 360$ K as mentioned above, and the transition measured at P_2 has a value $T_{c2} = 340$ K. We generally observe that T_c is the highest near the growth site and gradually decrease along the long axis of the nanowire until reaching the end of the growth side where shows the lowest T_c. We could not estimate the T_{c0} due to the maximum applied temperature is 400 K in our experiment setup, but it is still reasonable to conclude that this change of T_c in a single Ni NWs over position to growth site indicates there is a Si concentration gradient over the Ni NWs, with the lowest Si concentration near the growth site and highest concentration at the far end. From these measurements the Si concentration varies from below 6.1% to 7% along the length. This is consistent with observations that CVD grown Ni nanowires has a limited height, since the Si concentration on substrate is slowly depleted during the NW growth.[58]

2.3.6 Magnetoresistance Below Saturation Magnetic Field - AMR

In 3d ferromagnetic materials, the spontaneous magnetization by d-orbitals electrons gives additional resistivity terms including the AMR and DWMR which are magnetic field dependent below the saturation field. Here we define $\rho_{||}$ and $\rho_{\perp}$ are the resistivity for the nanowire when the magnetization is parallel and perpendicular to the nanowire axis, respectively, and define β is the angle between the external magnetic field and the long axis of Ni NWs $< 100 >$, θ is the angle between magnetization direction and the long axis of the Ni NWs as shown schematically in Figure 2.8(a). The magnitude of the AMR response of the wire is demonstrated by the $\rho vs.\beta$ curve in Figure 2.8(a) measured in a 10 kOe field. At this field the magnetization is saturated and follows the applied field and the resistivity shows the expected $\rho(\beta) = \rho_{||} - (\rho_{||} - \rho_{\perp})sin^2(\theta)$. The resistance is highest for θ = 0° and 180° where M is parallel to the current and lowest for θ = 90° and 270° when M is perpendicular to the current. Figure 2.8(b) shows the normalized magnitude of the AMR signal $(\rho_{||} - \rho_{\perp})$ $vs.$ temperature where the magnitude decreases with temperature going to zero at T_C.

The normalized MR curves $\rho(H)$ $vs.$ H at multiple temperatures are plotted in Figure 2.8(c) for the applied field either parallel (0 degrees) or perpendicular (90 degrees) to the nanowire axis. The MR signal appears below 370 K, seen as a small difference between the resistivity for the field applied parallel and perpendicular to the wire axis, consistent with the estimated T_c. This is shown in an expanded view in Figure 2.8(d). For T = 300 K and above the θ = 0° curves are featureless at low fields while the θ = 90° curves decrease from zero field and then saturate. This shows the magnetization of the nanowire is along wire axis at zero field which is consistent with the magnetic response being dominated by shape anisotropy of the nanowire geometry.

The shape of the MR curve in Figure 2.8(c) starts to change around 250 K where there a minimum occurs in the 0-degree $\rho_{||}(H)$ curves near zero field. The MR curve is nearly reversible with a finite saturation field. This behavior indicates the remanent magnetic state is no longer along the nanowire axis as expected from shape anisotropy of the NW. The minimum of the

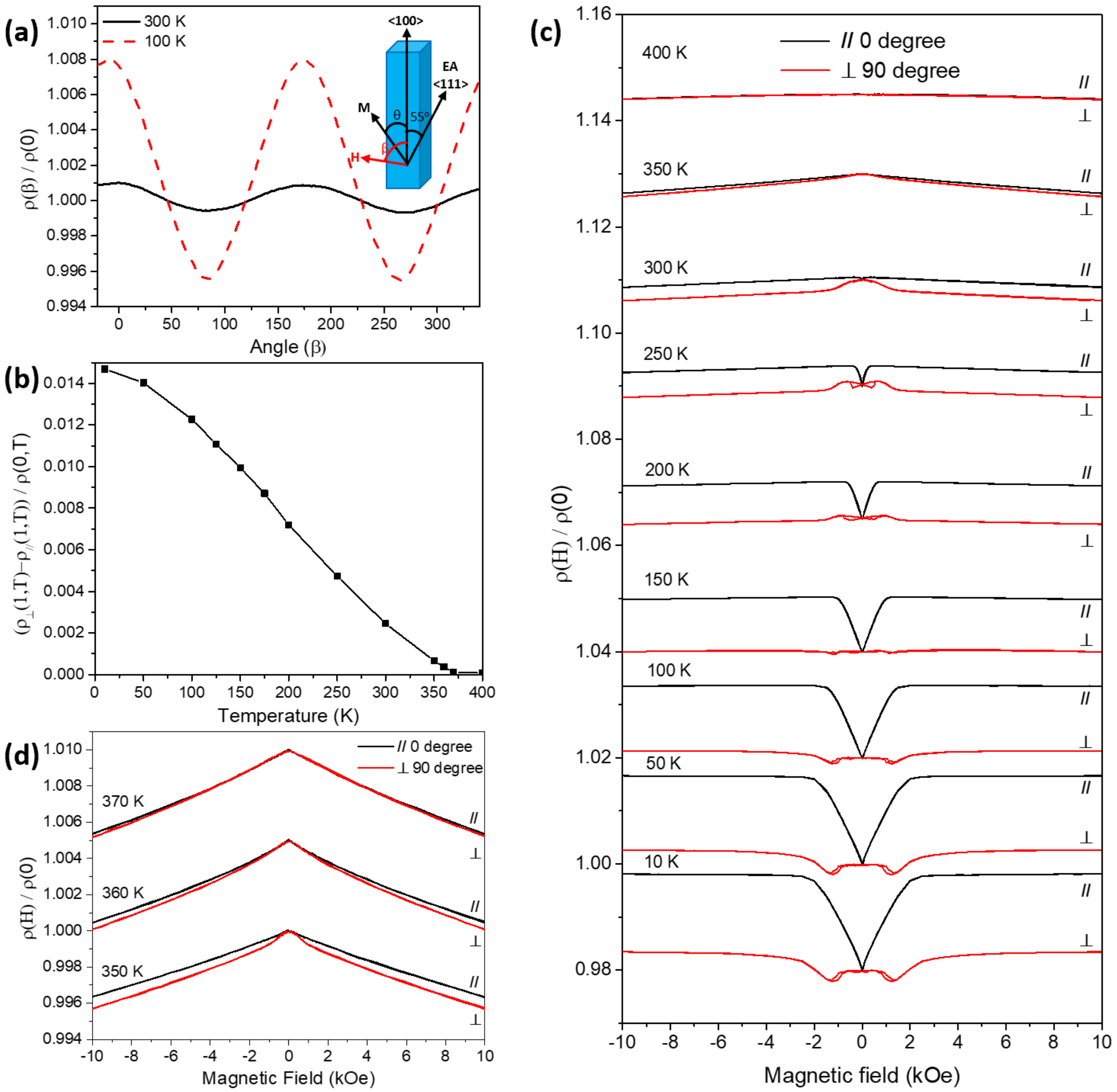

Figure 2.8. (a) AMR curves versus the angle between current direction (along the NW axis) and the external magnetic field (10 kOe). (b) Normalized AMR values $(\rho_{||}-\rho_{\perp})$ vs. temperature measured. (c) Field dependent MR curves measured with the applied field parallel (black) and perpendicular (red) with respect to the long axis of the Ni NWs. (d) Expanded view of MR curves from 350 to 370 K.

$\rho_{||}(H)$ curves decreases and the saturation field increases with decreasing temperature. By 200 K the MR curves indicate the remanent magnetization is nearly perpendicular the current and the nanowire axis. Similar MR curves have been seen previously in single-crystal nanowires[58, 55] and this behavior was attributed to the strong temperature dependence of the magneto-crystalline anisotropy of Ni which prefers the Ni $< 111 >$ easy axis which is an approximate 55° angle with respect to the $< 100 >$ long axis of the Ni nanowires (see inset of Figure 2.8(a)). The competition between the shape and magneto-crystalline anisotropy can further leads to complex domain patterns including periodic domains along the length of the wire[68]. However, in these previous studies the remanent MR values were roughly intermediate between the $\rho_{||}$ and $\rho_{\perp}$ values in saturation. In the current more heavily Si-doped wires the remanent state appears roughly perpendicular to the wire axis. We will discuss this in more detail below.

2.3.7 Calculated Anisotropy Energy and Saturation Magnetization values by the Stoner Model

We explain the saturation fields by a competition between the anisotropic energy terms. In single-crystalline Ni nanowires, usually there are two anisotropic energies governing the AMR behaviors, shape and cubic magneto-crystalline anisotropic energies. Both are expected to be strongly temperature dependent. In bulk Ni the magnitude of the negative first-order cubic anisotropy term K_1 increases with decreasing temperature and it follows the empirically equation[69, 70]:

$$\frac{K_1(T)}{K_1(0)} = (1 - c\frac{T}{T_C}(\frac{M_s(T)}{M_s(0)})^b \tag{2.17}$$

Here $K_1(T)$ and $K_1(0)$ are the anisotropy constant for Ni at temperature T and $T = 0$ respectively. $M_s(T)$ is the saturation magnetization at temperature T. b and c are coefficients depends on the materials. To estimate $K_1(T)$ and $M_s(T)$ at each temperature, we use the Stoner-Wohlfarth (SW) model[71] for analysis of the saturation fields. We make the simplifying assumption to use the shape anisotropy of a cylindrical wire and ignore higher-order magnetic anisotropies. Due to the shape anisotropy, the difference of saturation fields between parallel field and perpendicular field equals to $H_{\perp sat} - H_{||sat} = 2\pi M_s$. From this relationship, we can easily get the M_s by extracting $H_{\perp sat}$ and $H_{||sat}$ from the experiments. We note that if there is a magnetostrictive anisotropy that is uniaxial then this will contribute to the extracted M_s values. By considering the competition between crystalline anisotropy and shape anisotropy and solve the energy equation, we can get the perpendicular saturation field as:

$$H_{\perp sat} = \frac{-2K_1 + 2\pi M_s^2}{M_s} \tag{2.18}$$

The experimental $H_{\perp sat}$ and $H_{||sat}$ are extracted from the AMR curves in Figure 2.8(a) by finding the point when the slopes become flat. The resulting K_1 and M_s at different temperatures are listed in Table 2.1. From the resulting data, we found that the M_s at low temperatures are slight smaller than the bulk Ni value (484 emu/cc) but are much lower than the bulk value above 100 K reflecting the lower T_c. The values and trend of K_1 are in the same order as the previous studies[69, 72, 73] below 100 K but there is increasing discrepancy at higher temperatures, mainly due to the reduction of the T_c. In Fe-Si system[74], a small amount of Si impurities can lead to a large decrease in the magnitude of K_1, which could be the same case in our Ni-Si system. By extrapolating the existing data, we can get $M_s(0)$ = 433 emu/cc and $K_1(0)$ = -6.2×10^5 erg/cc. From the $\rho_{||}(H)$ in Figure 2.8(c), $K_1(T)$ changes sign around 330-340 K, slightly lower than the T_c =370 K. By fitting the Equation 2.17, we get coefficients b=1.87±0.02 and c =1.1 in our system. The value for b deviated significantly from the 10^{th} power law in bulk Ni. This might be owing to the Si impurities weaken the interaction between the Ni atoms and reduces the magneto-crystalline anisotropy energy.

2.3.8 Mumax3 Micromagentic Simulations for Nanowire

To understand the micromagnetic response, and to understand the shape of the MR curves micromagnetic modeling was done using the MuMax3 micromagnetic simulator as we introduced in previous section. The nanowire is subdivided into 512×16×16 cells defined by

Table 2.1. Experimentally measured saturation fields at different applied field angle and temperatures, and the extracted M_s and K_1 values.

Temperature (K)	$H_{\|\|sat}$ (Oe)	$H_{\perp sat}$ (Oe)	M_s (emu/cm^3)	K_1 (erg/cm^3)
350	0	800	128	>0
300	200	1600	223	-0.2×10^5
250	450	1900	231	-0.5×10^5
200	850	2600	279	-1.2×10^5
150	1300	3400	334	-2.2×10^5
100	1850	4350	398	-3.7×10^5
50	2550	5100	406	-5.2×10^5
10	2800	5500	430	-6.0×10^5

Table 2.2. Simulated results of saturation fields at different applied magnetic field and temperature compared to experimental values.

	Experiments		Simulations	
Temperature (K)	$H_{\|\|sat}$ (Oe)	$H_{\perp sat}$ (Oe)	$H_{\|\|sat}$ (Oe)	$H_{\perp sat}$ (Oe)
350	0	800	0	850
300	200	1600	200	1600
250	450	1900	450	1800
200	850	2600	800	2600
150	1300	3400	1300	3200
100	1850	4350	1800	4100
50	2550	5100	2300	5000
10	2800	5500	2750	5200

cubic shape elements with 20 nm in length for each cell. The exchange stiffness constant is set to 5×10^{-7} erg/cm. The simulated saturation fields at different temperatures and magnetic field angles are listed in Table 2.2. The simulated saturation fields are consistent with the data from Equation 2.18 which were extracted from experimental MR curves. This proves the validation of Equation 2.18 and simulation model. After getting the magnetic states in each cell, we can start to calculate the AMR in the nanowire.

2.3.9 AMR Simulation Model

The total MR curves are calculated from the micromagnetic results by calculating the AMR response in each cell and then calculating the resistance of the nanowire assuming a uniform current. The parallel pipes model has been applied here. As shown in Figure 2.9, in this model we are assuming electrons are moving in several individual channels which in parallel to each other and each channel are consisting of hundreds of individual small cells from the micromagnetic simulation grid and connected in series. By treating each small cell as a resistor, we can calculate the AMR of each small cell according to the Equation 2.7 by calculating the angle between the magnetic moment in cell and the current direction which is applied along Z direction of nanowire. Then the total AMR of the Ni nanowire can be calculated as pipe resistance first and then put parallel pipes together:

$$R_{pipe11} = R_{111} + R_{211} + ... + R_{i11} \tag{2.19}$$

$$\frac{1}{R_{total}} = \frac{1}{R_{11}} + \frac{1}{R_{12}} + ... + \frac{1}{R_{jk}} \tag{2.20}$$

then the total resistance is normalized from 0 to 1 and compared with experimental data.The resulting simulated AMR curve at 300 K compared to the experiment MR curve are plotted in Fig. 5(a). As shown in the figure, experimental MR curve is well fitted by the model. The negative slope above saturation field comes from electron-magnon scattering discussed below and a linear slope consistent with the experimental data was added to the simulated AMR curve.

Figures 2.10(b) and (c) show the micromagnetic configurations at various external magnetic field parallel to z-axis (+x and -x component of moment shown in color) and perpendicular to z-axis of NWs (+z and -z component of the moments), respectively. As shown in Figure 2.10(b), when scanning the field along z-axis of the NW from 10 kOe to zero, the magnetic moments aligned along z-axis at high field and split into two opposite domains at zero field with a small tilt towards the magnetic which leads to a small drop in resistivity near the zero field. For the field scanned perpendicular to z-axis of NW, the magnetic moments aligned along external field direction at high fields and then start to show two domains at relative lower field

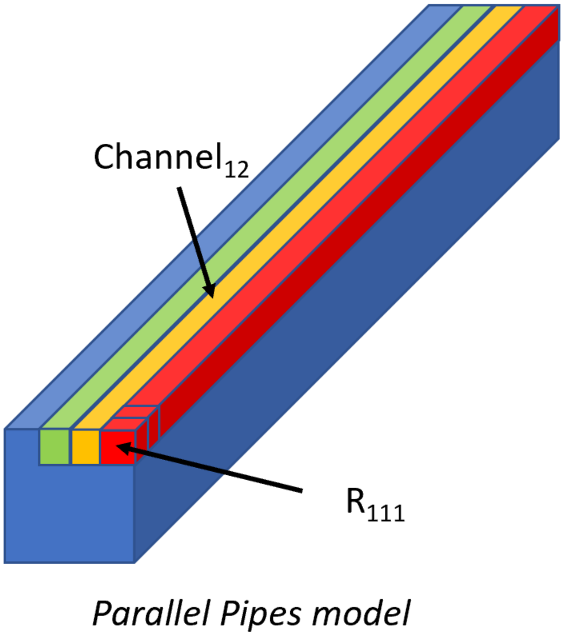

Figure 2.9. Brief configuration of parallel pipes model

and slowly merged into a dominant domain aligned to z-axis of NW at zero field. These results are consistent with the magnetic response dominated by shape anisotropy energy of the wire.

An additional feature emerges in the experimental MR curves near T = 100 K and below that is not understood from the calculated AMR curves. The $\rho_{\perp}(H)$ curves show minima at +/- 1-2 kOe prior to saturations with a small amount of hysteresis. This is shown more clearly in Figure 2.11(a) which expands the T = 10 K curves in Figure 2.8(c). This is compared to simulated AMR curve. Clearly, the AMR model is not sufficient at lower temperatures as shown by the large discrepancy between experimental MR and simulated AMR curves. In Figure 2.8(c), at T = 100 K there are hysteretic peaks in the $\rho_{\perp}(H)$ curves that evolve to mimina at T = 10 K. These minima cannot be simply explained by the AMR effect, since the minimum resistivity is below the saturation resistivity for $\rho_{\perp}(H)$ which should be the lowest resistance (Figure 2.8(a)). We contribute this effect to the domain wall resistance. The coming section will discuss this effect in detail.

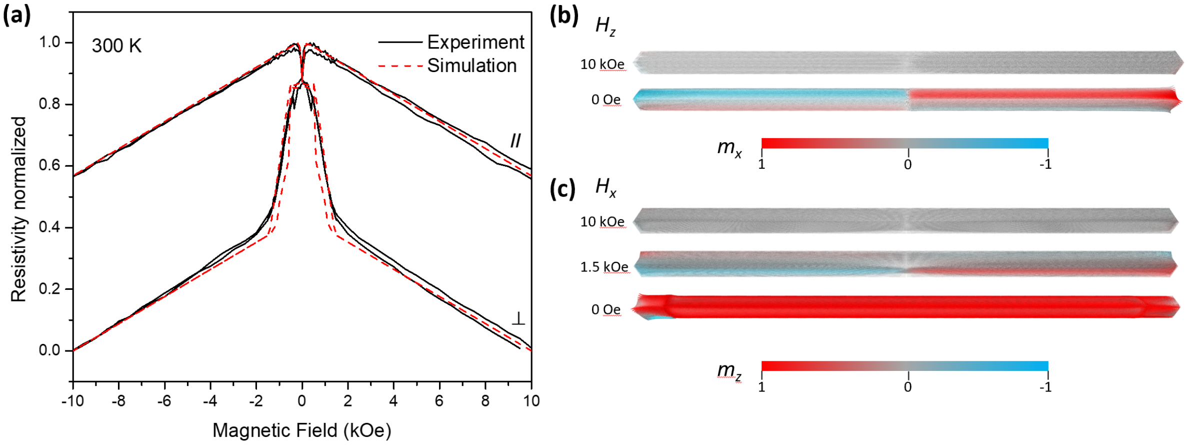

Figure 2.10. (a) Experimental AMR curve (black solid) measured at 300 K and simulated AMR curve (red dash). (b) Magnetization configuration of micromagnetic simulations at different external magnetic field applied (b) parallel to z axis (long axis) of NWs and (c) perpendicular to z axis of NWs.

2.3.10 Domain Wall Resistance Contribution to AMR at Low Temperature

These low-temperature resistance anomalies most likely result from the additional contributions of DWMR. Previous experimental studies[49, 75] on ferromagnetic wires showed the DWs have a negative contribution to the resistivity, which means the appearance of DWs will reduce the resistivity of the NWs and the magnitude of reduction is proportional to the density of the DWs along the NWs. In these papers it was suggested that DWs increases the mean free path of electrons and reduces the surface scattering and result in a reduction in resistivity. Theoretical works[48, 51] further suggests that the appearance of DWs will lead to a reduction in weak-localization scattering caused by impurities in ferromagnetic materials. This is due to a weaker back-scattering quantum interference (quantum decoherence) at low temperature. Noted by the author, the DWs suppress the interference due to random impurity scattering and the higher the concentration of impurities, the larger magnitude of reduction in resistivity. In our Ni NWs, Si impurities are up to 7 at.% resulting in a strong weak-localization scattering effect.

Previously studies on similarly prepared single-crystal Ni NWs showed a periodic domain pattern that were reproduced by the micromagnetic simulation.[68] In particular, micromagnetic calculations found that when as the field is reduced from saturation perpendicular to the wire that in the vicinity of 2.5 kOe, a precursor oscillatory state develops with the magnetization varies periodically along the nanowire axis with period of oscillation approximately 222 nm. Here we are using the parameters from Table 2.1 and running simulations at 10 K. The magnetization configurations at different field values aligned to z-axis of NW and perpendicular to z-axis of NW are shown in Figures 2.11(b) and (c), respectively. Similar to the case at 300 K, when slowly scanning magnetic field parallel to the z-axis of NW from 10 kOe to zero, a single domain state breaks into few random domains as shown in Figure 2.11(b) at zero field. The resulting $\rho_{\perp}(H)$ shows a minimum at zero field due to the magnetizations tilts between the Ni $< 111 >$ and $< 001 >$ easy axis. However, as shown in Figure 2.11(c), the magnetization configuration under field perpendicular to z-axis of NW, shows a periodic oscillation of domains along z direction at lower fields. While similar to what is observed in Ref. [68] the current micromagnetic simulation shows the periodic oscillation of domain structure can still form at remanence without abruptly removing the external field. We believe the appearance of these domain patterns are strongly affecting the MR curves. This periodic oscillation of domains is formed mainly due to the competition between shape anisotropy (easy axis along $< 001 >$) and magnetocrystalline anisotropy (easy axis along $< 111 >$). The forming of the periodic domain pattern dramatically increases the density of the DWs length of the wire leading to increasing contribution from DWMR.

To understand the abnormal MR curve, we posit the following explanation based on simulation results. During the process of scanning field from 10 kOe to 0 Oe at 10 K, the simulation results show it can be divided into 3 different magnetic states which can properly describe the corresponding behavior of experimental AMR curve. 1) Above the H_s (5.2 kOe), all spins are aligned along the external field and no domains formed. 2) When field is below H_s domains start to nucleate, and DWs density and contrast increases with the decreasing field until reach the peak domain density H_{pd} at 1.5 kOe where the 'dips' in resistivity appear in the experimental MR curves. 3) From H_{pd} to zero field, the periodic oscillation of domains become

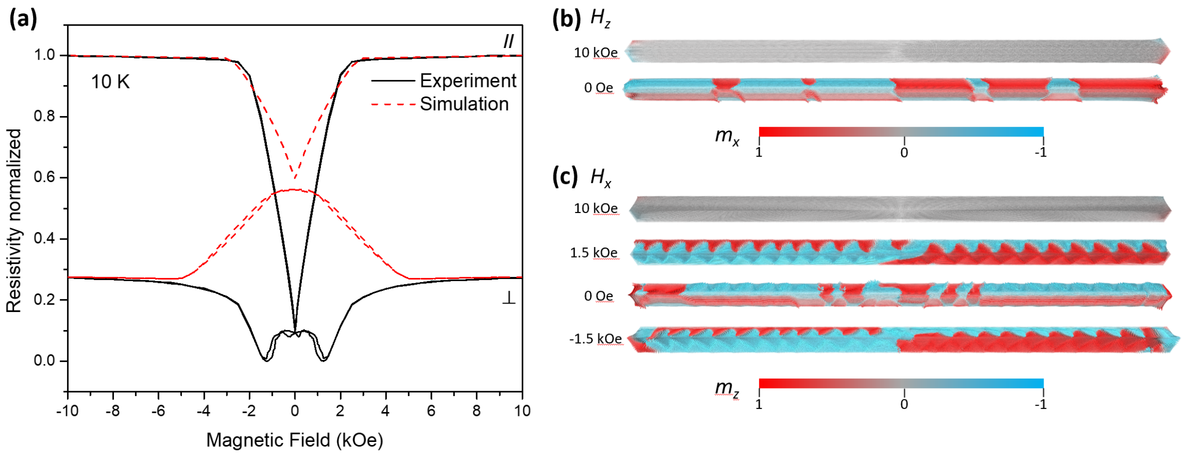

Figure 2.11. (a) Experimental MR curves (black solid) and simulated AMR curve (red dash) at 10 K. Magnetization configurations extracted from micromagnetic simulations at different external magnetic fields (b) parallel to z axis (long axis) of NWs and (c) perpendicular to the z axis of NWs.

more disordered, leading to a decrease in DWs density which corresponds to the slightly higher resistivity state experimentally observed at remanence. Note that the periodic oscillation domains symmetrically reappear at -1.5 kOe where the experimental MR curves also shows a dip at this field.

2.3.11 Fitting AMR Curve by Considering Domain Wall Magnetoresistance

To illustrate the calculated magnetization configuration of the NW, zoomed-in and cross-sectional views of the magnetization configuration are shown in Figures 2.12(a) and (b). The wavelength for the periodic domains is approximately 420 nm at 10 K. The magnetization configuration at +z and -z direction shows different periodic patterns compared to +x and -x direction, indicates the electrons might scatter differently at different paths. Cross-sectional views along half wavelength are shown on the right of each figure. These cross-section figures show that the magnetization along two directions have a repeated switching of magnetization direction along z-axis which is the direction of current flow. The formation of DWs could give rise to DMWR and thus a reduction in in resistivity. To explore the relation between domain wall density and the observed low resistivity state observed, we plot normalized domain wall density under perpendicular magnetic field along M_x, M_y, M_z directions and also the average of three $< M >$ as shown in Figure 2.13(a). It can be clearly seen that the peak domain wall densities fall at around +/- 1500 Oe at all directions, which indicates the highest contributions from the domain walls to the resistivity of nanowires. Here if we assume the domain wall resistivity is proportional to the domain wall density $\Delta\rho \propto f(DWD)$ and the experimental MR (expMR) curves are mainly affected by the positive normal AMR and negative DWRM, we should have the domain wall density

$$f(DWD) \propto \Delta\rho = \Delta\rho_{simuAMR} - \Delta\rho_{expAMR} \tag{2.21}$$

This means the trend in $f(DWD)$ and $(\Delta\rho_{simuAMR} - \Delta\rho_{expAMR})$ curves should be the same. To verify this assumption, the $f(DWD)$ (red dash) and $(\Delta\rho_{simuAMR} - \Delta\rho_{expAMR})$ (black solid) curves are plotted in Figure 2.13(b). Apparently, the peak of the domain wall density is the same as the peak of $(\Delta\rho_{simuAMR} - \Delta\rho_{expAMR})$ curve, illustrates the negative resistivity contribution is related to the domain wall density. Besides the domain wall density, the magnitude of oscillation will also affect the magnitude of the negative resistance. From the simulation result, we observed the magnitude of oscillation is proportional to $(1- < M >)$, which means the higher the magnetization, the less the magnitude of oscillation. To take account into this effect, we multiple the domain wall density with the complement of the 1 to average magnetization $< M >$, which result in equation $f(DWD) \times (1- < M >)$ as shown in Figure 2.13(b) in blue dash dot line. The resulting curve fits better with curve $(\Delta\rho_{simuAMR} - \Delta\rho_{expAMR})$. This kind of behavior was not observed in the purer Ni NWs, presumably due to better purity, suppresses the weak-localization scattering.

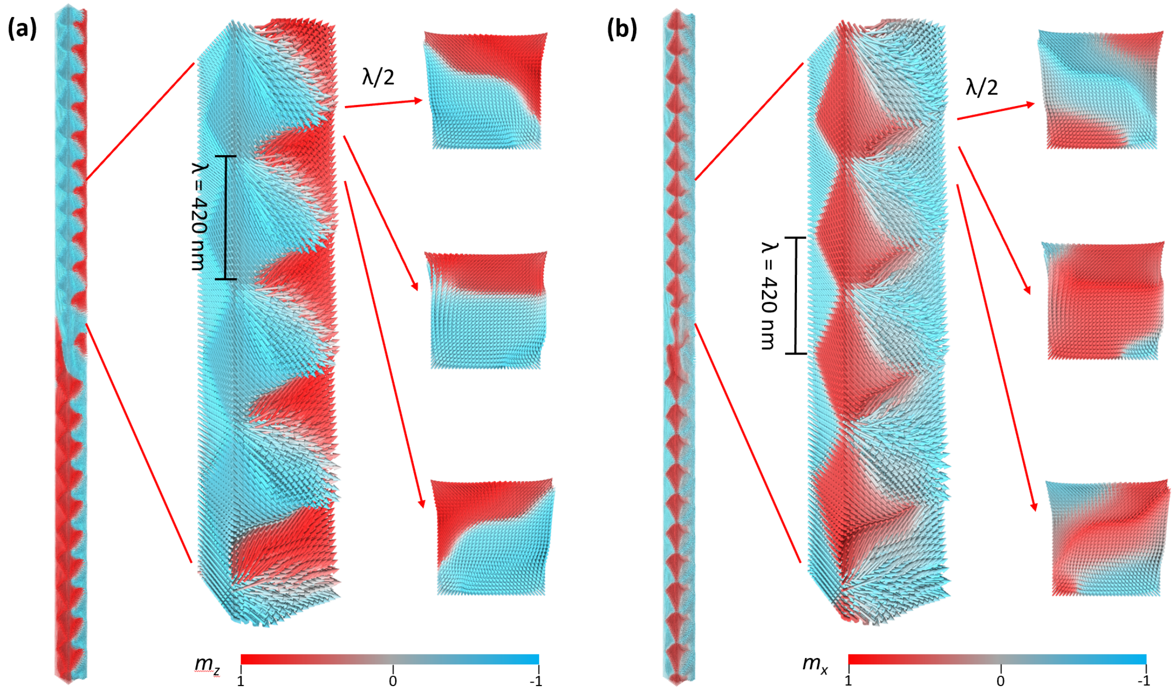

Figure 2.12. Magnetization configurations from micromagnetic simulations showing (a) z-axis component and (b) x-axis direction component. Cross-sectional configurations are shown on the right of each figure.

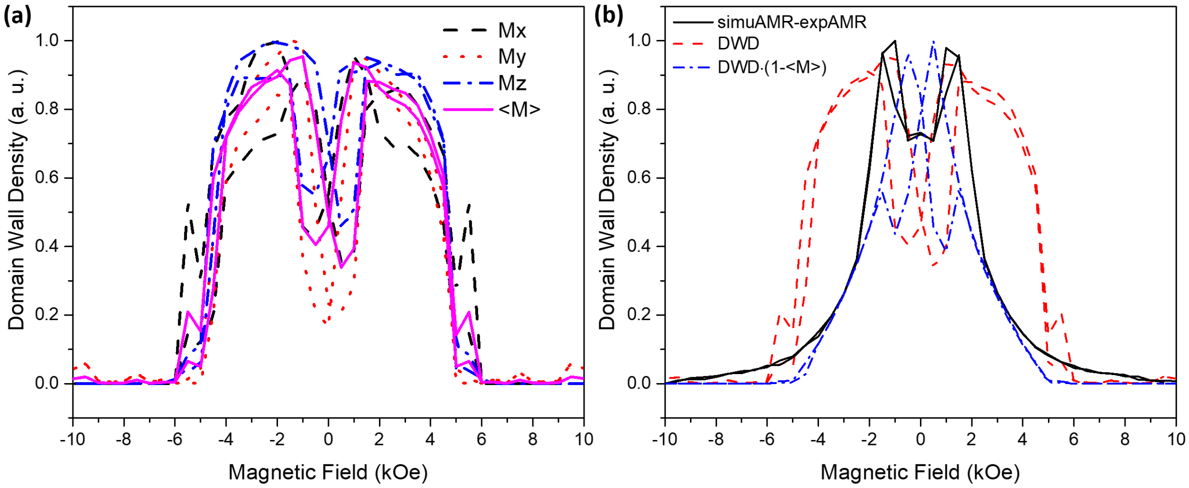

Figure 2.13. (a) Normalized domain wall densities counted under perpendicular magnetic field along M_x, M_y, and M_z directions and the average magnetization $< M >$ of all directions. (b) The subtraction of simulated AMR curve and experimental AMR curve compared to domain wall density and domain wall density times the complement of 1 to the average magnetization $(1- < M >)$. These two three curves are showing the same trend.

2.3.12 Magnetoresistance Above Saturation Magnetic Field - Electron-magnon Scattering

The normalized magnetoresistivity at various temperatures under high applied magnetic fields either parallel (β = 0°) and perpendicular (β=90°) to the NW axis are plotted in Figures 2.14(a) and (b), respectively. The magnetization is saturate by H_s = 5 kOe. There is no significant difference in the behavior for the orientation of the applied field above H_s. The slope of the $\Delta\rho$ monotonically increase from negative to positive with the decrease of temperature due to the competition from contributions of the electron-magnon scattering $\Delta\rho_{e-m}(T,B)$ and the ordinary magnetoresistance $\Delta\rho_{OMR}(T,B)$. Even though our samples are single crystalline the doping of Si results in the relaxation time is dominated by impurity scattering. In this case, the relaxation time τ is weakly dependent on the temperature. The electron-magnon term $\Delta\rho_{e-m}$ will increase with temperature, while the OMR term $\Delta\rho_{OMR}$ should be much weaker compared to pure Ni. Raquet[52] proposed the following equation to estimate the contribution from electron-magnon scattering:

$$\Delta\rho_{e-m}(T,B) \approx \Delta\rho_{e-m}(T,B) - \Delta\rho_{e-m}(T,0) \propto \frac{BT}{D(T)^2} ln \frac{\mu_B B}{kT} \tag{2.22}$$

where μ_B is Bohr magneton, k is Boltzmann constant and $D(T)$ is the spin-wave stiffness. Researchers have found that the spin-wave stiffness can be described empirically as[76, 77]

$$D(T) = D_0 - D_1 T^2 - D_2 T^{5/2} \tag{2.23}$$

In most of the cases, D_2 is negligible being a few orders smaller than D_1. In ferromagnetic Ni nanowires, if we ignore the demagnetization field when the field is parallel to the wire axis, the internal magnetic flux density $B = H + 4\pi M_s$. To fit all the data to Equation 2.22 we extracted the temperature dependence of MR slopes using the expression from Ref. [54]:

$$\frac{\partial \Delta\rho_{e-m}(T,B)}{\partial B} \propto T(1 + 2d_1 T^2)(lnT + cte) \tag{2.24}$$

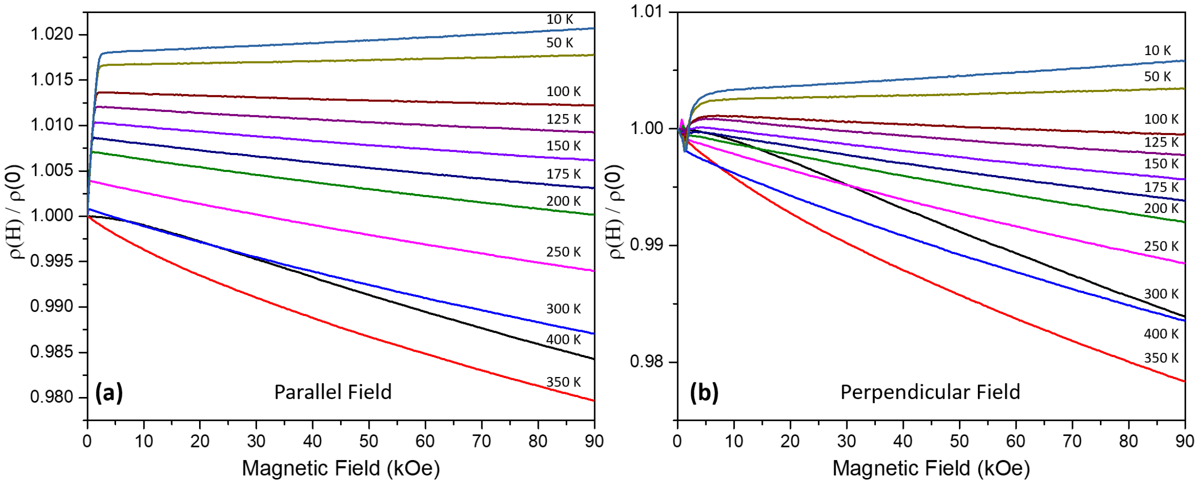

Figure 2.14. Normalized resistivity versus magnetic field at (a) parallel and (b) perpendicular field respect to the z-axis of nanowire.

where $d_1 = D_1/D_0$ and term cte is temperature independent. The extracted slopes from parallel field data at different temperature are plotted in Figure 2.15 as black squares. The anomalous data point measured at 400 K is due to the fact that the temperature is above T_c. The slopes below T_c gradually increase from negative at high temperature to positive at low temperature due to the changing magnetization and the increasing contribution of electron-magnon scattering. Note that the curves become non-linear above 300 K. It has been known that above at least $T_c/2$, the impact from Stoner excitations and appearance of optical mode in magnons will give rises to the disorder of spins, leading to a more negative slope in MR. Thus, by fitting the parallel field data using Equation 2.23 in the temperature range of 100 K to 250 K, we obtained the fitted curve as shown in Figure 2.15 as the red solid line and extrapolated to zero temperature shown as the red dashed line. Using this method, the extracted d_1=1.097×10^{-5} K^{-2}.

2.3.13 Modified Magnon-Electron Resistivity by OMR

The fitted line could not fully overlap with the experimental data and the extrapolated line has a discrepancy at low temperature region. The extracted d_1=1.097×10^{-5} K^{-2}, which is almost 10 times larger than the bulk Ni (d_1=1.5×10^{-6} K^{-2}). The reason for this discrepancy is owing to the contribution from the OMR. However, due to the Si doping, the $1/\tau = 1/\tau_{imp} + 1/\tau_{pho} \approx 1/\tau_{imp}$ and τ_{imp} is weakly dependent on the temperature. We observe a linear positive slope mainly due to the OMR and use the approximate equation for the contribution from the OMR:

$$\Delta\rho_{OMR}(T,B) = \Delta\rho_{OMR}(B) = c_2(\omega_c\tau_{OMR})^n \approx c_2(\frac{eB}{m_e c}) \propto B \tag{2.25}$$

Adding 2.25 to 2.22 and get the partial derivative to the internal field B, we have:

$$\frac{\partial\Delta\rho_{e-m}(T,B)}{\partial B} \propto T(1+2d_1T^2)(lnT + cte) + a \tag{2.26}$$

where $a = c_2e/m_ec$ is a constant related to the OMR effect. Using this equation, we can fit the data from 10 K to 250 K as shown in Figure 2.15 as the solid blue line and extracted parameter d_1=2.11×10^{-6} K^{-2}, which is slightly higher but consistent with values reported Ni (d_1=1.5×10^{-6} K^{-2}). The modified equation gives a more consistent parameters compared to previous reported values, proves the validation of this modified version.

2.4 Conclusion

We fabricated and conducted temperature- and field-dependent transport measurements on Si-doped single-crystalline Ni nanowires. The T_c=350-450 K and RRR = 1.59 values as attributed to a relative large Si incorporation during fabrication. Further we observe a gradient in T_c over the growth direction NWs that is attributed to a Si concentration gradient. This is consistent with a previously proposed growth mechanism where Si atoms on the substrates are consumed over the time. The MR response is understood as a combination of AMR and a large contribution of the DWMR effects at low temperatures. Both the AMR and DWMR contributions result from the complex domain pattern arising from the competition between shape anisotropy and magnetocrystalline anisotropy. The calculated M_s and K_1 have similar trends as pure Ni but with smaller magnitude due to the lower T_c. The high-field MR is understood from contributions

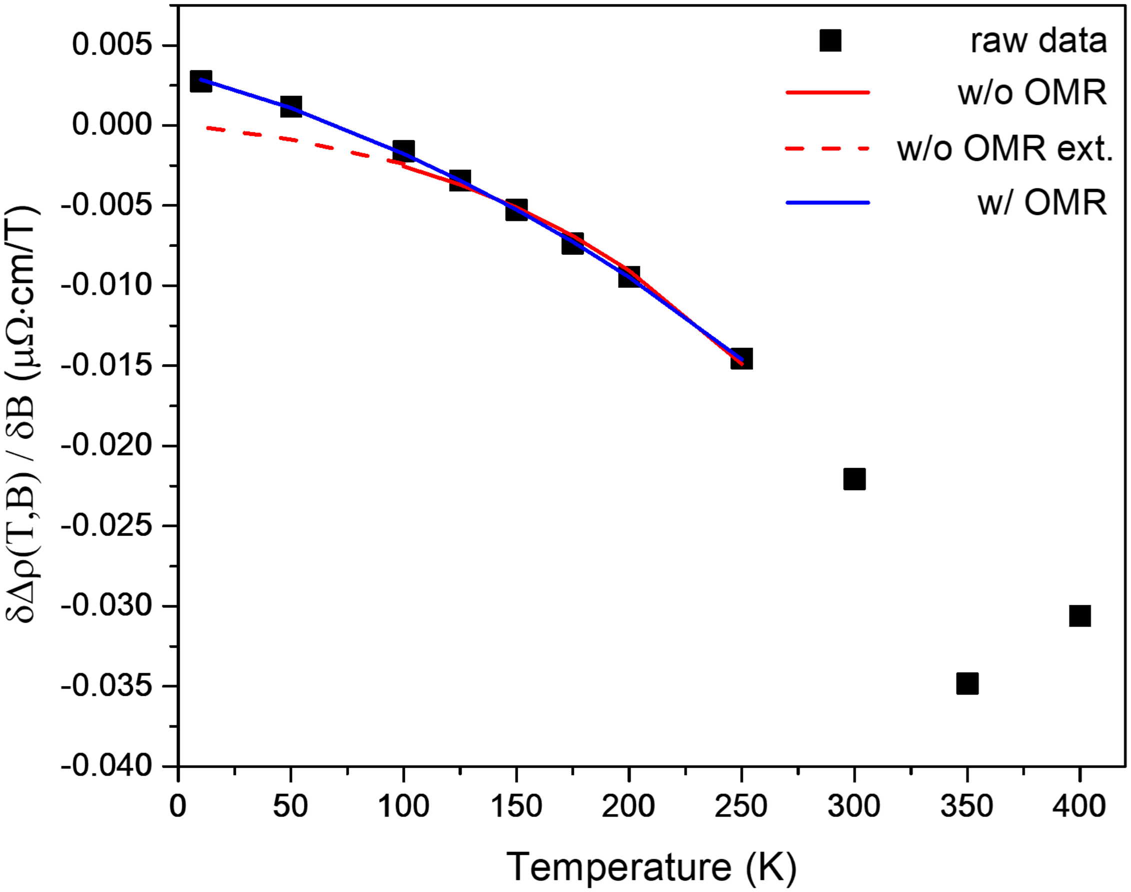

Figure 2.15. Change of magnetoresistivity slopes vs temperature curves. Black square point is the experimental results, red solid and dash lines is fitted without considering OMR effect and blue solid line is fitted with OMR effect.

from both OMR and spin-wave scattering and is consistent with significant impurity scattering in the NWs.

2.5 Acknowledgement

Chapter 2, in part, is currently being prepared for submission for publication of the material ”*Temperature-dependent magnetoresistance in Si-doped single-crystalline Ni nanowires*”, Haowen Ren, Sohini Manna, Eric E. Fullerton. The dissertation author was one of the primary investigators and author of this material.

Chapter 3

Spin-Triplet Superconductivity Spintronics

3.1 Introduction

Superconductivity is a physical phenomenon that can be observed in some specific materials, such as Nb, Al, and YBCO, etc., where electrical resistance vanishes and magnetic flux fields are expelled from the internal of the material below the superconducting critical temperature (T_C). This type of materials are called as superconductor. The most successful theory of predicting the properties of conventional superconductors is the Bardeen-Cooper-Schrieffer (BCS) theory. According to this theory, once the temperature are lower than the superconducting critical temperature of the material, free electrons in the crystals start to form spin-singlet Cooper pairs due to the electron-phonon interaction, which are pairs of electrons that process opposite direction of spins. This will lead to diminished electrons scattering when they are traveling in crystal lattice and thus zero electrical resistance in the materials. However, the conventional superconductors are not compatible with ferromagnetic materials due to their spontaneously internal magnetic field which will suppress the formation of spin-singlet Cooper pair. The singlet Cooper pairs can only process a short diffusion length (typically a few nanometers) and short survivor time when penetrate into the ferromagnetic materials. To make Cooper pairs exist in ferromagnetic materials, spin-triplet Cooper pairs are introduced in this chapter. In this chapter, we will focus on the experiments regarding the spin-triplet spin valves fabrication.

3.1.1 Spin-triplet Superconductivity

Most of the studies in the past focus on the conventional spin-singlet superconductivity, where Cooper pairs must be in a spin-singlet antisymmetric state as shown in Figure 3.1. An interesting topic in superconductivity study is the proximity effect when superconductors (S) are deposited next to the non-magnetic metals (N). Back to 1960s, Andreev[78] proposed that the proximity effect is caused by the Andreev reflection when an electron diffuses form N to S, it will produce a hole in N and generate a Cooper pair in S. This will lead to a long-range diffusion length of Cooper pairs in N which can be up to hundreds of nanometers.

Recently, researchers start to investigate spin-triplet superconductivity, which usually happened in ferromagnetic (F) materials contacting with superconducting materials. The spin-triplet Cooper pairs are consisting of two electrons in three different combinations of spins: with opposite spin sign, with two up spins, and with two down spins as shown in Figure 3.1. The mechanism of spin-triplet superconductivity has been explained by theories[79, 80, 81]. From these theories, the spin-triplet superconductivity can be produced when an inhomogeneous magnetic moment layer is introduced between the magnetic layer and superconducting layer. This inhomogeneous moment can convert the Cooper pairs from singlet state to triplet state. There are some evidences showing the existence of the spin-triplet Cooper pairs. In 2001, Kontos et al. [82] observed oscillatory behavior in density of state in Nb/$Pd_{1-x}Ni_x$ bilayers with the change of the thickness of PdNi layer, a sign of spin-triplet Cooper pairs. Since the incompatibility of ferromagnetism and superconductivity, it only exhibit a few nanometers of proximity effect. Later, Keizer et al. [83] found supercurrents can survive in CrO_2 (half metallic ferromagnetic materials) over 300 nm when contacting with superconducting leads on top. More interestingly, Wang et al. [84] deposited tungsten leads on top of a single-crystalline Ni and Co nanowires via the FIB and they observed a long-proximity effect in the ferromagnetic nanowires over a few hundreds of nanometers. They believe that the high energy ion beam can create a disorder phase at the interface between S and F layer, which will introduce an inhomogeneous

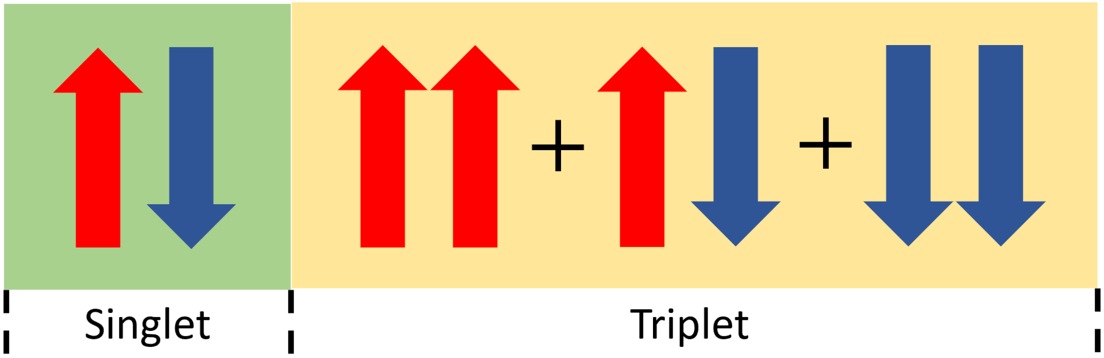

Figure 3.1. Configuration of the Cooper pairs of spin-singlet and spin-triplet superconductivity

magnetic moment into the system. At the same time, Anwar[85] also discovered a 700-nm long-range proximity effect in CrO_2 with MoGe electrodes. Later, they inserted a very thin layer of Ni between CrO_2 and MoGe, which greatly enhanced the critical current of the device. Apart from these direct evidences, there are different ways of proving the existence of spin-triplet Cooper pairs, like weak-link Josephson junction, spin-triplet spin valves. The following sections will introduce the works we have done related to the spin-triplet superconductivity devices.

3.1.2 Josephson Junctions

The spin-triplet superconductivity can be detected by fabricating Josephson junctions. Ryazanov[86] studied Nb/$Cu_{1-x}Ni_x$/Nb Josephson junctions and found out the critical current was oscillating with the thickness of F material. Khaire[87] build up a Co-based Josephson junction and observed spin-triplet superconductivity. This heterostructure is based on S/F'/N/SAF(synthetic antiferromagnet consist of (Co/Ru/Co)/N/F"/S) structure. Here F' and F" are weak magnetic materials like PdNi or CuNi. They found that the critical currents I_C decayed much slower when there were F' and F" layers inserted into the heterostructure, which created an inhomogeneous magnetic moment in the system. Volkov[88] gave a theoretical explanation for this work. At the same year, Robinson JWA[89] was using holmium metal, which has a spiral magnetization crystal structure, as a source of inhomogeneous moment to create a sample with stack S/Ho/F/Ho/S, with Co as F layer. They found out that supercurrent sustained with the increase of Co thickness when there are Ho interlayers. Particularly, they found that the thickness of Ho plays an important role in this process, which might be owing to a certain spiral structure that rotates the spins.

3.1.3 Spin-triplet Superconducting Spin Valve

Apart from the experimental evidences mentioned above, superconducting spin-valve is also a suitable device for measuring spin-triplet superconducting. A brief configuration of superconducting spin-valve is shown in Figure 3.2. Here F is the fixed magnetic layer which is hard to rotate under the external field, F' is the free magnetic layer which is susceptible to the external field, and S is superconducting layer which provides spin-singlet Cooper pairs. The β is defined as the angle between the orientations of the two magnetic layers. As shown in Figure 3.2, penetration of spin-singlet Cooper pairs from S to F materials will result in a mixing of the spin-singlet and spin-triplet components of the condensate when there are more than one magnetic orientation presenting. In other words, the spin-triplet Cooper pairs can only exist when two magnetic layers are in non-colinear configuration. Studies[90, 91, 92, 93, 94] showed more evidences of spin-triplet superconductivity in a S/F/F' superconducting spin-valve heterostructures. Via controlling the relative orientation of two magnetic layers in the superconducting spin-valves from non-linear magnetic state to either antiparallel or parallel state, the T_C changes with the magnetization angle, which gives a strong evidence for the spin-triplet superconductivity. A theoretical predictions for this phenomenon has been given by Ya. V. Fominov[92]. In summery, the generation of the spin-triplet state can be manipulated via changing the relative orientation of the magnetization, which gives potential to invent a new type of superconducting spintronics.

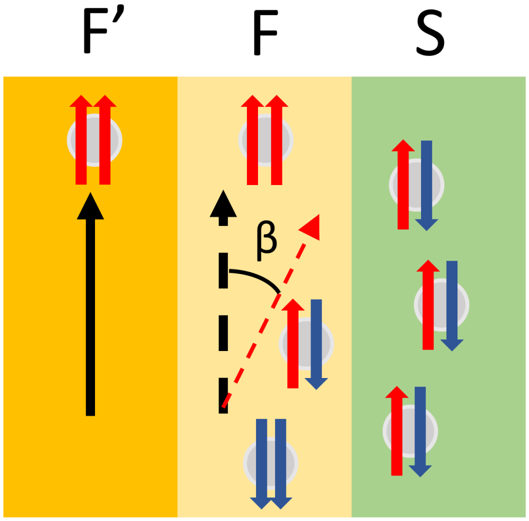

Figure 3.2. Configuration of superconducting spin-valves

3.2 Experimental Method

3.2.1 Epitaxial Growth of Ni and Co Thin Films

As shown in Figure 3.3, here we use magnetron sputtering for the epitaxial growth of Ni and Co thin films on top of single-crystalline MgO(110) substrates. Since there is a large mismatch in lattice constant between Co/Ni and the MgO substrate, a single-crystalline Cr buffer layer was deposited before the deposition of Co and Ni layer. To ensure the single-crystalline growth of Cr, the MgO substrate was preheated to 200 °C for half an hour to eliminate the moisture on the surface. The Cr buffer layer was then deposited at 200 °C at 3 mTorr processing pressure. The resulting Cr buffer layer thickness is approximately 6-nm thick for all prepared samples. After that, the substrate is cooled to room temperature for the subsequent deposition of the remaining layers.

3.2.2 Angle Dependent VSM and Transport Measurements

The vibrating sample magnetometry (VSM) measurements were carried out in a Versalab system with different applied field angles respect to the easy and hard axis of the MgO(110) substrate as shown in Figure 3.3. The samples were mounted and wire-bonded on the PCB

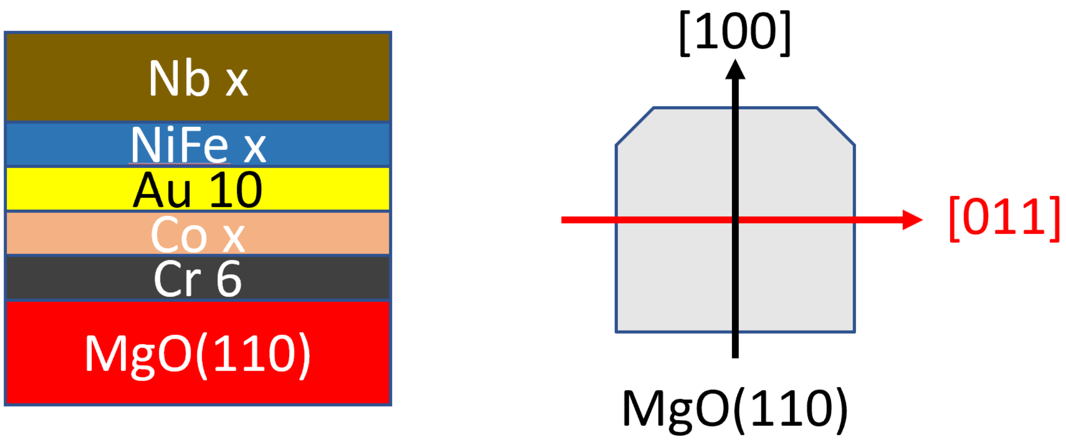

Figure 3.3. Heterostructure of superconducting spin-valve and configuration of the MgO(110) substrate

for the 4-wires transport measurements in PPMS to achieve low temperature and high field environment. The samples were measured around the superconducting critical temperature under external magnetic fields, and then repeat the same measurement after rotating 90 °to change the orientation of the free magnetic layer. During the measurement, the angle between easy axis of Co/Ni hard layer and external magnetic field is defined as β. For Co sample, when field is applied to MgO[001] and MgO[110] direction, $\beta = 0$ and 90°, respectively. This is opposite in Ni samples, when field is applied to MgO[001] and MgO[110] direction, $\beta = 90°$and 0, respectively.

3.2.3 Polarized Beam Relectometry

The samples were sent to the NIST for the polarized beam relectrometry (PBR) measurements. The PBR used cold neutron to study the surface and interfacial science of materials, including magnetic multilayers, polymer films, and artificial biological membranes. One of the most frequently used application of PBR is the specular neutron relectometry, which is sensitive to the depth profile of the nuclear composition and the vector magnetization in thin films and multilyaers. The spin polarized neutron beam allows for clear distinction between magnetic and structural contributions to the scattering. Cryostats, magnets, and liquid cells are available for control of sample environment. In our experiments, the samples were put into a cryostats and a

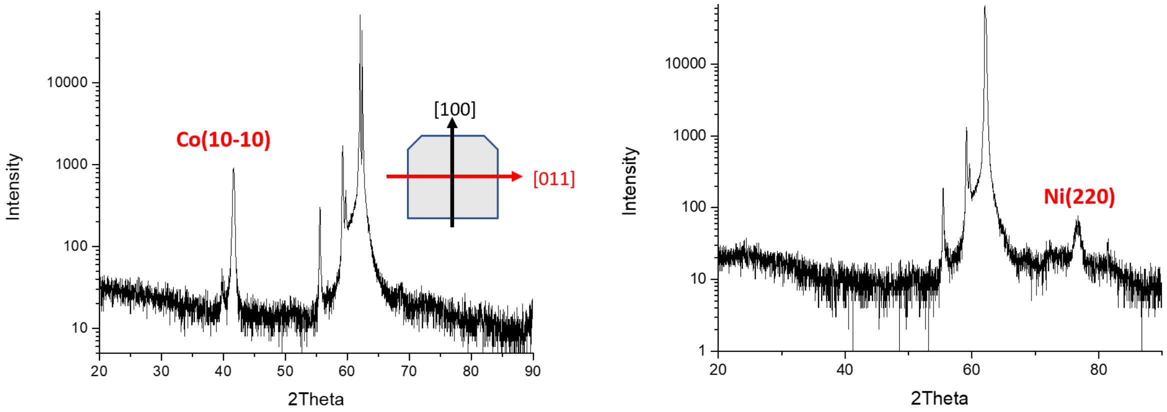

MgO(110)/Cr(211)/Co(10-10)

MgO(110)/Cr(211)/Ni(220)

Figure 3.4. XRD characterizations for the epitaxial growth of Co an Ni thin film on MgO(110) substrate

field is applied to the in-plane direction of the multilayers at different angles with respect to the hard axis of the Co layer. The NiFe free layer will always aligned to the direction of the external field, which can switch the superconducting spin valves between co-linear and non-co-linear state and thus control the generation of the spin-triplet Cooper pair. The magnetic orientations of two the magnetic layers were analyzed by fitting the resulting PBR data from different polarized neutron beams.

3.3 Results and Discussion

3.3.1 XRD and VSM Characterizations for Epitaxial Single Magnetic layer

To confirm the epitaxial growth of Co and Ni thin films, XRD characterizations were carried on the deposited samples. As shown in Figure 3.4, for the Co sample, excluding the high intensity peak around 2θ = 55-65°from the MgO(110) substrate, there was only one detectable Co(10-10) peak around 2θ = 41°, which indicates the good quality of the epitaxial growth of the hcp Co films with easy axis (c-axis) in the film plane. A similar situation can be observed in the XRD for the Ni thin film sample where there was only one observable Ni(220) around 2θ = 76°, indicates good quality of the epitaxial growth of the fcc Ni films.

Due to the uniaxial crystal structure of Co(10-10) and Ni(220), the magnetic layer exhibited in-plane easy and hard axes along two different directions normal to each other. It is known that the easy axis of hcp Co and fcc Ni are along [0001] and [110] directions, respectively. Their hard axes are along [1-100] and [100] directions, respectively. However, it is hard to determine the angle difference of crystal structure between MgO(110) substrate and epitaxial growth Co and Ni, which is essential for the determination of their magnetic easy and hard axes. This can be shown in Figure 3.5(a) that depends on the angle difference, we can observe different magnetic behaviors of the grown magnetic layers along MgO[100] direction and MgO[110] direction. To confirm the angle difference between MgO substrate and grown epitaxial magnetic thin film, VSM technique was used to measure the magnetic hysteresis loops along MgO[100] direction and MgO[110] direction for the NiFe thin film, the hcp Co thin film, and the fcc Ni thin film. Figures 3.5(b),(c), and (d) show the VSM results when magnetic fields were applied along MgO[100] direction (black curves), MgO[111] direction (blue curve), and MgO[110] direction (red curves) for a single layer of NiFe thin film, Co thin film, and Ni thin film, respectively. We can clearly observe that the in-plane easy axes for NiFe, Co, and Ni thin films were along the directions of MgO[100], MgO[100], and MgO[110], respectively. Similarly, the hard axes are along the direction of MgO[110], MgO[110], and MgO[100], respectively. Apart from that, the coercive field along hard axis of NiFe thin film was much smaller than the Co and Ni thin films, which allows us to manipulate the magnetic orientation of the NiFe layer without affecting the magnetic orientation of Co or Ni hard layer via applying a proper strength of external magnetic field. As a result, the Co and Ni layers were used as the hard magnetic layer and NiFe layer was used as the soft magnetic layer in our superconducting spin-valves.

3.3.2 Critical Temperatures of the Reference Samples at Different Angles

To eliminate possible artifacts' signals that might not origin from the spin-triplet spin-valve effect, the superconducting critical temperatures of the reference samples were measured

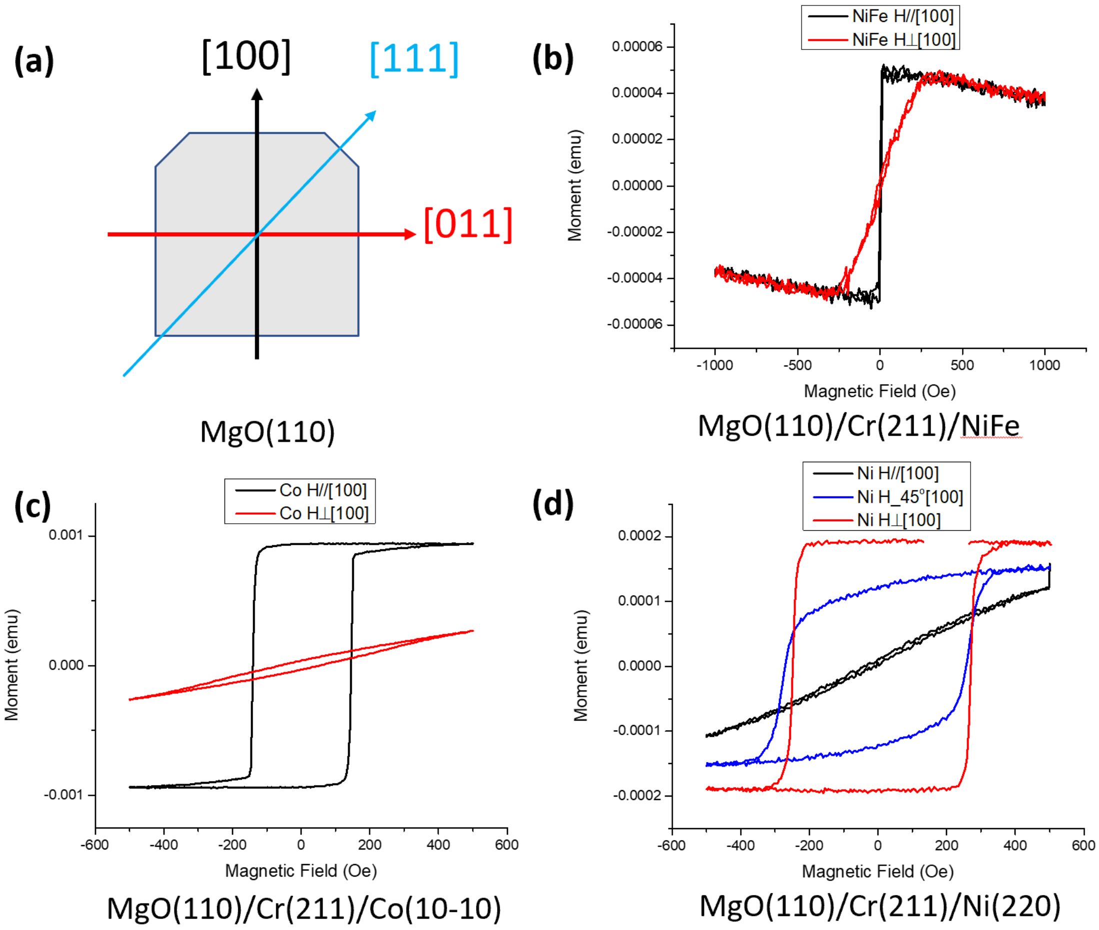

Figure 3.5. (a) Crystallography of MgO(110) substrate. Magnetic fields are applied along [100], [111], and [110] directions during the VSM measurements. (b) VSM curves along different external magnetic field directions for a single layer of NiFe epitaxial thin film, (c) for a single layer of Co epitaxial thin film sample, and (d) for a single layer of Ni epitaxial thin film.

at different external magnetic field intensity and angles. As shown in Figure 3.6(a), the reference sample with only a layer of Nb showed no change of T_C when fields were applied either along MgO[100] or MgO[110] direction, no matter what strength of field was applied. The same behavior can be observed in the reference sample which contains a single epitaxial Co layer with a Nb layer on the top as shown in Figure 3.6(b). The reference sample with a single layer of NiFe and a Nb layer on top showed a small positive change (higher T_C at 90°) of T_C at different field angle below 2000 Oe of external field but this effect disappeared at higher field region where we commonly used for measuring the spin-triplet spin-valve effect. All these results from the reference samples eliminate the possible artifacts' signal that might not come from the superconducting spin-valve effect.

3.3.3 VSM and GMR of Co-based Superconducting Spin-valves

To confirm the magnetic switching behavior of the fabricated superconducting spin-valves, VSM characterizations and gaint magnetoresistance (GMR) effects of Co-based superconducting spin-valves are measured at 100 K and 10 K respectively. Two samples with different thickness (in nm) of NiFe layer of structures: 1) MgO(110) /Cr(6) /Co(2.5) /Au(4) /NiFe(0.6) /Nb(21) /Au(4) as shown in Figure 3.7(a) and 2) MgO(110) /Cr(6) /Co(2.5) /Au(4) /NiFe(3) /Nb(21) /Au(4) as shown in Figure 3.8(a), are fabricated and mounted for VSM measurements and GMR transport measurements. As shown in Figure 3.7(b) and Figure 3.8(b), the VSM curves for both two samples showed two distinctive magnetic transition when field is applied at $\beta = 0°$. The first transition near zero field comes from the switching of NiFe soft layer and the second transition around 250 Oe comes from the switching of Co hard layer. The absolute value of the moment of the first transition is proportional to the thickness of the NiFe layer. When $\beta = 90°$, the VSM for both samples shows no saturation even at 1000 Oe, due to the coercive field along the hard axis of the Co. Notice the saturation at low field region is caused by the NiFe soft layer, which only exhibit a coercive field up to 300 Oe.

To further investigate the relative magnetic orientations of two layers at lower temperature,

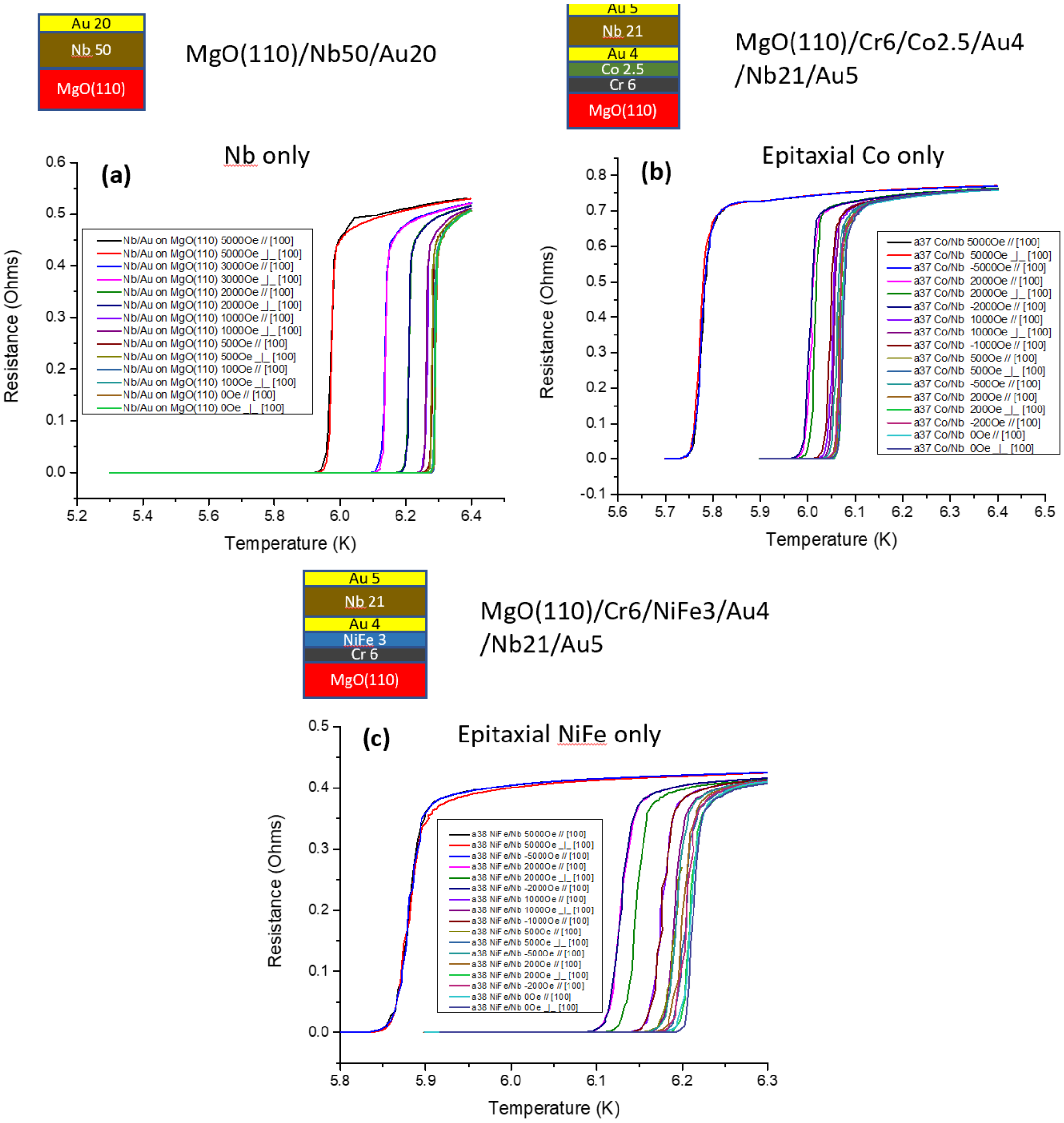

Figure 3.6. Transport measurements for the reference samples with (a) a single Nb layer, (b) a single epitaxial Co layer with a Nb layer, and (c) a single epitaxial NiFe layer with a Nb layer.

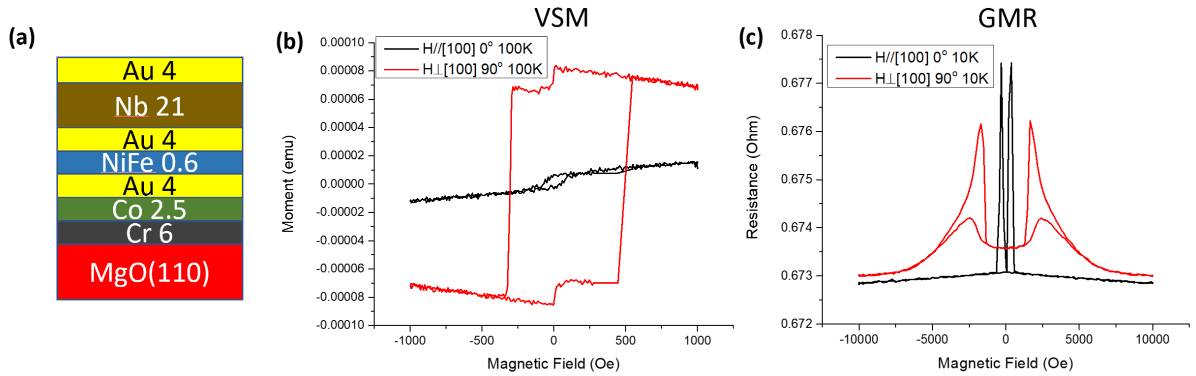

Figure 3.7. (a) Multilayer configuration of the Co-based sample with d(NiFe) = 0.6 nm. (b) VSM curves measured at 100 K at $\beta = 0°$and 90°and (c) their corresponding GMR curves measured at 10 K.

GMR transport measurements were carried on these two sample at 10 K as shown in Figure 3.7(c) and Figure 3.8(c). The GMR effect is directly related to the angle between the magnetic orientations of two magnetic layers. The change of resistance is proportional to the $sin(\beta/2)$. In this case, the maximum resistance state will show up at antiparallel magnetic orientations where $\beta = 180°$, and will switch to the minimum resistance state when magnetic orientations are in parallel where $\beta = 0°$. When they are not in co-linear state, the resistance should fall into a value in between. For both samples, the GMR effects were similar to each other when field was applied along the easy axis of the Co thin film where $\beta = 0°$or 180°. However, when field was applied along the hard axis of Co thin film, the resistance of the samples abruptly jumped up and then slowly decreased to the same resistance at the parallel state. This GMR behavior indicates the sample will not saturate along hard axis until 10 kOe due to the strong anisotropy field. A proper field to create a non-co-linear magnetic configuration should be picked up between the field at the jump of resistance and saturation field.

3.3.4 Detection of Magnetic Orientations via PBR

To confirm the magnetic orientations of the two magnetic layers at different field strength and angles, these two samples were sent to NIST for the PBR measurements at 4 K. As shown in Figure 3.9, the sample 1) was measured at three different conditions to achieve three different

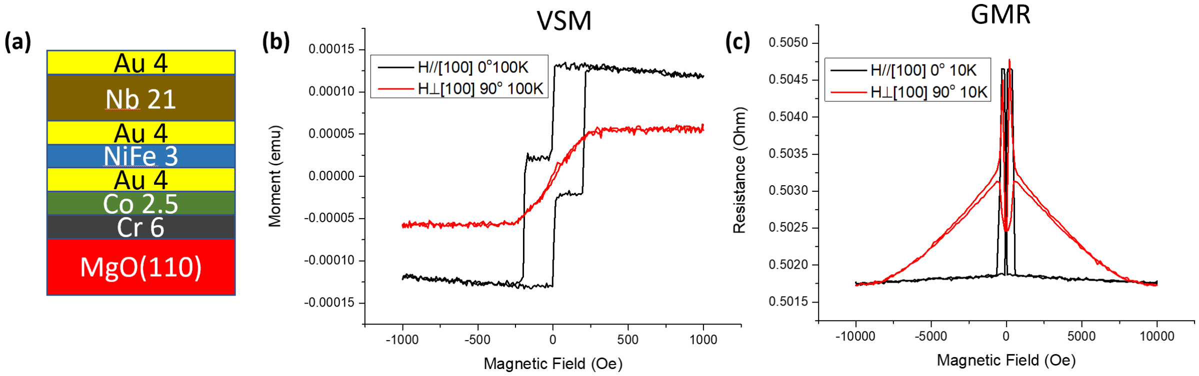

Figure 3.8. (a) Multilayer configuration of the Co-based sample with d(NiFe) = 3 nm. (b) VSM curves measured at 100 K at $\beta = 0°$and 90°and (c) their corresponding GMR curves measured at 10 K.

magnetic orientation configuration: a) $\beta = 0°$: H = 5000 Oe and field applied along MgO[100] direction; b) $\beta = 180°$: H = -200 Oe and field applied along minus MgO[100] direction; c) $\beta = 90°$: H = 3000 Oe and field applied along MgO[110] direction. The same PBR experiments were carried on the sample 2) as shown in Figure 3.10: a) $\beta = 0°$: H = 5000 Oe and field applied along MgO[100] direction; b) $\beta = 180°$: H = -200 Oe and field applied along minus MgO[100] direction; c) $\beta = 90°$: H = 2200 Oe and field applied along MgO[110] direction. In each different condition, the image on the top of the figure showing the field condition and the relative orientation of two magnetic layers. The resulting PBR data (denoted as cross points) on two opposite polarized neutron beam (++ and - -, without spin-flip) and the fitting data (denoted as solid line) are shown in the middle and in the bottom of the figures, respectively. From the PBR results, we can fit out the angles β between two magnetic orientations and the extracted the angle of Co hard layer β(F), the angle of the NiFe soft layer β(F'), and their difference $\beta = |\beta(F) - \beta(F')|$ are listed in Table 3.1. We can clearly see that the relative angle between two layers are consistent with the data we get from VSM and GMR measurements. Notice the angle difference between two layers was not exactly 90°when field applied perpendicular to the easy axis. This is due to a small degree of rotation of hard layer under this field strength, which reduces the value of β.

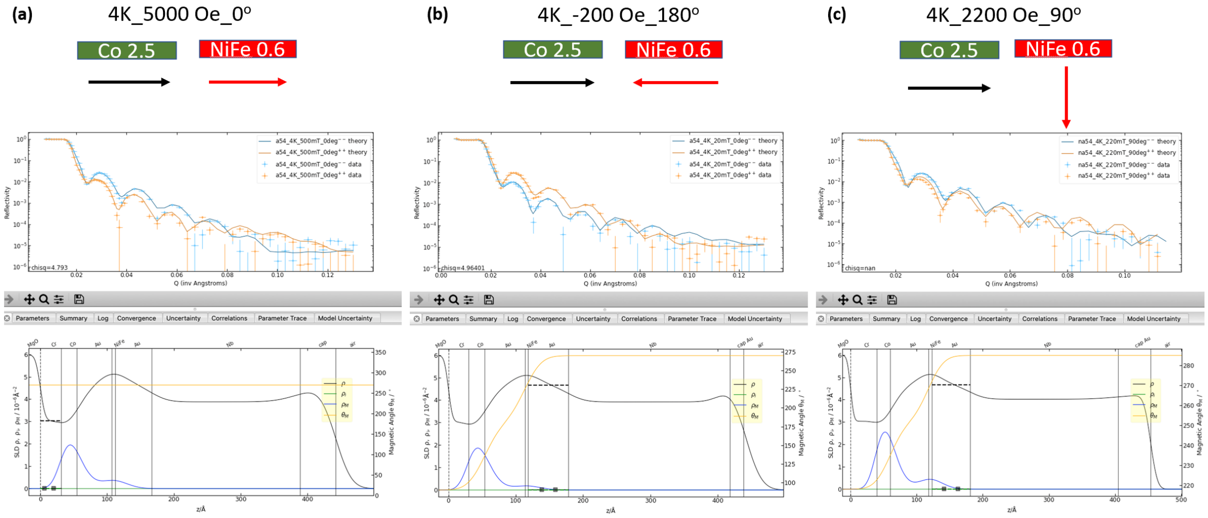

Figure 3.9. Low temperature PBR experiments for sample 1) at (a) H = 5000 Oe and $\beta = 0°$, (b) H = -2000 Oe and $\beta = 180°$, and (c) H = 2200 Oe and $\beta = 90°$

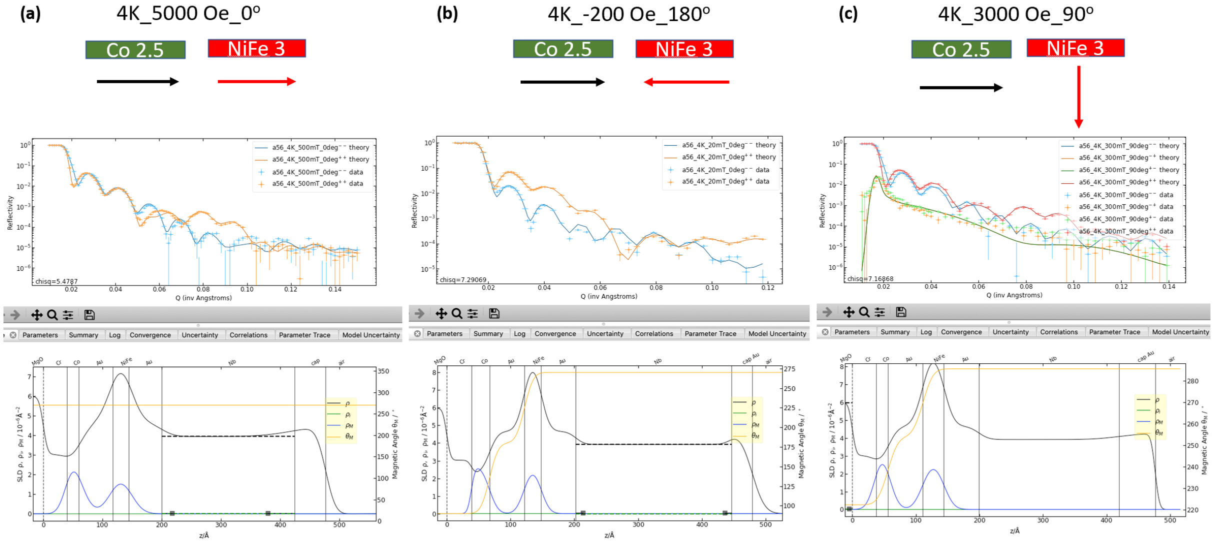

Figure 3.10. Low temperature PBR experiments for sample 2) at (a) H = 5000 Oe and $\beta = 0°$, (b) H = -2000 Oe and $\beta = 180°$, and (c) H = 3000 Oe and $\beta = 90°$

Table 3.1. Fitted magnetic orientations from PBR experiments

Sample	H (Oe)	Field Direction	β(F) (°)	β(F') (°)	β (°)
1)	5000	MgO[100]	0	0	0
1)	-200	MgO[100]	90	270	180
1)	2200	MgO[110]	220	285	65
2)	5000	MgO[100]	0	0	0
2)	-200	MgO[100]	100	275	175
2)	3000	MgO[110]	220	285	65

3.3.5 Change of Superconducting Critical Temperatures in Superconducting Spin-valves

Now we start to look into the change of T_C at different applied field angles and strengths. In these superconducting spin-valves, we measured T_C at non-co-linear magnetic configuration when β = 90°(denoted as $T_C(90)$) and T_C at co-linear magnetic configuration when β = 0°(denoted as $T_C(0)$). The β is the angle between the magnetic orientation of F layer and F' layer. The $\Delta T_C = T_C(90) - T_C(0)$ is the change of T_C at two distinctive states, which usually holds a negative value for spin-triplet spin valves. Here in Figure 3.11, we are showing the results for the Co-based sample 1) and 2) as we mentioned above. As shown in Figure 3.11(a), the sample 1), where d(NiFe) = 0.6 nm, ΔT_C showed a negative value above 2000 Oe, corresponding to the non-co-linear state shown by the GMR curve in Figure 3.7. This negative change of ΔT_C is similar to what we expected in spin-triplet spin-valves. However, as we can see in Figure 3.11, in the sample 2), where d(NiFe) = 3 nm, the sign of ΔT_C changed to positive, which means the T_C is higher at non-co-linear state. This effect is opposite to what we observed in sample 1), indicates the ΔT_C is highly sensitive to the thickness of NiFe layer. The positive value of ΔT_C at field below 2000 Oe might be caused by the epitaxial growth of NiFe thin film as shown in Figure 3.6(c), but this positive value disappeared once the field is above 2000 Oe, which cannot explain the larger $|\Delta T_C|$ value at 5000 Oe. A list of samples with different thickness of F, F', and S layers are shown and discussed in the later section.

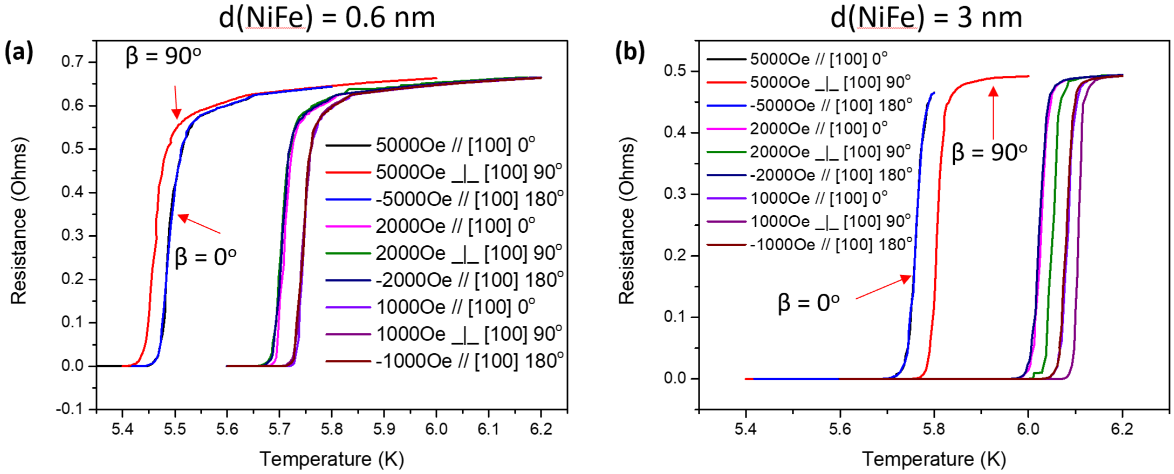

Figure 3.11. T_C of the samples with (a) d(NiFe)=0.6 nm and (b) d(NiFe)=3 nm at different β and field strength.

3.3.6 Thickness Dependence of the Change of Critical Temperature

From what we discussed above, the ΔT_C is highly sensitive to the thickness of the NiFe layer. To study the thickness dependence of the change of ΔT_C at different magnetic orientation, we fabricated multiple samples with different thickness of F, F' and S layer. In our experiments, the thickness dependence of the sign of ΔT_C are listed in Table 3.2 for Co-based samples and in Table 3.3 for Ni-based samples. We can observe that the sign of ΔT_C is not only sensitive to the thickness of F' but also sensitive to the thickness of F and S layers, independent of which epitaxial magnetic thin film was used for the hard layer. From these results, we found that most of the samples are showing positive ΔT_C, while some samples with some specific ratio of thickness of F, F', and S layers are showing negative ΔT_C. This might be caused by the corresponding change of wave function of the Cooper pairs when they are penetrating through the magnetic layers. Following up works are required to clearly identify the physics of spin-triplet superconductivity in these sample.

Table 3.2. The thickness dependent behavior of ΔT_C in Co-based superconducting spin-valves (thickness in nm)

Sample	d(Co)	d(NiFe)	d(Nb)	ΔT_C	VSM Transition
a39	2.5	0.6	15	Slightly Positive	2 steps
a26	2.5	0.6	21	Negative	2 steps
a28	2.5	3	21	Positive	2 steps
a10	2.5	1.5	50	Positive	broad
a34	5	3	15	Negative	2 steps
a33	5	0.6	21	No change	2 steps
a31	5	3	21	Positive	2 steps
a49	0	3	21	No change	2steps

Table 3.3. The thickness dependent behavior of ΔT_C in Ni-based superconducting spin-valves (thickness in nm)

Sample	d(Ni)	d(NiFe)	d(Nb)	ΔT_C	VSM Transition
b11	2.5	1.5	50	No change	2 steps
b19	5	0.6	21	Negative	2 steps
b20	5	1.2	21	Positive	2 steps
b25	5	1.8	21	No change	2 steps
b21	5	3	21	Positive	2 steps
b22	5	3	15	Slightly Negative	2 steps

3.4 Conclusion

In conclusion, we demonstrated a method to fabricate epitaxial growth of superconducting spin-valve structures. The epitaxial Co and Ni thin films were deposited onto single-crystalline MgO(110) substrates at high temperature. The crystallinity and their growth direction are characterized by XRD and VSM technique. In these epitaxial magetic thin films, they exhibit in-plane easy and hard axis along two normal directions, which can be used to manipulate the magnetic state in the spin-valves. The samples were then characterized by PBR technique to confirm the magnetic orientations of the magnetic layers. In our experiments, multiple samples with different combination of thickness of different layers were deposited. We found that the resulting change of T_C at different field angle were highly sensitive to the thickness of the magnetic layers and superconductor layer. Some of the device obeyed the expected behavior in spin-triplet spin-valves but some of them showed opposite trend. This phenomenon might be caused by a combination of spin-triplet spin-valve effect and other superconducting effects. Further studies are required to understand the physics underneath.

Chapter 4

Ion beam etching dependence of spin-orbit torque memory devices with low switching current density enhanced by Hf interlayers

Reliably fabricating nano-scale spin orbit torque switching devices has proven difficult. Here we report the fabrication of a nano-sized, three terminal in-plane spin orbit torque switching devices by ion beam etching which display low switching current density. The angle and time of etching has been systematically studied to avoid undesired defects in the magnetic tunnel junctions and the bottom spin current bridges. The switching behavior of the fabricated junctions are significantly affected by their aspect ratios and allow optimizing the shape of nanopillars. Further, Hf interlayer and dusting layer at interfaces improved the spin-orbit-torque induced switching process. Micromagnetic simulations prove the additional interfacial perpendicular anisotropy introduced by Hf interlayers lower the switching current density.

4.1 Introduction

Spin transfer torque (STT) magnetic random access memory (MRAM) is emerging as a fast and low-error non-volatile memory.[95, 96, 97, 98] However, for faster switching well below 10 ns, STT-MRAM has challenges to both avoid premature breakdown of the thin tunnel barrier Also, a two-terminal tunnel junction based STT-MRAM cell forces compromises in design between read and write circuits. A three-terminal spin-orbit-torque (SOT)- based memory cell separates the write and read operations It has been proposed for further improvements of MRAM performance metrics[99]5, enabling wider applications. In such a SOT-based 3-terminal memory device, the magnetic tunnel junction (MTJ) can be independently optimized for read circuit, while no current will pass through the MTJ for writing.

Researchers have succeeded in using SOT to switch magnetic layers and MTJs in different ways[99, 100, 101, 102, 103, 104, 105, 106, 107, 108]. Among these methods, a moment in-plane SOT switching device is one of the simpler structure to implement.[99, 101, 109] But since it relies on shape-anisotropy for bit-state stability, it requires additional care in fabrication to ensure shape fidelity. There are also some common issues for the SOT-MRAM formed using ion-beam etching (IBE) processes, including MTJ shorting due to sidewall redeposition as well as ‘big foot’ and ‘trench’ defects around the base of the MTJs. Here we demonstrate a fabrication process flow[99, 106] that focusing on the IBE angles and time and their impacts on the magnetic behavior of the MTJs. After optimizing the IBE conditions, MTJs with different aspect ratios were successfully fabricated and illustrated different SOT-induced switching behaviors enabling optimization of future memory devices. We further inserted dusting and spacer Hf layers in our MTJs, which simultaneously greatly enhances the interfacial magnetic anisotropy and suppresses the interfacial spin-memory loss.[109, 101] This significantly enhances the thermal stability and reduces the switching current density of our devices.

4.2 Experimental Methods

4.2.1 Heterostructure Composition

Multilayers from which the SOT devices were fabricated were deposited using magnetron sputtering on 8” thermally-oxidized Si wafers with the following composition as shown in Figure 4.1: (1) β-W(4nm) /CoFeB(1.8nm) /MgO(1.6nm) /CoFeB(4nm) /Ta(5nm) /Ru(5nm) and (2) β-W(4nm) /Hf(0.25nm) /CoFeB(1.8nm) /Hf(0.1nm) / MgO(1.6nm) /CoFeB(4nm) / Ta(5nm)/

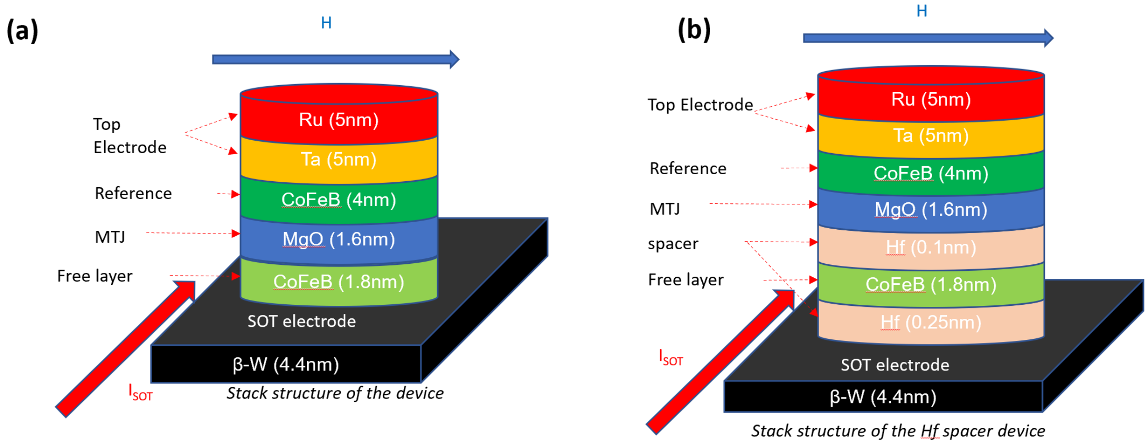

Figure 4.1. Configuration for heterostructure (a)β-W(4nm) /CoFeB(1.8nm) /MgO(1.6nm) /CoFeB(4nm) /Ta(5nm) /Ru(5nm) and (b)β-W(4nm) /Hf(0.25nm) /CoFeB(1.8nm) /Hf(0.1nm) /MgO(1.6nm) / CoFeB(4nm) /Ta(5nm) /Ru(5nm)

Ru(5nm). β-W was used to generate the SOT spin currents as it is known to have a large negative spin Hall angle.[110] The samples were annealed at 300 °C for 1 hour under an external magnetic field to get a preferential magnetization direction along the in-plane long axis of elliptical nanopillar.

4.2.2 Magneto Tunnel Junction and Contacts Fabrication

The elliptical nanopillars, bottom W bridge channel, and contacts (shown schematically in Figure 1.1(a)) are defined by e-beam lithography (EBL), followed by ion-beam etching (IBE) at 500-V beam voltage and 200-mA beam current with varying etch angles. The etching time is controlled through secondary ion mass spectrometry (SIMS). Shunt effects were avoided through in-situ SiN deposition immediately after the IBE process. These nanostructures were characterized using atomic force microscopy (AFM) and scanning electron microscopy (SEM). One resulting 30 nm × 200 nm device is shown in Figure 1.1(b). The details about fabrication will be discussed in later sections.

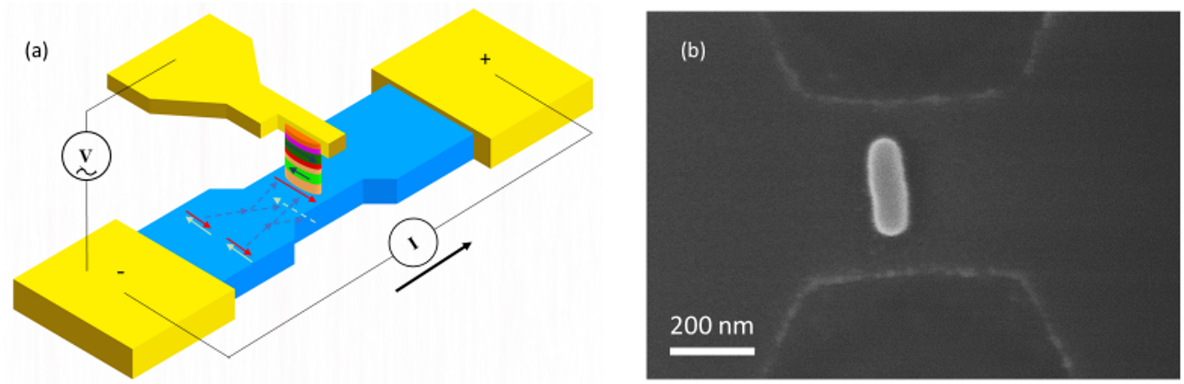

Figure 4.2. (a) Schematic configuration of designed MTJ multilayer cell and dumbbell-shape bottom β-W SOT bridge. (b) SEM image of the fabricated 30 nm × 200 nm elliptical MTJ cell above the patterned β-W layer before top lead deposition.

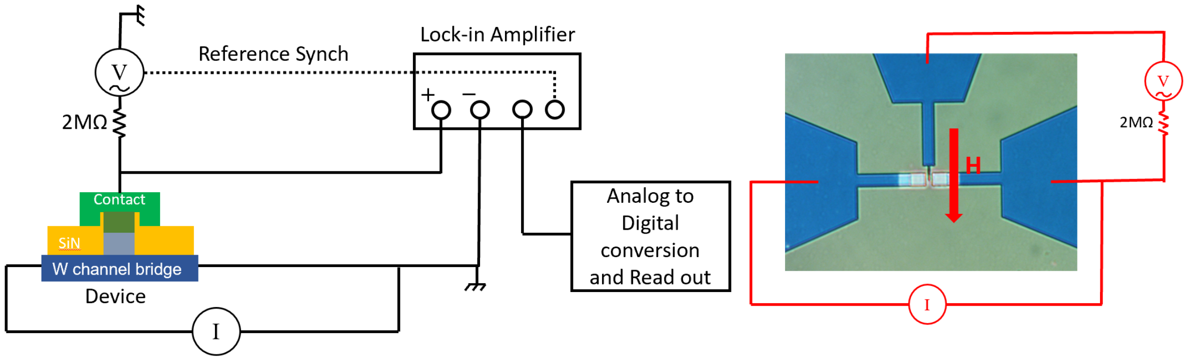

Figure 4.3. Configuration of transport measurement setup for 3-terminal SOT-MRAM device

4.2.3 3-terminal Transport Measurement Setup

A brief configuration of transport measurements setup is shown in Figure 4.3 Transport measurements were made using a probe station with an adjustable in-plane electromagnet. A three terminal configuration is used for our devices, which allows different current paths for reading and writing. An AC current source is coupled with a lock-in amplifier and connected between the top contact with one of the contact pads on the bottom W bridge for tunneling magnetoresistance (TMR) measurement of fabricated MTJs. A DC bias current source is connected to the β-W bridge for the spin Hall current generation.

4.3 Results and Discussion

4.3.1 Device Configuration and Fabrication Process Flow

The direction of spin current at the β-W/CoFeB interface induced by the spin Hall effect (SHE) is known to be in-plane and perpendicular to the direction of charge current. The elliptical nanopillar has its long axis perpendicular to the bottom current bridge as shown in Figure 4.2(a). To increase the spin current density, the β-W layer is patterned into a dumbbell shape with a narrow 500-nm width channel in the middle and two large pads on either end to reduce the total resistance of the β-W layer. Figure 4.2(b) shows a defined elliptical MTJ and the dumbbell shape β-W bridge. Finding the endpoint of IBE etching of β-W layer is critical for SOT-MRAMs which requires a stronger β-W signal in SIMS. To achieve a stronger β-W signal, elliptical MTJs are patterned first and then dumbbell shape β-W bridges are patterened.. In this case, a stronger β-W signal allows us have a more precise controlling of thickness of the bottom β-W bridge. The detailed process flow for the patterning of the full film wafer is as follows: 1) Spin coat OmniCoat (40 nm) / 2% or 6% HSQ (40-100nm)/PMMA (80-160nm) and expose the elliptical pattern of the nanopillars by EBL. 2) Develop and then pattern transferred by RIE oxygen plasma descum. 3) Etch the multilayer stack, stopping at the W layer by using IBE-SIMS. 4) Deposit a 10-nm SiN layer at 45 ° to avoid shunts. 5) Lift off any remaining resist. 6) Spin coat the same HSQ/PMMA double layer and expose through EBL to define the dumbbell shape of the W bridge. 7) Etch through the SiN insulating layer and the W bottom layer by IBE-SIMS until the substrate is reached. 8) Lift off and clean the sample surface. 9) EBL process to expose patterns for the capping electrode on the nanopillar and the SOT electrodes on the W bridge. 10) Deposit Ta/Ru and lift off, resulting in the final three-terminal devices.

4.3.2 IBE Angle Effects

IBE has been extensively used in the fabrication of STT- and SOT-MRAM devices.[111, 112, 113, 114] In our study, the critical process for SOT-MRAM device fabrication is using IBE

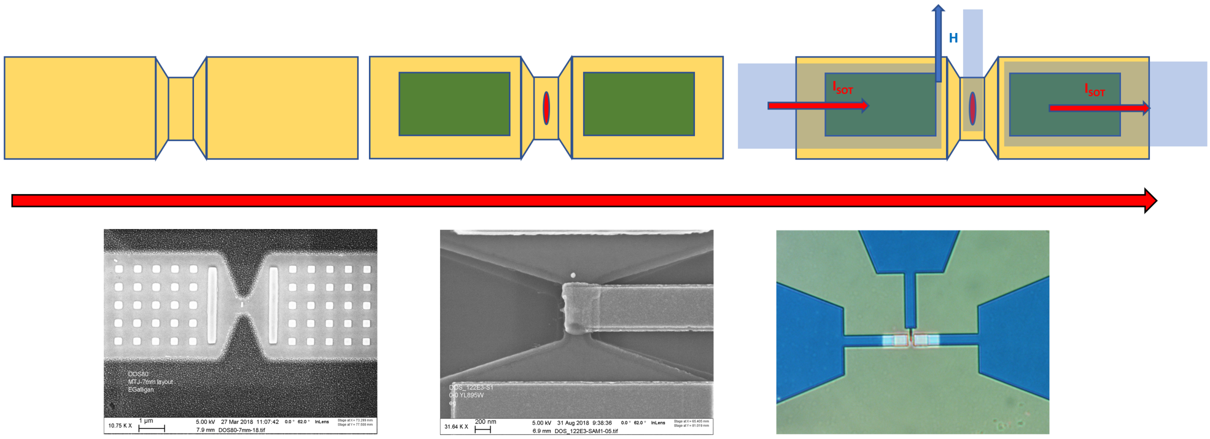

Figure 4.4. Fabrication process flow from multilayers to single device

to define the elliptical MTJs and the dumbbell shape spin current channels underneath. The most common issue in fabrication of STT- and SOT-MRAM devices is the barrier-short effect caused by the re-deposition effect during the IBE process, which will lead to a shunting of the current and low TMR values or even shunt the MTJs. In addition ‘trench’ effects arise around the base of MTJs, which is caused by reflected ions from the pillar side-wall during high-angle etching, and a “big foot” effect caused by shadowing effect from tall MTJs and photoresist are also commonly observed in IBE process.[115] It is known that the etch rate and re-deposition rate is highly dependent on etch angle.[111, 114, 116] As shown in Figure 4.5(a), we define the step angle α as the angle between side wall and substrate plane and the beam angle β as the angle between the incident ions and the normal of substrate. The sample rotates continuously during the etching process.

The most common beam angle used in STT-MRAM fabrication is $\beta = 45\,°$. At this angle, the re-deposition on the sidewall of MTJ is suppressed and a high net etching rate is achieved. However, thick photoresist (in our case OmniCoat(40nm) /6% HSQ(40-100 nm) /PMMA(80-160 nm)) will cause a ‘big foot’ effect as shown in Figure 4.5(b). The profile curve across the short axis of a nanopillar is shown in Figure 4.5(c). Subsequently, the shading effect is significant due to the tall photoresist, resulting in this large foot around the base of the MTJs. Due to the geometry of the MTJs, the big foot effect is more prominent along the short axis than along the

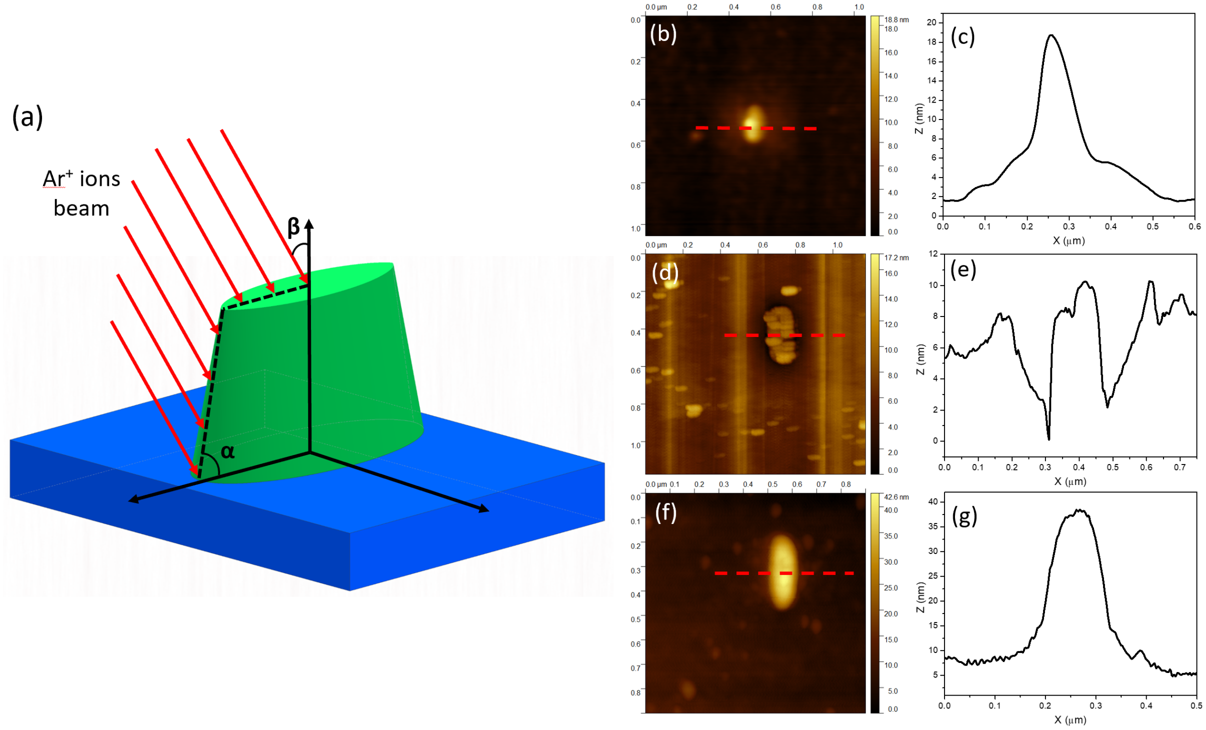

Figure 4.5. (a) IBE angle configurations where α is the step angle and β is the ion beam angle (b) AFM images of the MTJs after IBE at (b) $\beta = 45°$, (d) $\beta = 0°$, and (f) $\beta = 0°$ followed by an IBE at $\beta = 80°$. The cross-sectional profiles of AFM images for (c) $\beta = 45°$, (e) $\beta = 0°$, and (g) $\beta = 0°$ followed by an IBE at $\beta = 80°$.

long axis.

To address this problem, a low beam angle is necessary. Here we tried to etch the MTJs at $\beta = 0°$. However, a low beam angle will produce a sharp tilted sidewall and reflect ions that hit on sidewall, causing higher ion beam density near sidewall of MTJs. This will lead to a locally high etch rate around the base of MTJs and leads to a deeper cut around MTJs on β-W layer. An AFM image (Figure 4.5(d)) and profile curve (Figure 4.5(e)) clearly show trenches around the base region of the MTJs. The trenches usually do not cut through the entire β-W layer, however there is no sign of SOT switching in these devices, since the trenches dramatically reduce the spin current density that pass through the bottom of MTJs.

To make a sharp and clean junction without any defects, thinner 2% HSQ (40nm)/ PMMA (80nm) bilayer photoresist without OmniCoat was applied to get a sharper sidewall during the IBE process, which eliminates the trenches defects. Besides, two steps of IBE at different angles is introduced in our fabrication. We firstly etch at $\beta = 0$ to get a well-defined tall elliptical nanopillar structure, then followed by an 1 minute etch at $\beta = 80$ ° to clean the contaminated surface of sidewall caused by re-deposition. AFM image and cross sectional profile are shown in Figures 4.5(f) and (g), which show a well-defined elliptical shape MTJ without undesired defects.

4.3.3 IBE Time Effects

Meanwhile, controlling the etching time at $\beta = 0$ is also of great importance, since the bottom β-W layer is only approximately 4 nm in thickness that a small under-etch or over-etch will significantly devastate the performance of SOT devices. During the IBE-SIMS process, starting time t = 0 is set to when W signal emerges. A plot of the resistance of the bottom β-W dumbell bridge versus the over-etching time is shown in Figure 4.6(a). As expected, the longer the etching time, the higher the resistance of the β-W bridge. At an over-etching time of 60 seconds, the resistance is no longer measurable, though there is still a W signal from SIMS due to an uneven IBE etching. This results in a discontinuous W layer and creating individual

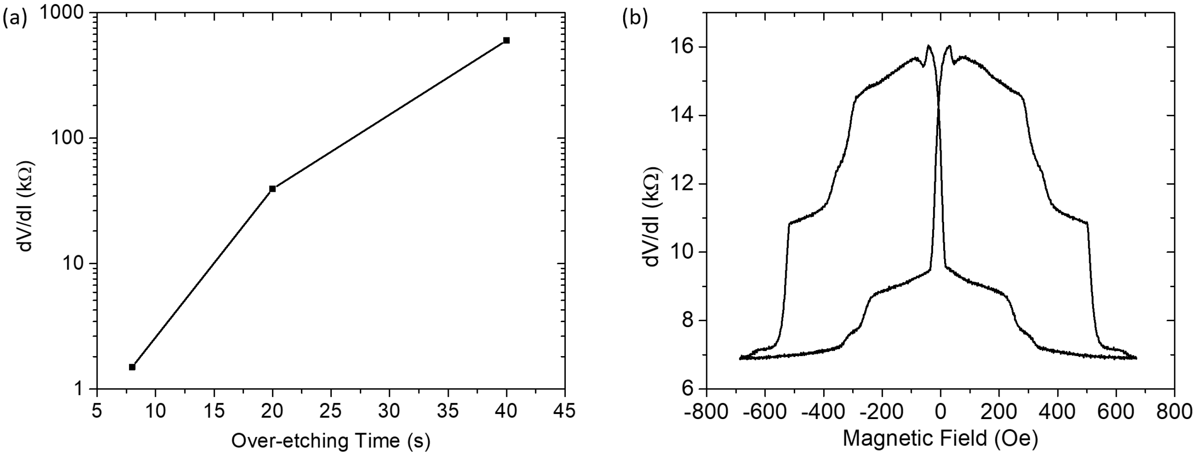

Figure 4.6. (a) β-W bridge's resistance vs. over-etching time at β = 0. (b) TMR hysteresis loop of the device with small over-etching time exhibit multiple domains switching pattern.

nano-islands. On the other side, if the etch process is stopped at time zero, there are still some residual CoFeB small islands remaining on the W bridge, which will lead to multi-domains curve in TMR hysteresis loop as shown in Figure 4.6(b). The optimal over-etching time at $\beta = 0$ for our devices ranges from 10s to 20s.

4.3.4 Spin-orbit Torque Switching in The Fabricated Single Device

Full SOT devices were fabricated by the process described above with the composition β-W(4nm)/CoFeB(1.8nm)/MgO(1.6nm)/CoFeB(4nm)/Ta(5nm)/Ru(5nm) with different elliptical dimensions. Figure 4.7(a) shows the TMR hysteresis minor loops of MTJs in different shape. A 200 Oe offset in the hysteresis loop is due to the dipole field from the top CoFeB reference layer. The TMR ratio is approximately 82.5% at zero bias DC current. According to the macrospin model in previous studies[97, 117], we define the effective anisotropic field H_{eff} that is required to overcome for switching by the spin Hall effective field. In our system, $H_{eff} = H_c + M_{eff}/2 + H_{DP} + H$, where H_c is the coercive field of the in-plane elliptical shape free layer, H_{DP} is the dipole field originate from the top reference layer and it usually being compensated by an external field H. For thin film samples, $M_{eff} \approx M_s - 2K_s/\mu_0 M_s t_M$ is the effective demagnetization field that mainly depends on the saturation magnetization M_s, the thickness of magnetic free layer t_M and perpendicular interfacial anisotropy energy K_s arising from the CoFeB-MgO interface. To simplify the transport measurements, we set $H = -H_{DP}$, then the SOT switching current density J_{c0} should follow the equation

$$J_{c0} = \frac{2e\mu_0 M_s t_M \alpha (H_c + M_{eff}/2)}{h\theta} \tag{4.1}$$

where e is the elementary electron charge, μ_0 is the permeability in vacuum, α is the damping constant of the free layer, h is the reduced Plank constant and θ is the effective spin Hall angle. For a pure CoFeB layer directly contacting with β-W layer, we have M_s = 1.2 × 10^6 A/m, α = 0.018 and measured $M_{eff} \approx$ 7.1 × 10^5 A/m from previous study[110]. From Figure 4.7(a), we could extract that $H_c \approx$ 102.5 Oe and $H_{DP} \approx$ 200 Oe. A 200 Oe bias magnetic field is added to compensate the dipole field and the resulting switching pattern shown in Figure 4.7(b). Due to the fast current ramping rate r_I = 1.2 mA/s, a good estimate of $I_{c0} \approx 1.5 I_c$ should be valid here. We observed J_c= 2.4 × 10^{11} A/m^2 and subsequently $J_{c0} \approx$ 3.6 × 10^{11} A/m^2 with the cross-section area 4 × 500 nm^2 defined by the shape of bottom β-W layer. Putting all parameters into Equation 4.1, the extracted effective spin Hall angle $\theta \approx$ -0.15, smaller than the reported values.[101, 110] This smaller spin-Hall angle might cause by a mixture of different W phases. The switching sign agrees with the negative spin Hall angle of β-W indicated the etch process and final device design are working as expected.

4.3.5 Aspect Ratio Effects on Switching Behaviors

The aspect ratio of the fabricated nanopillars is an important factor that governing the behavior of the device. Perpendicular magnetic anisotropy (PMA) SOT-MRAM devices are usually designed with round MTJs due to the desired out-of-plane magnetic anisotropy. In-plane SOT-MRAM devices require strong in-plane shape anisotropy, achieved here by shape anisotropy along the long axis of an elliptical nanopillar. The presence of magneto-crystalline anisotropy, the thickness of the magnetic layer, and the shape of the junction are important factors affecting

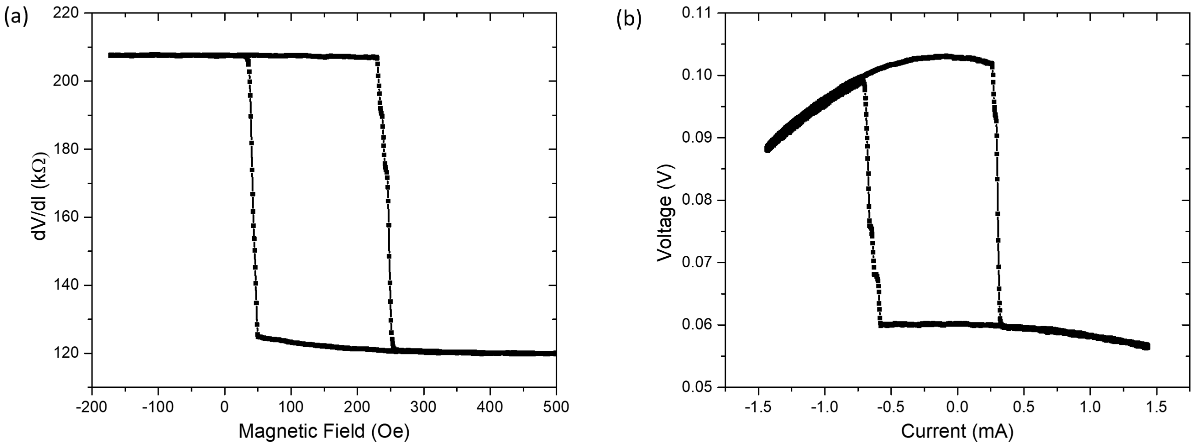

Figure 4.7. (a) The TMR magnetic hysteresis minor loop for a 40 × 150 nm^2 junction. (b) The DC bias SOT current-induced switching loop at a 200 Oe external field.

the switching current and thermal stability. Among these factors, the shape or the aspect ratio of the junctions in the easiest factor to manipulate, since the shape anisotropy is dependent on the aspect ratio of the MTJ. In order to study the effect from the shape of junction, we fabricated the MTJs into three different sizes: sample (1) 30 × 100 nm^2 and (2) 30 × 150 nm^2 with aspect ratios of (1) 1:3.3 and (2) 1:5, respectively. The higher the aspect ratio, the higher the shape anisotropy.

To fabricate devices that is applicable, the size of the MTJs should be small enough to ensure a single domain and high area density but large enough to ensure thermal stability. As shown in Figure 4.8(a), both two devices show TMR transition without loss of thermal stability. The resistances of the MTJs are inversely proportional to the designed size of nanopillars as expected. From Figure 4.8(a), the switching fields for each device are (1) 23 Oe and (2) 205 Oe, respectively. According to previous study[118], the switching fields are directly related to the aspect ratio $u = l/w$, where l and w are the long and short axis of elliptical nanopillars, and sweeping rate R_H of external magnetic field due to the thermal-assistance flipping process. The zero temperature anisotropic field for elliptical shape nanopillar is well-defined as

$$H_k = 4\pi M_s(t/w)F(u) \tag{4.2}$$

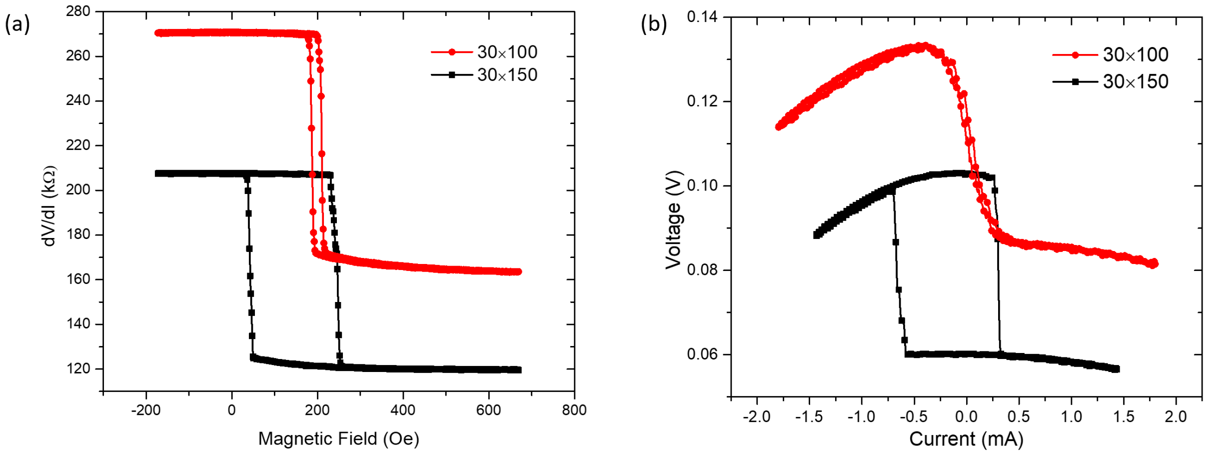

Figure 4.8. (a) In-plane field switching minor loop and (b) SOT-induced switching minor loop for the nanopillar with size 30 × 100 nm^2 (red circle) and 30 × 150 nm^2 and (black square), respectively.

where $F(u)$ is the integral of a function of u as shown in ref. [118]. The calculated H_k are (1) 718 Oe and (2) 802 Oe. However, due to the thermally assisted flipping process, the switching field H_s will be greatly reduced when barrier height is comparable to thermal energy k_BT (k_B is Boltzmann constant and T is temperature) at room temperature with small R_H. The sweeping rate R_H dependent switching field H_s then has the relation

$$R_H = \frac{\gamma_0}{2C(H_k - H_s)} e^{-C(H_k - H_s)^2} \tag{4.3}$$

where γ_0 on the order of 109 Hz is the attempting frequency and

$$C = \frac{lw^2F(u)}{32k_BT} \tag{4.4}$$

During the transport measurement R_H stays at 396 Oe/s and by solving the equation (2) numerically, we get H_s = (1) 248 Oe and (2) 398 Oe. Compared to the experimental values shown above, the calculated values showed the same trend but with higher switching field. One possible explanation is that the e-beam lithography process tends to enlarge the designed width of the elliptical shaped nanopillars due to its resolution limit. By adding 20 nm surplus to the widths of the devices, the resulting H_s become (1) 78 Oe and (2) 191 Oe, which is much closer to the measured values. Another possible explanation is that it is possible related to the thermal stability factor $\Delta = E_b/k_bT$. In our system, the energy barrier E_b is mainly coming from anisotropy energy $K_u = \mu_0 H_k M_s/2$ and thus $E_b = K_u V = K_u \pi twl/4$. This will give the thermal stability factor Δ = (1) 44 and (2) 74. If we consider the resolution of e-beam lithography, Δ further decreased to (1) 32 and (2) 63. These two values are strongly related to the switching field and we can notice that the Δ in device (1)<<(2), and $\Delta < 50$, which is a typical minimum for a stable device. This could explain why it only exhibits switching field of 25 Oe. As shown in Figure 4.8(b), the thermal-assisted SOT-induced J_c for a complete switching in each device are (1) 1.8 × 10^{11} A/m^2 and (2) 2.4 × 10^{11} A/m^2 respectively. The switching current I_c for spin-torque switching in MTJ is directly related to the thermal stability factor $\Delta = E_b/k_bT$ at ambient temperature indicated as[119, 120]

$$I_c = I_{c0}(1 - \frac{1}{\Delta} ln[\frac{1}{a_I \tau_0 \Delta} \frac{|I_{c0}|}{|r_I|} (\frac{|I_{c0}|}{|I_{c0} - I_c|})^{(a_I - 1)}]) \tag{4.5}$$

where τ_0 is the effective thermal attempt time, assumed to be 1 ns, and r_I is the current ramping rate and set to 1.2 × 10^{-3} A/s during the measurements, a_I is a constant, usually equals to 1.5. Assuming two devices has similar I_{c0} = 3.6 × 10^{11} A/m^2, by putting parameters into equation (3) and switching current measured from experimental data, we can easily get the thermal fitted stability factors Δ for two devices are (1) 33 and (2) 50. These numbers are consistent with the previous calculation results, indicating the device is rounder than the designed pattern.

4.3.6 Hf Spacers and Dusting

According to previous studies[109, 101, 121], inserting a subatomic Hf dusting layer between the MTJ barrier and the free layer, and a monoatomic Hf spacer layer between the spin current layer and the free layer can enhance the interfacial magnetic anisotropy energy (or perpendicular anisotropy) and suppresses the interfacial spin-memory loss and thus reducing

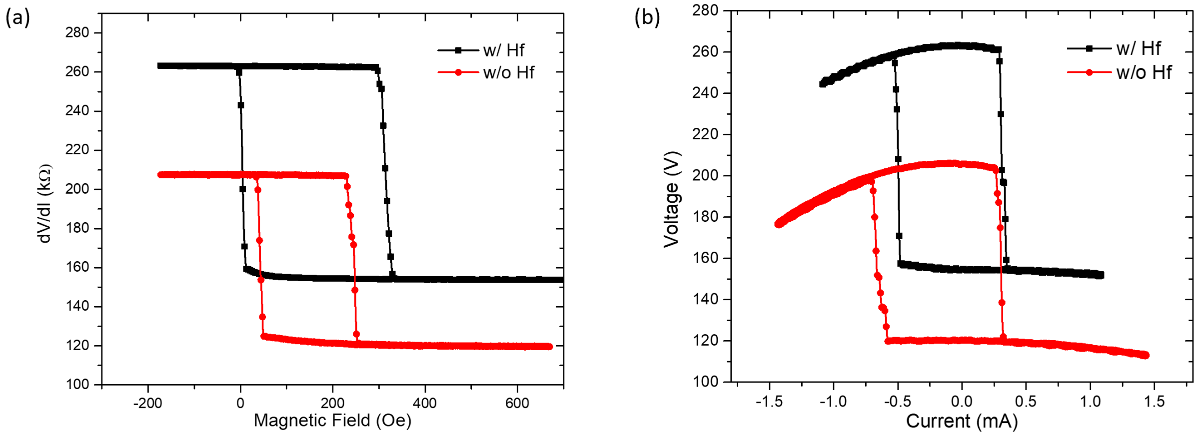

Figure 4.9. (a) Magnetic field switching loops and (b) SOT-induced switching loop in similar devices with Hf interlayers (black square) and without Hf interlayers (red circle).

the critical switching current density. We insert a 0.25 nm monoatomic Hf layer between the free layer and β-W layer, and also insert a 0.1 nm Hf dusting layer on top of the free layer as shown in Figure 4.1(a). The MTJs are patterned into elliptical 30 × 150 nm^2 nanopillars. As shown in Figure 4.9(a), the H_s of the device with Hf functional layers is 310 Oe, which is 50% greater than the device without Hf functional layer. By fitting the Equation 4.3 and 4.5, one can obtain the ratio of thermal stability factor between the device with and without Hf functional layers is $\Delta_{Hf}/\Delta = 1.17$, which means the device with Hf functional layers is more stable at room temperature. As shown in Figure 4.9(b), the measured J_c for the Hf inserted device is about 1.9×10^{11} A/m^2, which is about 79% of the J_{c0} for the device without the Hf functional layer. We attribute this reduction of J_{c0} to the lower effective demagnetization field $M_{eff} \approx M_s - 2K_s/\mu_0 M_s t_M$ due to the increase of K_s. As found in earlier work[121, 109], the subatomic Hf layer between the free layer and the MgO layer results in oxidized HfOx during the MgO deposition, which enhances the perpendicular interfacial magnetic anisotropy K_s. Apart from that, a monoatomic Hf layer between β-W and free layer leads to a decrease in the damping constant α due to the reduction of interfacial spin-memory loss will also decrease the J_{c0} accordingly[122].

4.3.7 Micromagnetic Simulation of Hf Space

To verify the assumptions, we carried out Mumax3 micromagnetic simulations on these devices.[123] The simulation grid is consist of 30 × 150 × 1 cells in elliptical shape with dimension 30 × 150 × 1.8 nm^3. The running time for each step are set to be 20 ns to ensure spins have enough time to response. All input parameters that are used in simulation come from previous result in this paper and T = 300 K. Two simulations are examined: (1) Device without Hf interlayer which has no additional perpendicular anisotropy K_s and (2) device with Hf interlayer which is added a uniaxial $K_u = K_s/t_M$ with easy axis out of the plane. Due to the very fast current density ramping rate (20 ns per 0.5 $\mathrm{A/m^2}$), we should have $J_{c0} \approx J_c$. As shown in Figure 4.10, the resulting magnetization versus spin current density for a device (1) without Hf interlayers gives J_{c0} = 6 × 10^{11} $\mathrm{A/m^2}$, slightly smaller but consistent with our experimental result. By adding a small out-of-plane K_u = 2 × 10^5 $\mathrm{J/m^3}$, which equals to a perpendicular interfacial anisotropy $K_s = K_u t_M$ = 3.6 × 10^{-4} $\mathrm{J/m^2}$, we obtained a critical switching current about J_{c0} = 5 × 10^{11} $\mathrm{A/m^2}$ for device (2) with Hf interlayers, which is consistent with the J_{c0} drop in the experimental data. The simulation tells us that a small amount of perpendicular interfacial anisotropy can easily reduce the J_{c0} in SOT-MRAMs. These results show the effectiveness of the Hf interlayer and dusting layer assist the effort of reducing critical current density.

4.4 Conclusion

In conclusion, we have demonstrated a fabrication process flow for SOT-MRAM devices and studied the impacts from IBE angles and time. By introducing multiple IBE steps with thin EBL resist layers, different elliptical shape MTJs have been fabricated without nano-architecture defects and shunts. The device without Hf interlayers inserted shows a spin Hall angle $\theta \approx$ -0.15. Devices with different aspect ratios show high TMR value and clear transitions in both field switching and SOT-induced switching hysteresis loops. Hf interlayers are also introduced to enhance the perpendicular interfacial anisotropy at the MgO/HfOx/CoFeB interface and reduce

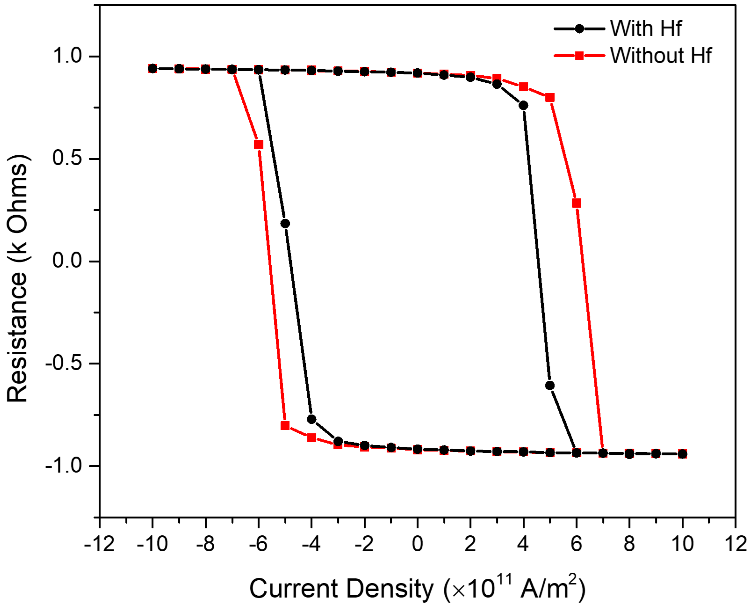

Figure 4.10. Micromagnetic simulation SOT-induced switching loop in similar devices with Hf interlayers (black square) and without Hf interlayers (red circle).

the spin-memory loss at the bottom CoFeB/Hf/β-W interface. The resulting switching current density in Hf contained device decreased to 1.9×10^{11} A/m^2, only 79% of the switching current density in the device without Hf with the same geometry. This study gives an overlook of etching process, design of nanopillar and multilayer materials design that will be helpful for the future fabrication engineering of SOT-MRAM devices.

4.5 Acknowledgement

Chapter 4, in part, is currently being prepared for submission for publication of the material "*Ion beam etching dependence of spin-orbit torque memory devices with low switching current density enhanced by Hf interlayers*", Haowen Ren, Shih-Yu Wu, Jonathan Z. Sun, Eric E. Fullerton. The dissertation author was one of the primary investigators and author of this material.

Chapter 5

Conclusion

In this dissertation we first demonstrated a new method to fabricate nano-porous composite LSCF-YSZ and LSC-GDC cathodes for the application in TF-SOFCs in the chapter 1. The XRD, EDX, and TEM characterizations shows the composition and nano-morphology of the deposited cathode and EIS analysis revealed the mechanism of these high performance cathodes. We also showed that our TF-SOFCs are hydrocarbon fuels compatible via replacing anode materials with Ru and GDC materials, which are suitable catalyst for the reforming process of hydrocarbon fuels. In chapter 2, we demonstrate the fabrication of single-crystalline Si-dope Ni nanowires via thermal CVD method. We found that the Si impurities greatly reduced the Curie temperature of the Ni nanowires and the growth mechanism gives a Si concentration gradient over the distance to the growth site of the nanowires. The anisotropic magnetoresistance were calculated by Stoner model and the AMR curves were fitted via the micromagnetic simulations. An abnormal negative resistance contribution appeared at low temperature are attributed to the domain wall magnetroresistance. At high magnetic field, we studied the magnon-electron scattering in the nanowire and the magnon stiffness constant was extracted via the transport measurements. In the chapter 3, we talked about the fabrication of superconducting spin-valves and transport measurement around the superconducting critical temperature. The epitaxial Co and Ni thin films and the superconducting spin-valve heteroustructures were grown via sputtering technique. The magnetic properties and orientations were confirmed by VSM and PBR techniques. The change of the superconducting critical temperature at different magnetic orientations of two magnetic layers were found to be highly sensitive to the thickness and ratio of the magnetic and superconducting layers. In the chapter 4, we presented the fabrication and characterizations of 3-terminal SOT-MRAM devices. We found that the ion-beam etching process was the most critical step in the process flow and a combination of low angle and high angle etching was applied to pattern the nanopillars. The single-device measurements give the information about the spin Hall angle of β-W. By inserting Hf interlayers into the heterostructure, the critical switching current density of the devices decreased due to the introduction of a perpendicular anisotropy in the free layer, which was reproduced by micromagnetic simulations.

Bibliography

[1] N. Q. Minh, K. Kendall, and M. Kendall, *High-Temperature Solid Oxide Fuel Cells for the 21st Century*. Academic Press, 2015.

[2] N. Q. Minh, K. Kendall, and M. Kendall, *High-Temperature Solid Oxide Fuel Cells for the 21st Century*. Academic Press, 2015.

[3] A. Evans, A. Bieberle-Hütter, J. L. M. Rupp, and L. J. Gauckler, "Review on microfabricated micro-solid oxide fuel cell membranes," *J. Power Sources*, vol. 194, no. 1, p. 119, 2009.

[4] J. H. Shim, J. S. Park, J. An, T. M. Gür, S. Kang, and F. B. Prinz, "Intermediate-temperature ceramic fuel cells with thin film yttrium-doped barium zirconate electrolytes," *Chem. Mater.*, vol. 21, no. 14, p. 3290, 2009.

[5] P.-C. Su, C.-C. Chao, J. H. Shim, R. Fasching, and F. B. Prinz, "Solid oxide fuel cell with corrugated thin film electrolyte," *Nano Lett.*, vol. 8, no. 8, p. 2289, 2008.

[6] J. An, Y. B. Kim, J. Park, T. M. Gür, and F. B. Prinz, "Three-dimensional nanostructured bilayer solid oxide fuel cell with 1.3 w/cm2 at 450°c," *Nano Lett.*, vol. 13, no. 9, p. 4551, 2013.

[7] S. Ji, G. Y. Cho, W. Yu, P.-C. Su, M. H. Lee, and S. W. Cha, "Plasma-enhanced atomic layer deposition of nanoscale yttria-stabilized zirconia electrolyte for solid oxide fuel cells with porous substrate," *ACS Appl. Mater. Interfaces*, vol. 7, no. 5, p. 2998, 2015.

[8] Y.-W. Ju, A. Jun, A. Inoishi, S. Ida, T. Lim, G. Kim, and T. Ishihara, "Growth of thin-film layered perovskite cathodes by pulsed laser deposition and their electrochemical studies in it-sofcs," *J. Electrochem. Soc.*, vol. 161, no. 6, p. F698, 2014.

[9] F. Wang, M. E. Brito, K. Yamaji, D. H. Cho, M. Nishi, H. Kishimoto, T. Horita, and H. Yokokawa, "Effect of polarization on sr and zr diffusion behavior in lscf/gdc/ysz system," *Solid State Ionics*, vol. 262, p. 454, 2014.

[10] M. Tsuchiya, B. K. Lai, and S. Ramanathan, "Scalable nanostructured membranes for solid-oxide fuel cells," *Nat. Nanotechnol.*, vol. 6, no. 5, p. 282, 2011.

[11] I. Chang, S. Woo, M. H. Lee, J. H. Shim, Y. Piao, and S. W. Cha, "Characterization of porous pt films deposited via sputtering," *Appl. Surf. Sci.*, vol. 282, p. 463, 2013.

[12] X. Wang, H. Huang, T. Holme, X. Tian, and F. B. Prinz, "Thermal stabilities of nanoporous metallic electrodes at elevated temperatures," *J. Power Sources*, vol. 175, no. 1, p. 75, 2008.

[13] I. Chang, S. Ji, J. Park, M. H. Lee, and S. W. Cha, "Ultrathin ysz coating on pt cathode for high thermal stability and enhanced oxygen reduction reaction activity," *Adv. Energy Mater.*, vol. 5, no. 10, p. 1402251, 2015.

[14] Y. H. Lee, G. Y. Cho, I. Chang, S. Ji, Y. B. Kim, and S. W. Cha, "Platinum-based nanocomposite electrodes for low-temperature solid oxide fuel cells with extended lifetime," *J. Power Sources*, vol. 307, p. 289, 2016.

[15] H. J. Choi, M. Kim, K. C. Neoh, D. Y. Jang, H. J. Kim, J. M. Shin, G. T. Kim, and J. H. Shim, "High-performance silver cathode surface treated with scandia-stabilized zirconia nanoparticles for intermediate temperature solid oxide fuel cells," *Adv. Energy Mater.*, vol. 7, no. 4, p. 1601956, 2017.

[16] N. Q. Minh, "Ceramic fuel cells," *J. Am. Ceram. Soc.*, vol. 76, no. 3, p. 563, 1993.

[17] R. O'Hayre, S.-W. Cha, W. Colella, and F. B. Prinz, *Fuel Cell Fundamentals*. Wiley, 2006.

[18] H.-S. Noh, J.-W. Son, H. Lee, H.-I. Ji, J.-H. Lee, and H.-W. Lee, "Suppression of ni agglomeration in pld fabricated ni-ysz composite for surface modification of sofc anode," *J. Eur. Ceram. Soc.*, vol. 30, no. 16, p. 3415, 2010.

[19] J. A. Thornton, "The microstructure of sputter deposited coatings," *J. Vac. Sci. Technol., A*, vol. 4, no. 6, p. 3059, 1986.

[20] M. Mogensen, "The kinetics of hydrogen oxidation on a ni-YSZ SOFC electrode at 1000°c," *ECS Proceedings Volumes*, vol. 1993-4, pp. 484–493, jan 1993.

[21] N. Mahato, A. Banerjee, A. Gupta, S. Omar, and K. Balani, "Progress in material selection for solid oxide fuel cell technology: A review," *Progress in Materials Science*, vol. 72, pp. 141 – 337, 2015.

[22] H. Sumi, Y.-H. Lee, H. Muroyama, T. Matsui, M. Kamijo, S. Mimuro, M. Yamanaka, Y. Nakajima, and K. Eguchi, "Effect of carbon deposition by carbon monoxide disproportionation on electrochemical characteristics at low temperature operation for solid oxide fuel cells," *Journal of Power Sources*, vol. 196, no. 10, pp. 4451–4457, 2011.

[23] C. M. Chun, J. D. Mumford, and T. A. Ramanarayanan, "Carbon-induced corrosion of nickel anode," *Journal of The Electrochemical Society*, vol. 147, no. 10, p. 3680, 2000.

[24] A. Atkinson, S. Barnett, R. Gorte, J. Irvine, A. McEvoy, M. Mogensen, S. Singhal, and J. Vohs, "Advanced anodes for high-temperature fuel cells," *Nature Materials*, vol. 3, pp. 17–27, Jan. 2004.

[25] T. Hibino, A. Hashimoto, K. Asano, M. Yano, M. Suzuki, and M. Sano, "An intermediate-temperature solid oxide fuel cell providing higher performance with hydrocarbons than with hydrogen," *Electrochemical and Solid-State Letters*, vol. 5, no. 11, p. A242, 2002.

[26] T. Hibino, A. Hashimoto, M. Yano, M. Suzuki, and M. Sano, "Ru-catalyzed anode materials for direct hydrocarbon sofcs," *Electrochimica Acta*, vol. 48, no. 17, pp. 2531 – 2537, 2003.

[27] T. Ioroi, T. Hara, Y. Uchimoto, Z. Ogumi, and Z.-i. Takehara, "Preparation of Perovskite-Type La1 - x Sr x MnO3 Films by Vapor-Phase Processes and Their Electrochemical Properties," *J. Electrochem. Soc.*, vol. 144, pp. 1362–1370, Apr 1997.

[28] C.-W. Kwon, J.-W. Son, J.-H. Lee, H.-M. Kim, H.-W. Lee, and K.-B. Kim, "High-performance micro-solid oxide fuel cells fabricated on nanoporous anodic aluminum oxide templates," *Adv. Funct. Mater.*, vol. 21, no. 6, p. 1154, 2011.

[29] J. Park, Y. Lee, I. Chang, W. Lee, and S. W. Cha, "Engineering of the electrode structure of thin film solid oxide fuel cells," *Thin Solid Films*, vol. 584, p. 125, 2015.

[30] B. A. Boukamp and A. Rolle, "Use of a distribution function of relaxation times (DFRT) in impedance analysis of SOFC electrodes," *Solid State Ionics*, vol. 314, pp. 103–111, Jan 2018.

[31] G. Y. Cho, Y. H. Lee, and S. W. Cha, "Multi-component nano-composite electrode for sofcs via thin film technique," *Renewable Energy*, vol. 65, p. 130, 2014.

[32] H. J. Leamy and A. G. Dirks, "Microstructure and magnetism in amorphous rare-earth–transition-metal thin films. i. microstructure," *J. Appl. Phys.*, vol. 49, no. 6, p. 3430, 1978.

[33] W. Jung, J. J. Kim, and H. L. Tuller, "Investigation of nanoporous platinum thin films fabricated by reactive sputtering: Application as micro-sofc electrode," *J. Power Sources*, vol. 275, p. 860, 2015.

[34] W.-H. Kim, H.-S. Song, J. Moon, and H.-W. Lee, "Intermediate temperature solid oxide fuel cell using (la, sr)(co, fe)o3-based cathodes," *Solid State Ionics*, vol. 177, no. 35–36, p. 3211, 2006.

[35] E. Perry Murray, M. Sever, and S. Barnett, "Electrochemical performance of (la,sr)(co,fe)o3–(ce,gd)o3 composite cathodes," *Solid State Ionics*, vol. 148, no. 1, pp. 27 – 34, 2002.

[36] D.-H. Myung, J. Hwang, J. Hong, H.-W. Lee, B.-K. Kim, J.-H. Lee, and J.-W. Son, "Pulsed laser deposition of la0.6sr0.4coo3 ce0.9gd0.1o2 nano-composite and its application to gradient-structured thin-film cathode of SOFC," *Journal of The Electrochemical Society*, vol. 158, no. 8, p. B1000, 2011.

[37] C. Benel, A. J. Darbandi, R. Djenadic, A. Evans, R. Tölke, M. Prestat, and H. Hahn, "Synthesis and characterization of nanoparticulate la0.6sr0.4coo3-x cathodes for thin-film solid oxide fuel cells," *Journal of Power Sources*, vol. 229, pp. 258 – 264, 2013.

[38] Y. H. Lee, H. Ren, E. A. Wu, E. E. Fullerton, Y. S. Meng, and N. Q. Minh, "All-sputtered, superior power density thin-film solid oxide fuel cells with a novel nanofibrous ceramic cathode," *Nano Letters*, vol. 20, no. 5, pp. 2943–2949, 2020. PMID: 32176514.

[39] B. S. Kang, J. Matsuda, Y. W. Ju, H. H. Kim, and T. Ishihara, "Nano strain induced double columnar oxide as highly active oxygen-dissociation electrode for ni-fe metal supported solid oxide fuel cells," *Nano Energy*, vol. 56, pp. 382 – 390, 2019.

[40] Y.-W. Ju, J. Hyodo, A. Inoishi, S. Ida, T. Tohei, Y.-G. So, Y. Ikuhara, and T. Ishihara, "Double columnar structure with a nanogradient composite for increased oxygen diffusivity and reduction activity," *Advanced Energy Materials*, vol. 4, no. 17, p. 1400783, 2014.

[41] B. S. Kang, A. Inoishi, A. Takagaki, and T. Ishihara, "Pr2ni0.71cu0.24ga0.05o4-sm0.2ce0.8o1.9 composite film as active cathodic layer for intermediate temperature solid oxide fuel cells," *Solid State Ionics*, vol. 327, pp. 59 – 63, 2018.

[42] T. H. Wan, M. Saccoccio, C. Chen, and F. Ciucci, "Influence of the discretization methods on the distribution of relaxation times deconvolution: Implementing radial basis functions with drttools," *Electrochimica Acta*, vol. 184, pp. 483 – 499, 2015.

[43] M. Saccoccio, T. H. Wan, C. Chen, and F. Ciucci, "Optimal regularization in distribution of relaxation times applied to electrochemical impedance spectroscopy: Ridge and lasso regression methods - a theoretical and experimental study," *Electrochimica Acta*, vol. 147, pp. 470 – 482, 2014.

[44] M. J. Jørgensen and M. Mogensen, "Impedance of solid oxide fuel cell LSM/YSZ composite cathodes," *Journal of The Electrochemical Society*, vol. 148, no. 5, p. A433, 2001.

[45] F. S. Baumann, J. Fleig, G. Cristiani, B. Stuhlhofer, H.-U. Habermeier, and J. Maier, "Quantitative comparison of mixed conducting SOFC cathode materials by means of thin film model electrodes," *Journal of The Electrochemical Society*, vol. 154, no. 9, p. B931, 2007.

[46] G. Brug, A. van den Eeden, M. Sluyters-Rehbach, and J. Sluyters, "The analysis of electrode impedances complicated by the presence of a constant phase element," *Journal of Electroanalytical Chemistry and Interfacial Electrochemistry*, vol. 176, no. 1, pp. 275 – 295, 1984.

[47] T. Mcguire and R. Potter, "Anisotropic magnetoresistance in ferromagnetic 3d alloys," *IEEE Transactions on Magnetics*, vol. 11, pp. 1018–1038, 1975.

[48] G. Tatara and H. Fukuyama, "Resistivity due to a Domain Wall in Ferromagnetic Metal," *Physical Review Letters*, vol. 78, no. 19, pp. 3773–3776, 1997.

[49] U. Rudiger, J. Yu, S. S. P. Parkin, and A. D. Kent, "Magnetoresistance of epitaxial Fe wires with varied domain wall structure," *Journal of Magn*, vol. 199, pp. 261–263, 1999.

[50] V. D. Nguyen, L. Vila, P. Laczkowski, A. Marty, T. Faivre, and J. P. Attane, "Detection of Domain-Wall Position and Magnetization Reversal in Nanostructures Using the Magnon Contribution to the Resistivity," *Physical Review Letters*, vol. 107, no. 136605, pp. 1–4, 2011.

[51] P. A. E. Jonkers, "Magnetoresistance in magnetic domain wall systems," *Journal of Magnetism and Magnetic Materials*, vol. 247, pp. 178–186, 2002.

[52] B. Raquet, M. Viret, E. Sondergard, O. Cespedes, and R. Mamy, "Electron-magnon scattering and magnetic resistivity in 3d ferromagnets," *Physical Review B*, vol. 66, no. 024433, pp. 1–11, 2002.

[53] W. Gil, D. Görlitz, M. Horisberger, and J. Kötzler, "Magnetoresistance anisotropy of polycrystalline cobalt films: Geometrical-size and domain effects," *Physical Review B*, vol. 72, no. 134401, pp. 1–10, 2005.

[54] A. P. Mihai, A. Marty, P. Warin, and Y. Samson, "Electron-magnon diffusion and magnetization reversal detection in FePt thin films," *Physical Review B*, vol. 77, no. 060401, pp. 1–4, 2008.

[55] K. T. Chan, J. J. Kan, C. Doran, L. Ouyang, D. J. Smith, E. E. Fullerton, K. T. Chan, J. J. Kan, C. Doran, L. Ouyang, and J. David, "Controlled growth behavior of chemical vapor deposited Ni nanostructures," *Philosophical Magazine*, vol. 92, no. 17, pp. 2173–2186, 2012.

[56] R.-Q. Zhang, Y. Lifshitz, and S.-T. Lee, "Oxide-assisted growth of semiconducting nanowires," *Advanced Materials*, vol. 15, no. 7-8, pp. 635–640, 2003.

[57] K. N. Trohidou, J. A. Blackman, and J. F. Cooke, "Calculation of the high-energy spin-wave spectrum of hcp cobalt," *Phys. Rev. Lett.*, vol. 67, pp. 2561–2564, Oct 1991.

[58] K. T. Chan, J. J. Kan, C. Doran, L. Ouyang, D. J. Smith, and E. E. Fullerton, "Oriented Growth of Single-Crystal Ni Nanowires onto Amorphous SiO2," *Nano Letters*, vol. 10, pp. 5070–5075, 2010.

[59] A. Vansteenkiste, J. Leliaert, M. Dvornik, M. Helsen, F. Garcia-Sanchez, and B. Van Waeyenberge, "The design and verification of MuMax3," *AIP Adv.*, vol. 4, p. 107133, Oct 2014.

[60] G. R. Taylor, A. Isin, and R. V. Coleman, "Resistivity of Iron as a Function of Temperature and Magnetization," *Physical review*, vol. 165, no. 2, pp. 621–631, 1968.

[61] A. Fert and I. A. Campbell, "Electrical resistivity of ferromagnetic nickel and iron based alloys alloys," *Journal of Physics F: Metal Physics*, vol. 6, no. 5, pp. 849–871, 1976.

[62] M. N. Ou, T. J. Yang, S. R. Harutyunyan, Y. Y. Chen, C. D. Chen, and S. J. Lai, "Electrical and thermal transport in single nickel nanowire," *Applied Physics Letters*, vol. 92, no. 063101, pp. 1–3, 2008.

[63] M. V. Kamalakar and A. K. Raychaudhuri, "Low temperature electrical transport in ferromagnetic Ni nanowires," *Physical Review B*, vol. 79, no. 205417, pp. 1–8, 2009.

[64] J. Dorleijn and A. Miedema, "The Magnetic Resistance Anisotropy in Nickel and Iron Based Alloys," *AIP Conference Proceedings*, vol. 34, no. 50, pp. 50–54, 1976.

[65] A. Fert, "Two-current conduction in ferromagnetic metals and spin wave-electron collisions," *Journal of Physics C: Solid State Physics*, vol. 2, no. 2, pp. 1784–1788, 1969.

[66] W. Martienssen and H. Warlimont, *Springer Handbooks (Springer-Verlag, Berlin, Heidelberg, 2005).* (Springer-Verlag, Berlin, Heidelberg, 2005)., 2005.

[67] K. T. K. IKEDA, K. SUZUKI, "ELECTRICAL RESISTIVITY IN FERROMAGNETIC Ni-BASE ALLOYS CONTAINING Al, Si AND Ge," *Journal of Magnetism and Magnetic Materials*, vol. 40, pp. 232–240, 1983.

[68] J. J. Kan, M. V. Lubarda, K. T. Chan, A. Scholl, V. Lomakin, and E. E. Fullerton, "Periodic chiral magnetic domains in single-crystal nickel nanowires," *Physical Review Materials*, vol. 2, no. 064406, pp. 1–8, 2018.

[69] W. J. Carr, "Temperature Dependence of Ferromagnetic Anisotropy," *Physical Review*, vol. 109, no. 6, pp. 1971–1976, 1958.

[70] E. A. Turov and A. I. Mitsek, "ON THE THEORY OF THE TEMPERATURE DEPENDENCE OF FERROMAGNETIC ANISOTROPY," *Soviet Physics Jetp*, vol. 37, no. 4, pp. 801–806, 1960.

[71] E. C. Stoner and E. P. Wohlfarth, "A Mechanism of Magnetic Hysteresis in Heterogeneous Alloys," *Philosophical Transactions of the Royal Society A*, vol. 240, no. 826, pp. 599–642, 1948.

[72] E. Tatsumoto, T. Okamoto, and N. Iwata, "Eiji Tatsumoto Temperature Dependence of the Magnetocrystalline Anisotropy Constants K1 and K2 of Nickel jpsj.20.1541.pdf," *J. Phys. Soc. Japan*, vol. 20, pp. 1541–1542, 1965.

[73] M. Sillassen, P. Eklund, N. Pryds, N. Bonanos, and J. Bøttiger, "Concentration-dependent ionic conductivity and thermal stability of magnetron-sputtered nanocrystalline scandia-stabilized zirconia," *Solid State Ionics*, vol. 181, pp. 1140–1145, Aug 2010.

[74] J. Crangle and M. J. C. Martin, "Magnetic moments and electron transfer in nickel-rich binary alloys," *Philosophical Magazine*, vol. 4, no. 45, pp. 1006–1012, 1959.

[75] A. D. Kent, U. Rüdiger, J. Yu, L. Thomas, S. S. P. Parkin, A. D. Kent, and U. Ru, "Magnetoresistance, micromagnetism, and domain wall effects in epitaxial Fe and Co structures with stripe domains (invited)," *Journal of Applied Physics*, vol. 85, no. 8, pp. 5243–5248, 1999.

[76] H. A. Alperin, O. Steinsvoll, G. Shirane, and R. Nathans, "Observation of the Dispersion Relation for Spin Waves in Hexagonal Cobalt," *Journal of Applied Physics*, vol. 37, no. 3, pp. 1052–1053, 1966.

[77] M. W. Stringfellow, "Observation of spin-wave renormalization effects in iron and nickel," *Journal of Physics C: Solid State Physics*, vol. 1, no. 2, pp. 950–965, 1968.

[78] A. F. Andreev, "The thermal conductivity of the intermediate state in superconductors," 1964.

[79] F. S. Bergeret, A. F. Volkov, and K. B. Efetov, "Long-Range Proximity Effects in Superconductor-Ferromagnet Structures," *Phys. Rev. Lett.*, vol. 86, pp. 4096–4099, Apr 2001.

[80] A. Kadigrobov, R. I. Shekhter, and M. Jonson, "Triplet superconducting proximity effect in inhomogeneous magnetic materials," *Low Temp. Phys.*, vol. 27, pp. 760–766, Sep 2001.

[81] F. S. Bergeret, A. F. Volkov, and K. B. Efetov, "Odd triplet superconductivity and related phenomena in superconductor-ferromagnet structures," *Rev. Mod. Phys.*, vol. 77, pp. 1321–1373, Nov 2005.

[82] T. Kontos, M. Aprili, J. Lesueur, and X. Grison, "Inhomogeneous Superconductivity Induced in a Ferromagnet by Proximity Effect," *Phys. Rev. Lett.*, vol. 86, pp. 304–307, Jan 2001.

[83] R. S. Keizer, S. T. B. Goennenwein, T. M. Klapwijk, G. Miao, G. Xiao, and A. Gupta, "A spin triplet supercurrent through the half-metallic ferromagnet CrO2," *Nature*, vol. 439, pp. 825–827, Feb 2006.

[84] J. Wang, M. Singh, M. Tian, N. Kumar, B. Liu, C. Shi, J. K. Jain, N. Samarth, T. E. Mallouk, and M. H. W. Chan, "Interplay between superconductivity and ferromagnetism in crystalline nanowires," *Nat. Phys.*, vol. 6, pp. 389–394, May 2010.

[85] M. S. Anwar, F. Czeschka, M. Hesselberth, M. Porcu, and J. Aarts, "Long-range supercurrents through half-metallic ferromagnetic CrO_2," *Phys. Rev. B*, vol. 82, p. 100501, Sep 2010.

[86] V. V. Ryazanov, V. A. Oboznov, A. Yu. Rusanov, A. V. Veretennikov, A. A. Golubov, and J. Aarts, "Coupling of Two Superconductors through a Ferromagnet: Evidence for a π Junction," *Phys. Rev. Lett.*, vol. 86, pp. 2427–2430, Mar 2001.

[87] M. A. Khasawneh, T. S. Khaire, C. Klose, W. P. Pratt, and N. O. Birge, “Spin-triplet supercurrent in Co-based Josephson junctions,” *Supercond. Sci. Technol.*, vol. 24, p. 024005, Jan 2011.

[88] A. F. Volkov and K. B. Efetov, “Odd spin-triplet superconductivity in a multilayered superconductor-ferromagnet Josephson junction,” *Phys. Rev. B*, vol. 81, p. 144522, Apr 2010.

[89] J. W. A. Robinson, J. D. S. Witt, and M. G. Blamire, “Controlled Injection of Spin-Triplet Supercurrents into a Strong Ferromagnet,” *Science*, vol. 329, pp. 59–61, Jul 2010.

[90] P. V. Leksin, N. N. Garif’yanov, I. A. Garifullin, Ya. V. Fominov, J. Schumann, Y. Krupskaya, V. Kataev, O. G. Schmidt, and B. Büchner, “Evidence for Triplet Superconductivity in a Superconductor-Ferromagnet Spin Valve,” *Phys. Rev. Lett.*, vol. 109, p. 057005, Aug 2012.

[91] V. I. Zdravkov, J. Kehrle, G. Obermeier, D. Lenk, H.-A. Krug von Nidda, C. Müller, M. Yu. Kupriyanov, A. S. Sidorenko, S. Horn, R. Tidecks, and L. R. Tagirov, “Experimental observation of the triplet spin-valve effect in a superconductor-ferromagnet heterostructure,” *Phys. Rev. B*, vol. 87, p. 144507, Apr 2013.

[92] Ya. V. Fominov, A. A. Golubov, T. Yu. Karminskaya, M. Yu. Kupriyanov, R. G. Deminov, and L. R. Tagirov, “Superconducting triplet spin valve,” *JETP Lett.*, vol. 91, pp. 308–313, Mar 2010.

[93] A. Singh, S. Voltan, K. Lahabi, and J. Aarts, “Colossal Proximity Effect in a Superconducting Triplet Spin Valve Based on the Half-Metallic Ferromagnet CrO_2,” *Phys. Rev. X*, vol. 5, p. 021019, May 2015.

[94] M. G. Flokstra, T. C. Cunningham, J. Kim, N. Satchell, G. Burnell, P. J. Curran, S. J. Bending, C. J. Kinane, J. F. K. Cooper, S. Langridge, A. Isidori, N. Pugach, M. Eschrig, and S. L. Lee, “Controlled suppression of superconductivity by the generation of polarized Cooper pairs in spin-valve structures,” *Phys. Rev. B*, vol. 91, p. 060501, Feb 2015.

[95] J. E. Hirsch, “Spin Hall Effect,” *Physical Review Letters*, vol. 83, no. 9, pp. 1834–1837, 1999.

[96] J. C. Slonczewski, “Current-driven excitation of magnetic multilayers,” *Journal of Magnetism and Magnetic Materials*, vol. 159, pp. L1–L7, 1996.

[97] J. A. Katine, F. J. Albert, and R. A. Buhrman, “Current-Driven Magnetization Reversal and Spin-Wave Excitations in Co/Cu/Co Pillars,” *Physical Review Letters*, vol. 84, no. 14, pp. 3149–3152, 2000.

[98] D. C. Ralph and M. D. Stiles, “Spin transfer torques,” *Journal of Magnetism and Magnetic Materials*, vol. 320, pp. 1190–1216, 2008.

[99] L. Liu, C.-f. Pai, Y. Li, H. W. Tseng, D. C. Ralph, and R. A. Buhrman, "Spin-Torque Switching with the Giant Spin Hall Effect of Tantalum," *Science*, vol. 336, pp. 555–559, 2012.

[100] I. M. Miron, K. Garello, G. Gaudin, P.-J. Zermatten, M. V. Costache, S. Auffret, S. Bandiera, B. Rodmacq, A. Schuh, and P. Gambardella, "Perpendicular switching of a single ferromagnetic layer induced by in-plane current injection," *Nature*, vol. 476, pp. 189–193, 2011.

[101] S. Shi, Y. Ou, S. V. Aradhya, D. C. Ralph, and R. A. Buhrman, "Fast Low-Current Spin-Orbit-Torque Switching of Magnetic Tunnel Junctions through Atomic Modifications of the Free-Layer Interfaces," *Physical Review Applied*, vol. 9, p. 11002, 2018.

[102] M. Cubukcu, O. Boulle, D. Marc, K. Garello, C. O. Avci, I. M. Miron, J. Langer, B. Ocker, P. Gambardella, and G. Gaudin, "Spin-orbit torque magnetization switching of a three-terminal perpendicular magnetic tunnel junction," *Applied Physics Letters*, vol. 104, p. 042406, 2014.

[103] K. Garello, C. O. Avci, I. M. Miron, M. Baumgartner, A. Ghosh, S. Auffret, O. Boulle, G. Gaudin, and P. Gambardella, "Ultrafast magnetization switching by spin-orbit torques," *Applied Physics Letters*, vol. 105, p. 212402, 2014.

[104] S. Zhang, Y. Su, X. Li, W. Tian, J. Hong, and L. You, "Spin-orbit-torque-driven multilevel switching in Ta/CoFeB/MgO structures without initialization Spin-orbit-torque-driven multilevel switching in Ta/CoFeB/MgO structures without initialization," *Applied Physics Letters*, vol. 114, p. 042401, 2019.

[105] U. A. B. Campus and E. Avan, "Current-induced spin–orbit torques," *Philosophical Transactions of the Royal Society A*, vol. 369, pp. 3175–3197, 2011.

[106] M. Yamanouchi, L. Chen, J. Kim, M. Hayashi, H. Sato, S. Fukami, S. Ikeda, F. Matsukura, and H. Ohno, "Three terminal magnetic tunnel junction utilizing the spin Hall effect of iridium-doped copper," *Applied Physics Letters*, vol. 102, p. 212408, 2013.

[107] S. Fukami, T. Anekawa, C. Zhang, and H. Ohno, "A spin–orbit torque switching scheme with collinear magnetic easy axis and current configuratio," *Nature Nanotechnology*, vol. 11, pp. 621–625, 2016.

[108] Y. Kajiwara, K. Harii, S. Takahashi, J. Ohe, K. Uchida, M. Mizuguchi, H. Umezawa, H. Kawai, K. Ando, K. Takanashi, S. Maekawa, and E. Saitoh, "Transmission of electrical signals by spin-wave interconversion in a magnetic insulator," *Nature*, vol. 464, pp. 262–266, 2010.

[109] Y. Ou, C.-f. Pai, S. Shi, D. C. Ralph, and R. A. Buhrman, "Origin of fieldlike spin-orbit torques in heavy metal/ferromagnet/oxide thin film heterostructures," *Physical Review B*, vol. 94, p. 140414(R), 2016.

[110] C.-f. Pai, L. Liu, H. W. Tseng, D. C. Ralph, and R. A. Buhrman, “Spin transfer torque devices utilizing the giant spin Hall effect of tungsten,” *Applied Physics Letters*, vol. 101, p. 122404, 2012.

[111] X. Peng, S. Wakeham, A. Morrone, S. Axdal, M. Feldbaum, J. Hwu, T. Boonstra, Y. Chen, and J. Ding, “Towards the sub-50 nm magnetic device definition: Ion beam etching (IBE) vs plasma-based etching,” *Vaccum*, vol. 83, pp. 1007–1013, 2009.

[112] K. Garello, F. Yasin, S. Couet, L. Souriau, J. Swerts, S. Rao, S. V. Beek, W. Kim, E. Liu, S. Kundu, D. Tsvetanova, N. Jossart, K. Croes, E. Grimaldi, M. Baumgartner, D. Crotti, A. Furnémont, P. Gambardella, and G. Kar, “SOT-MRAM 300mm integration for low power and ultrafast embedded memories,” in *2018 Symposium on VLSI circuits Digest of Technical Papers*, pp. 81–82, 2018.

[113] K. Sugiura, S. Takahashi, M. Amano, T. Kajiyama, M. Iwayama, Y. Asao, N. Shimomura, T. Kishi, S. Ikegawa, H. Yoda, and A. Nitayama, “Ion Beam Etching Technology for High-Density Spin Transfer Torque Magnetic Random Access Memory,” *Japanese Journal of Applied Physics*, vol. 48, p. 08HD02, 2009.

[114] S.-w. Chun, D. Kim, J. Kwon, B. Kim, S. Choi, and S.-b. Lee, “Multi-step ion beam etching of sub-30 nm magnetic tunnel junctions for reducing leakage and MgO barrier damage,” *Journal of Applied Physics*, vol. 111, p. 07C722, 2012.

[115] R. E. Lee, “Microfabrication by ion-beam etching,” *Journal of Vacuum Science & Technology*, vol. 16, no. 2, pp. 164–170, 1979.

[116] V. Ip, S. Huang, S. D. Carnevale, I. L. Berry, K. Rook, T. B. Lill, A. P. Paranjpe, and F. Cerio, “Ion Beam Patterning of High-Density STT-RAM Devices,” *IEEE Transactions on Magnetics*, vol. 53, no. 2, pp. 1–4, 2017.

[117] J. Z. Sun, “Spin-current interaction with a monodomain magnetic body: A model study,” *Physical Review B*, vol. 62, no. 1, pp. 570–578, 2000.

[118] J. Z. Sun, L. Chen, Y. Suzuki, S. S. P. Parkin, and R. H. Koch, “Thermally activated sweep-rate dependence of magnetic switching field in nanostructured current-perpendicular spin-valves,” *Journal of Magnetism and Magnetic Materials*, vol. 247, pp. 237–241, 2002.

[119] E. B. Myers, F. J. Albert, J. C. Sankey, E. Bonet, R. A. Buhrman, and D. C. Ralph, “Thermally Activated Magnetic Reversal Induced by a Spin-Polarized Current,” *Physical Review Letters*, vol. 89, no. 19, p. 196801, 2002.

[120] R. H. Koch, J. A. Katine, and J. Z. Sun, “Time-Resolved Reversal of Spin-Transfer Switching in a Nanomagnet,” *Physical Review Letters*, vol. 92, no. 8, p. 088302, 2004.

[121] C.-f. Pai, M.-H. Nguyen, C. Belvin, L. H. Vilela-Leao, D. C. Ralph, and R. A. Ruhrman, “Enhancement of perpendicular magnetic anisotropy and transmission of spin-Hall- effect-induced spin currents by a Hf spacer layer in W/Hf/CoFeB/MgO layer structures,” *Applied Physics Letters*, vol. 104, p. 082407, 2014.

[122] C.-f. Pai, Y. Ou, L. H. Vilela-le, D. C. Ralph, and R. A. Buhrman, “Dependence of the efficiency of spin Hall torque on the transparency of Pt/ferromagnetic layer interfaces,” *Physical Review B*, vol. 92, no. 064426, 2015.

[123] A. Vansteenkiste, J. Leliaert, M. Dvornik, M. Helsen, F. Garcia-sanchez, and B. V. Waeyenberge, “The design and verification of MuMax3,” *AIP Advance*, vol. 4, no. 107133, 2014.